

## Stellar Population and Elemental Abundance Gradients of Early-type Galaxies\*

A. FELDMEI<sup>E</sup>R-KRAUSE <sup>1</sup>, I. LONOCE <sup>2</sup>, AND W. L. FREEDMAN <sup>2</sup>

<sup>1</sup>*Max-Planck-Institut für Astronomie, Königstuhl 17, 69117, Heidelberg, Germany*

<sup>2</sup>*Department of Astronomy & Astrophysics, The University of Chicago, 5640 South Ellis Avenue, Chicago, IL 60637, USA*

(Received May 9, 2021; Revised August 17, 2021; Accepted September 17, 2021)

Submitted to ApJ

### ABSTRACT

The evolution of galaxies is imprinted in their stellar populations. Several stellar population properties in massive early-type galaxies have been shown to correlate with intrinsic galaxy properties like the galaxy’s central velocity dispersion, suggesting that stars formed in an initial collapse of gas ( $z \sim 2$ ). However, stellar populations change as a function of galaxy radius, and it is not clear how local gradients of individual galaxies are influenced by global galaxy properties and galaxy environment. In this paper, we study the stellar populations of eight early-type galaxies as a function of radius. We use optical spectroscopy ( $\sim 4000\text{--}8600\text{ \AA}$ ) and full-spectral fitting to measure stellar population age, metallicity, IMF slope, and nine elemental abundances (O, Mg, Si, Ca, Ti, C, N, Na, Fe) out to  $1 R_e$  for each galaxy individually. We find a wide range of properties, with ages ranging from 3–13 Gyr. Some galaxies have a radially constant, Salpeter-like IMF, and other galaxies have a super-Salpeter IMF in the center, decreasing to a sub-Salpeter IMF at  $\sim 0.5 R_e$ . We find a global correlation of the central  $[Z/H]$  to the central IMF and the radial gradient of the IMF for the eight galaxies, but local correlations of the IMF slope to other stellar population parameters hold only for subsets of the galaxies in our sample. Some elemental abundances also correlate locally with each other within a galaxy, suggesting a common production channel. Those local correlations appear only in subsets of our galaxies indicating variations of the stellar content among different galaxies.

*Keywords:* galaxies: abundances – galaxies: elliptical and lenticular, cD – galaxies: stellar content – galaxies: individual (NGC 1404, NGC 3923, NGC 4552, NGC 4697, NGC 5061, NGC 7144, NGC 7796, IC 1459, UGC 1382)

### 1. INTRODUCTION

Radial stellar population gradients in early-type galaxies provide information on a galaxy’s formation and evolution. Age and metallicity help us to understand the star formation history; chemical abundances can constrain star formation time-scales and chemical enrichment history. The initial mass function (IMF) affects the chemical evolution. All of these parameters are required to fully understand the evolution of a galaxy.

Massive early-type galaxies are thought to have formed in two main stages (e.g. Naab et al. 2009; Oser et al. 2010): in an early ( $z \approx 2$ ) collapse of gas, stars formed in situ in a compact core. The second stage is ongoing to the present: satellite galaxies are accreted and deliver stars to the galaxy that were formed ex situ. The fraction of accreted stars is higher for more massive galaxies, and at large galaxy radius, due to the longer dynamical timescales (e.g. Greene et al. 2015). A small fraction (ca. 10%, Thomas et al. 2010) of early-type galaxies show signs of recent star formation activity, with a young sub-population of stars that formed in situ. Thomas et al. (2010) suggest that rejuvenation may be triggered by galaxy interaction and merger activity in the past few gigayears. Since most early-type galaxies show only little recent star formation, their stel-

Corresponding author: A. Feldmeier-Krause  
feldmeier@mpia.de

\* This paper includes data gathered with the 6.5 meter Magellan Telescopes located at Las Campanas Observatory, Chile.

lar mass is dominated by old stars, and we can learn about galaxy assembly and early star formation from their stellar populations.

Important clues come from chemical elemental abundances, as different chemical elements have different origins. Hydrogen, deuterium and most helium were formed in primordial nucleosynthesis, but most other elements are produced by stellar nucleosynthesis or explosive burning in the late stages of stellar evolution (see the review by [Maiolino & Mannucci 2019](#), and references therein). Stars more massive than  $8 M_{\odot}$  produce most of the  $\alpha$  elements (e. g. O, Ne, Mg, Si, Ca, Ti). They end their life as core-collapse supernovae (SNe), and release elements into the ISM soon after the beginning of star formation. Massive stars also produce iron peak elements (e.g. Fe, Ni), but a larger portion is produced by type Ia SNe. Type Ia SNe are thermonuclear explosions of C-O white dwarfs that accrete mass, they produce Fe peak elements, but also Si, Ar, S, Ca. There is a delay between the explosion of massive stars and SNe Ia, in the range of about 40-50 Myr to few Gyr. Sodium is produced in both massive and intermediate-mass stars. Carbon and Nitrogen are partly produced in massive ( $>8 M_{\odot}$ ) stars, but a large portion (70% of N, and  $\sim$ 30-40% of C, [Romano et al. 2020](#)) is produced in intermediate-mass (2-8  $M_{\odot}$ ) asymptotic giant branch (AGB) stars and SNe Ia, leading also to a later enrichment compared to  $\alpha$  elements. The relative elemental abundances are thus caused by the delay between the production channels, and depend on the star formation history and the stellar initial mass function of a galaxy. However, other factors influence the element production of a star, for example the star’s total metallicity and stellar rotation.

Different studies revealed non-solar abundance ratios in early-type galaxies, and found increasing values as function of the galaxy mass or velocity dispersion (e.g. [Trager et al. 2000a](#); [Thomas et al. 2005](#); [Johansson et al. 2012](#); [Conroy et al. 2014](#); [Worthey et al. 2014](#)). This may be caused by a larger fraction of massive stars, i.e. a more top-heavy IMF, in more massive galaxies. Other explanations are more rapid star formation or quicker quenching in more massive galaxies, such that the star formation has ended before type Ia SNe enrich the material with Fe.

The IMF of massive early-type galaxies has been found to be bottom-heavy, i.e. dwarf-rich with a larger fraction of low-mass stars compared to the Milky Way (e.g. [Cenarro et al. 2003](#); [Treu et al. 2010](#); [Graves & Faber 2010](#); [van Dokkum & Conroy 2010](#); [Conroy & van Dokkum 2012](#); [La Barbera et al. 2013](#)). In some galaxies the IMF slope varies as a function of radius, being more

bottom-heavy in the center (e.g. [Martín-Navarro et al. 2015a](#); [van Dokkum et al. 2017](#); [Sarzi et al. 2018](#); [La Barbera et al. 2019](#); [Barbosa et al. 2021a](#)), while in other galaxies the IMF slope appears to be constant (e.g. [Zieleniewski et al. 2017](#); [Alton et al. 2017, 2018](#); [Vaughan et al. 2018a](#)).

Several possible global and local correlations of the IMF slope with other structural and stellar population parameters have been suggested, for example the galaxy’s velocity dispersion ([Cappellari et al. 2012](#); [Spiniello et al. 2014](#)), total metallicity  $[Z/H]$  ([Martín-Navarro et al. 2015b](#); [Parikh et al. 2018](#); [Zhou et al. 2019](#)), total mass density ([Spiniello et al. 2015](#)),  $[Mg/Fe]$  ([Conroy & van Dokkum 2012](#)),  $[Na/Fe]$  ([van Dokkum et al. 2017](#)),  $[\alpha/Fe]$ , or age ([McDermid et al. 2014](#)). Some of these correlations have not been found in other studies e.g. age by [Martín-Navarro et al. \(2015b\)](#) and [Zhou et al. \(2019\)](#),  $[Mg/Fe]$  by [Martín-Navarro et al. \(2015b\)](#) and [van Dokkum et al. \(2017\)](#),  $[Na/Fe]$  and  $[Z/H]$  by [La Barbera et al. \(2019\)](#), and local  $\sigma$  by [Martín-Navarro et al. \(2015b\)](#) and [Barbosa et al. \(2021b\)](#). In summary, there is still no consensus about which correlations hold, either globally or locally, and if any correlation signifies a causal relation or just that two parameters vary within galaxies in a similar way ([Martín-Navarro et al. 2019](#); [Smith 2020](#)).

In this paper we study stellar population gradients of eight early-type galaxies (NGC 1404, NGC 3923, NGC 4552, NGC 4697, NGC 5061, NGC 7144, NGC 7796, IC 1459) and one low-surface brightness spiral galaxy (UGC 1382). We measure single stellar population light-weighted age,  $[Z/H]$ , the IMF slope in the mass range  $0.08$ – $1.0 M_{\odot}$ , and nine elemental abundances (O, Mg, Si, Ca, Ti, C, N, Na, Fe). We investigate radial gradients for these parameters and test whether there are local correlations for the galaxies, and global correlations for the entire sample.

This paper is organised as follows: We describe the long-slit spectroscopic data in Section 2. We present our stellar population analysis and results in Section 3. In Section 4 we test whether local and global correlations of various stellar population parameters hold for our data set, and in Section 5 we compare relative elemental abundances, and how they vary as function of  $[Z/H]$ . We discuss our results in Section 6.

## 2. DATA

### 2.1. Galaxy Sample and Observations

We observed nine galaxies with the Inamori Magellan Areal Camera and Spectrograph (IMACS, [Dressler et al. 2006](#)) on the Magellan Baade 6.5 m telescope. The data were collected over several observing runs from

**Table 1.** Galaxy Sample

Galaxy	Type	Distance	$R_e$	Scale	$e$	Major Axis PA	$\mu_e$	$\sigma_{R_e/8}$	$M_B$	B-V	Env	$N_g$
		(Mpc)	(arcsec)	(kpc/arcmin)		( $^\circ$ )	(mag arcsec $^{-2}$ )	(km s $^{-1}$ )	(mag)	(mag)		
NGC 4552	S0/E0	15.8	31.2	4.60	...	...	20.02	250	-20.5	0.94	C	714
NGC 1404	E1	18.6	24.6	5.41	0.195	163.6	19.84	230	-20.7	0.94	C	120
NGC 3923	E4-5	20.9	86.4	6.08	0.271	48.0	22.06	246	-21.1	0.91	G	25
NGC 4697	E6	11.6	68.4	3.38	0.308	66.1	21.35	165	-20.3	0.87	G	19
NGC 5061	E0	26.0	39.0	7.57	0.255	113.2	21.14	188	-21.4	0.83	G	14
NGC 7144	E0	24.9	36.0	7.25	0.044	50.0	21.79	163	-20.4	0.88	G	3
NGC 7796	cD	49.9	24.0	14.52	0.141	170.4	21.53	254	-21.0	0.93	F	2
IC 1459	E3-4	26.9	55.8	7.83	0.264	45.0	21.26	296	-21.4	0.95	G	16
UGC 1382	S	80.0	16.0	23.27	...	47.4	...	167	-20.2	...	F	...

NOTE—Hubble type from RC3 (Corwin et al. 1994); central velocity dispersion  $\sigma_{R_e/8}$ , integrated colors B-V from Hyperleda <sup>a</sup>; NGC 4552 effective radius  $R_e$  from Cappellari et al. (2006), NGC 4552 surface brightness at  $1 R_e$  in g-band  $\mu_e$  (g) from Chen et al. (2010); Remaining distance, effective radius  $R_e$ , ellipticity  $e$ , major axis position angle PA, surface brightness at  $1 R_e$  in V-band  $\mu_e$  (V), and environment (C=cluster, G=group, or F=field) from Carnegie–Irvine Galaxy Survey (Ho et al. 2011); Number of galaxies in group  $N_g$  from Kourkchi & Tully (2017). UGC 1382 data from Hagen et al. (2016), see Appendix F for details.

<sup>a</sup> <http://leda.univ-lyon1.fr/>

**Table 2.** Summary of Observations

Galaxy	Date	Grating	Slit Width	Exposure Time	PA
			(arcsec)	(minutes)	E of N ( $^\circ$ )
NGC 4552 (M 89)	2018 May 11	600 $\ell$ /9 $^\circ$ 71	2.5	60	0
	2018 May 11	600 $\ell$ /10 $^\circ$ 46	2.5	60	0
	2019 April 28	600 $\ell$ /17 $^\circ$ 11	2.5	60	0
NGC 1404	2019 Dec. 2	600 $\ell$ /9 $^\circ$ 7	2.5	60	151
	2019 Dec. 2	600 $\ell$ /10 $^\circ$ 45	2.5	60	151
	2019 Dec. 3	600 $\ell$ /17 $^\circ$ 11	2.5	40	151
NGC 3923	2015 May 19/20	600 $\ell$ /9 $^\circ$ 8	2.5	40	48
	2015 May 19/20	600 $\ell$ /16 $^\circ$ 8	2.5	20	48
NGC 4697	2019 April 27	600 $\ell$ /9 $^\circ$ 71	2.5	60	0
	2019 April 27	600 $\ell$ /10 $^\circ$ 46	2.5	60	0
	2019 April 27	600 $\ell$ /17 $^\circ$ 11	2.5	60	0
NGC 5061	2019 April 29	600 $\ell$ /9 $^\circ$ 71	2.5	60	0
	2019 April 30	600 $\ell$ /10 $^\circ$ 46	2.5	80	0
	2019 April 30	600 $\ell$ /17 $^\circ$ 11	2.5	80	0
NGC 7144	2018 July 9	600 $\ell$ /9 $^\circ$ 95	2.5	80	0
	2018 July 9	600 $\ell$ /10 $^\circ$ 72	2.5	80	0
	2019 April 28	600 $\ell$ /17 $^\circ$ 11	2.5	80	0
NGC 7796	2018 July 15	600 $\ell$ /9 $^\circ$ 95	2.5	120	0
	2018 July 15	600 $\ell$ /10 $^\circ$ 72	2.5	120	0
IC 1459	2014 Sept. 19/20	600 $\ell$ /9 $^\circ$ 78	1.5	30	0
	2014 Sept. 19/20	600 $\ell$ /16 $^\circ$ 6	1.5	120	0
IC 1459	2015 May 19	600 $\ell$ /9 $^\circ$ 78	2.5	20	30
	2015 May 19	600 $\ell$ /16 $^\circ$ 6	2.5	20	30

2014–2019. For each run, nearby bright galaxies were selected that were observable on the allocated nights. Most galaxies are elliptical or S0/E0, and most are located in group or cluster environments, only NGC 7796 is classified as a field galaxy. One galaxy, UGC 1382, was believed to be an early-type galaxy, but was classified as a giant low-surface brightness galaxy (LSBG) by Hagen et al. (2016), with a surrounding disk and spiral arms. Our stellar population analysis of UGC 1382 is detailed in Appendix F.

The galaxies’ central velocity dispersions are in the range  $160\text{--}300\text{ km s}^{-1}$ , and their physical sizes span  $R_e \sim 2.2\text{ kpc}$  (NGC 1404) to  $8.8\text{ kpc}$  (NGC 3923). We list details on the sample galaxies in Table 1, and summarise the observations in Table 2.

For all galaxies we obtained optical longslit spectra in the ranges  $\sim 4000\text{--}6600\text{ \AA}$  (grating  $600\ell/\sim 9^\circ 8$ ), and for seven galaxies in addition the Ca triplet (CaT) range  $\sim 8100\text{--}8600\text{ \AA}$  (grating  $600\ell/\sim 17^\circ$ ). For NGC 7796 we do not have spectra in the CaT range, because IMACS showed a strong fringing signal, and the spectroscopic flat spectra taken during the day were not sufficient to correct it.

For some galaxies, we observed two slightly different settings at optical wavelengths (NGC 1404, NGC 4552, NGC 4697, NGC 5061, NGC 7144, NGC 7796), to ensure that the spectra cover the full wavelength range from  $\sim 3700\text{--}6700\text{ \AA}$  without gaps. However, for IC 1459 and NGC 3923 we observed only one optical grating angle, which causes three gaps, with each about  $60\text{ \AA}$  width, in the spectra, as IMACS consists of four chips along the wavelength direction. We have two sets of observations for IC 1459 at different position angles (PAs),  $30^\circ$  offset, and different slit widths. We analyzed these spectra separately.

## 2.2. Data Reduction and Processing

We used a combination of IRAF<sup>1</sup> and custom-made IDL scripts for data reduction. Our reduction steps include bias subtraction, bad pixel detection and cosmic ray removal, distortion correction, and wavelength calibration to air wavelengths using He/Ne/Ar/Hg arc lamp exposures. For the CaT spectra (grating  $600\ell/\sim 17^\circ$ ), we had an additional step in order to correct for fringes. Following Lonoce et al. (2021), we divided the science frames by spectroscopic flat field frames, which were

taken close in time to the observations. This step was performed before distortion correction.

The optical spectra of NGC 7144 and NGC 7796 show a wedge of additional light contamination in the lower right part of the reddest chip (chip 1). This is probably caused by stray light from the Hall effect device on one of the grating tilt mechanisms (Dave Osip, priv. communication). We decided not to use the spectral region affected by it, which limits our useful optical wavelength range to  $< 6640\text{ \AA}$ .

The IMACS slit length is  $15'$  along two chips, i.e. about  $7'$  on a single chip. This allowed us to use the exposure itself to estimate the sky background, at a distance of  $\gtrsim 2 R_e$  from the galaxy center. We used the IRAF tool BACKGROUND. For NGC 3923 only, we used a slightly different approach (see Feldmeier-Krause et al. 2020 for details), which resulted in a similar S/N compared to using BACKGROUND subtraction. In short, we first extracted a sky spectrum at  $> 3 R_e$  and subtracted it, and then we removed sky residuals using PPF (Cappellari & Emsellem 2004; Cappellari 2012, 2017). We combined individual exposures of a galaxy in the same setting before we extracted the spectra. We simultaneously extracted spectra from the flat field exposures, processed in the same way as the science exposures, and corrected the extracted optical science spectra along the dispersion axis. The CaT spectra had already been flat-field corrected before sky subtraction, when we corrected for fringes. We extracted spectra in a finer radial sampling in the center ( $\sim 0.01 R_e$ ), but increased the extraction windows at larger radii to obtain  $S/N > 50$ , typically up to  $\sim 0.25 R_e$  width. For most galaxies, the outermost bin extends to  $1 R_e$ . The geometric mean of the extraction window along the slit is listed in Table 6 as  $x/R_e$ . When considering the slit width we obtain the geometric distance or radius from the galaxy center as  $r/R_e$ . We derived the flux calibration from standard star observations, observed with the same settings as the science frames and processed in a similar way. The only exception are the data observed with a slit width of  $1''.5$  (IC 1459 observed 2014 Sept. 19/20), for which we only have standard star observations with slit width  $2''.5$ . We compared the flux calibrated spectra with the IC 1459 data that were observed with a slit width of  $2''.5$  (observed 2015 May 19). We found that the flux calibration for the bluest wavelength chip is not satisfactory, as it results in an overestimation of the flux towards shorter wavelengths ( $\lesssim 3900\text{ \AA}$ ) for the slit width  $= 1''.5$  data. For this reason, we do not use the spectra on the bluest chip ( $3600\text{--}4380\text{ \AA}$ ). We corrected the atmospheric transmission using the ESO tool MOLECFIT (Kausch et al. 2015; Smette et al. 2015).

<sup>1</sup> IRAF is distributed by the National Optical Astronomy Observatory, which is operated by the Association of Universities for Research in Astronomy (AURA) under a cooperative agreement with the National Science Foundation.

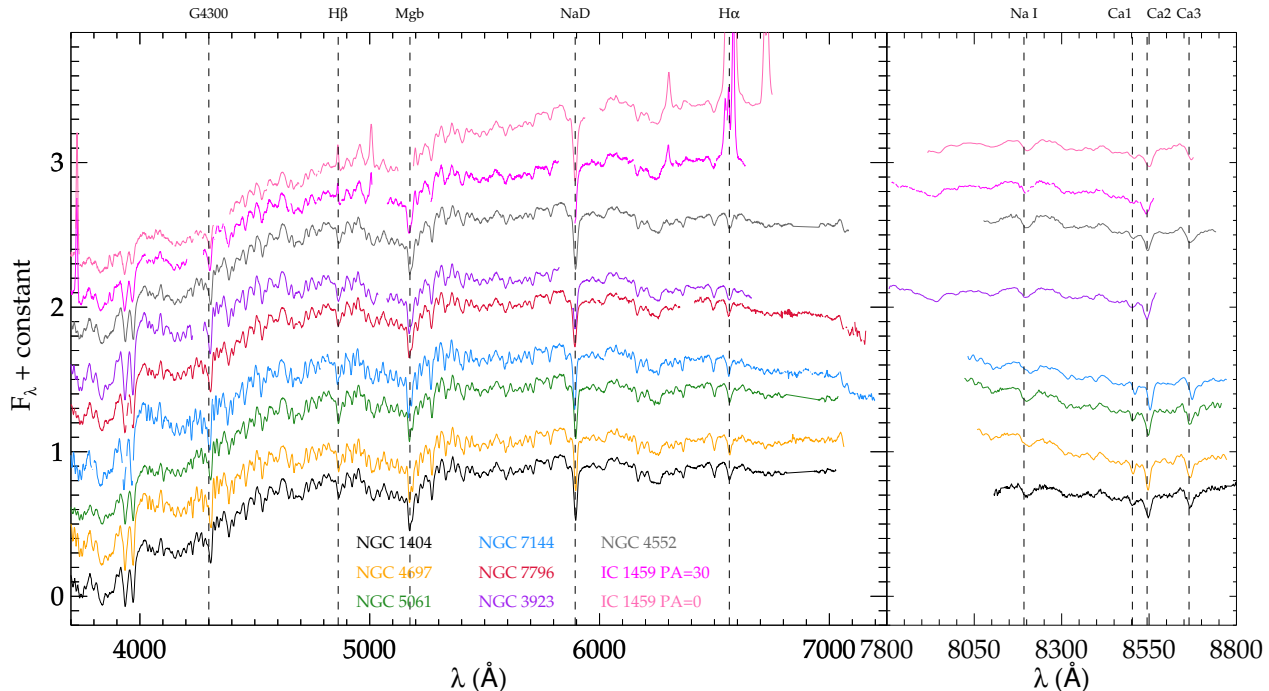


**Figure 1.** Central spectra of all galaxies in our sample, denoted with different colors. The spectra are normalised and shifted to rest wavelength. Note the slightly different wavelength regions and the missing CaT region for NGC 7796 (red).

In order to prepare the reduced spectra for our spectral fitting, we performed the following steps: We corrected the galaxy rotation as outlined in Appendix A, we corrected all spectra for Galactic extinction using the map of Schlafly & Finkbeiner (2011), and converted the spectra from air to vacuum wavelengths. We measured the spectral resolution of our data using arc line exposures. The full-width-half-maximum (FWHM) is usually  $\sim 5.5 \text{ \AA}$ , with small variations between observing runs. Only the data observed with a slit width  $1''.5$  have a higher spectral resolution with FWHM  $\sim 3 \text{ \AA}$ . For our analysis we use Conroy et al. (2018) template spectra, which have a spectral resolution of  $\sigma = 100 \text{ km s}^{-1}$ . We convolved our spectra to a spectral resolution of  $100 \text{ km s}^{-1}$  if the spectral resolution of the data was less than  $100 \text{ km s}^{-1}$ .<sup>2</sup> The convolution was necessary for the entire spectra observed with the  $1''.5$  slit, and for the CaT region ( $> 8000 \text{ \AA}$ ) of the  $2''.5$  slit spectra. We resampled all spectra to a  $1.25 \text{ \AA}$  spaced wavelength grid, in order to decrease the time required for a fit. Finally, we combined the spectra with different grating angles for each galaxy and radius bin, with exception of IC 1459, where we kept the two sets at different PA and slit widths separate. We show the central spectra of all galaxies in our

sample in Figure 1. In Appendix B and Figure 12, we show the S/N of our data as a function of wavelength and radial extraction region, for each individual galaxy. In summary, the S/N lies usually in the range of 50 to  $300/\text{\AA}$ .

### 3. SPATIALLY RESOLVED STELLAR POPULATIONS

We applied full spectral fitting using the PYTHON code PYSTAFF (Python Stellar Absorption Feature Fitting, Vaughan et al. 2018b) to measure 12 stellar population parameters. First we summarise the method, and then we present our results.

#### 3.1. Method

##### 3.1.1. Spectral Fitting

The code PYSTAFF applies full spectral fitting to find the best-fit single stellar population (SSP) using the models by Conroy et al. (2018). We fit the stellar population parameters age  $t$ , metallicity  $[Z/H]$ , nine elemental abundances ( $[Na/H]$ ,  $[C/H]$ ,  $[O/H]$ ,  $[Ca/H]$ ,  $[Fe/H]$ ,  $[N/H]$ ,  $[Ti/H]$ ,  $[Mg/H]$ ,  $[Si/H]$ ), and the IMF slope. In addition, we fit the gas velocity and dispersion, gas emission flux (see Appendix C.1 for details), and the stellar velocity and velocity dispersion  $\sigma$ . We show the stellar velocity dispersion profiles, corrected for stellar rotation as described in Appendix A, in Figure 2.

We used the bounds  $[1, 14 \text{ Gyr}]$  for age,  $[-1.5, 0.3 \text{ dex}]$  for  $[Z/H]$ ,  $[-0.45, 1.0 \text{ dex}]$  for Na,  $[-0.2, 0.3 \text{ dex}]$  for

<sup>2</sup> For the spectral fitting in Section 3, we convolved the template spectra to the spectral resolution of the data in regions where it was  $> 100 \text{ km s}^{-1}$ .

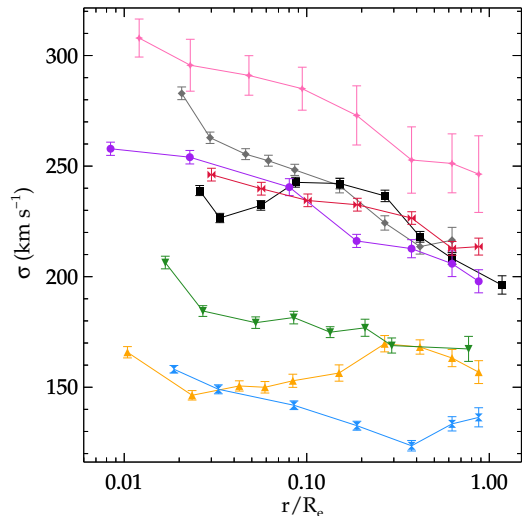


**Figure 2.** Velocity dispersion  $\sigma$  as a function of radius for all galaxies, denoted by different colored symbols as in Figure 1.

C, [0, 0.45 dex] for O, [-0.45, 0.45 dex] for Ca, Fe, N, Ti, Mg, and Si, and [0.3, 3.5] for the IMF slope. We combined the two IMF slope parameters  $x_1$  and  $x_2$  of the SSP models (in the initial stellar mass ranges 0.08–0.5  $M_\odot$  and 0.5–1.0  $M_\odot$ ) to a single slope by forcing  $x_1$  equal to  $x_2$ . The IMF slope at  $>1.0 M_\odot$  is fixed to the Salpeter (1955) slope. PYSTAFF utilises the EMCEE package (Foreman-Mackey et al. 2013) to explore the large parameter space. We chose 100 walkers and 8000 steps.

We also ran fits with two IMF slope parameters instead of one, for the two mass ranges 0.08–0.5  $M_\odot$  and 0.5–1.0  $M_\odot$ . However, the two parameters  $x_1$  and  $x_2$  are anti-correlated (see also Feldmeier-Krause et al. 2020; Lonoce et al. 2021), which led us to use only one slope for the full mass range 0.08–1.0  $M_\odot$  instead. The differences for the other parameters when using two instead of one IMF slope are within the  $1\sigma$  uncertainties.

We explored covariances of our fitting parameters. The probability distribution functions (PDFs) of our fits show some correlations, and the most common are a positive correlation between C and O, Fe and Mg, and an anti-correlation of age and [Z/H]. These covariances are also shown in the upper right off-diagonal of Figure 9. For each PYSTAFF stellar population fit, we computed the Spearman rank correlation coefficient  $\rho$  of the PDFs of two stellar population parameters. We combined these measurements of  $\rho$  to one mean  $\rho$  per galaxy and parameter set, which we show as ellipses. A near circular shape and dotted lines mean no or a weak covariance ( $|\rho| < 0.4$ ), a dot-dashed line a moderate ( $0.4 \leq |\rho| < 0.6$ ), a dashed line a strong ( $0.6 \leq |\rho| < 0.8$ ),

a solid line a very strong ( $|\rho| \geq 0.8$ ) covariance of two parameters. The covariances are included in the uncertainty estimates of our fitting results as listed in Table 6.

### 3.1.2. Gradient Fitting

We measured radial gradients of the final single stellar population parameters. We used orthogonal distance regression (SCIPY package ODR) to fit a log-linear relationship for each galaxy and stellar population property  $Y$  as a function of the geometric bin center or radius  $r$ , defined as  $Y = \nabla_r \cdot \log(r/R_e) + B_r$ . The quantity  $\nabla_r$  denotes the radial gradient per  $\log(r/R_e)$ ;  $B_r$  denotes the stellar population value at  $1 R_e$  ( $\log(r/R_e)=0$ ). We do not have an uncertainty for  $r$ , and used only the errors of the stellar population parameter in the fits. This means that the ODR fits as a function of  $\log(r/R_e)$  are equivalent to least-squares minimization. We fit the logarithmic age,  $\log t$ . We excluded data points located within the central  $1''$  from the gradient fits, in order to avoid seeing effects.

Some stellar population gradients are not well described with a linear function, and we obtain large reduced  $\chi^2$  with our linear fits. We fit quadratic models and found them significantly better than the linear models for [Z/H] for four galaxies (NGC 4552, NGC 1404, NGC 4697, NGC 5061). For NGC 1404 and NGC 5061 the quadratic fit for [O/Fe] is better, and for NGC 5061 also [Na/Fe], [N/Fe], and the IMFs are better described with a quadratic model as a function of radius. Nevertheless, we use the linear model fits for an easier comparison among galaxies and parameters.

## 3.2. Single Stellar Population Results

In this section we present our results of the stellar populations and their radial gradients for our eight early-type galaxies. For easier comparison with the literature, we converted the elemental abundances from [X/H], as they are parameterised in the models, to [X/Fe] by subtracting [Fe/H]. The exceptions are [Fe/H] and [Z/H], which remain unchanged. We show the resulting radial stellar population profiles in Figure 3 (top), and list the results in Table 6 for each galaxy. In the panels of elemental abundances we show the reference values of the Conroy et al. (2018) model response functions, which are used to derive elemental abundances (see Appendix C.2) as horizontal dotted lines.<sup>3</sup> The radial gradients

<sup>3</sup> The response function reference values are for [X/H], and not for [X/Fe] as in the plot. However, since [Fe/H]  $\approx 0$  dex in all our fits, we neglected the difference to illustrate where the reference values of the response functions are.

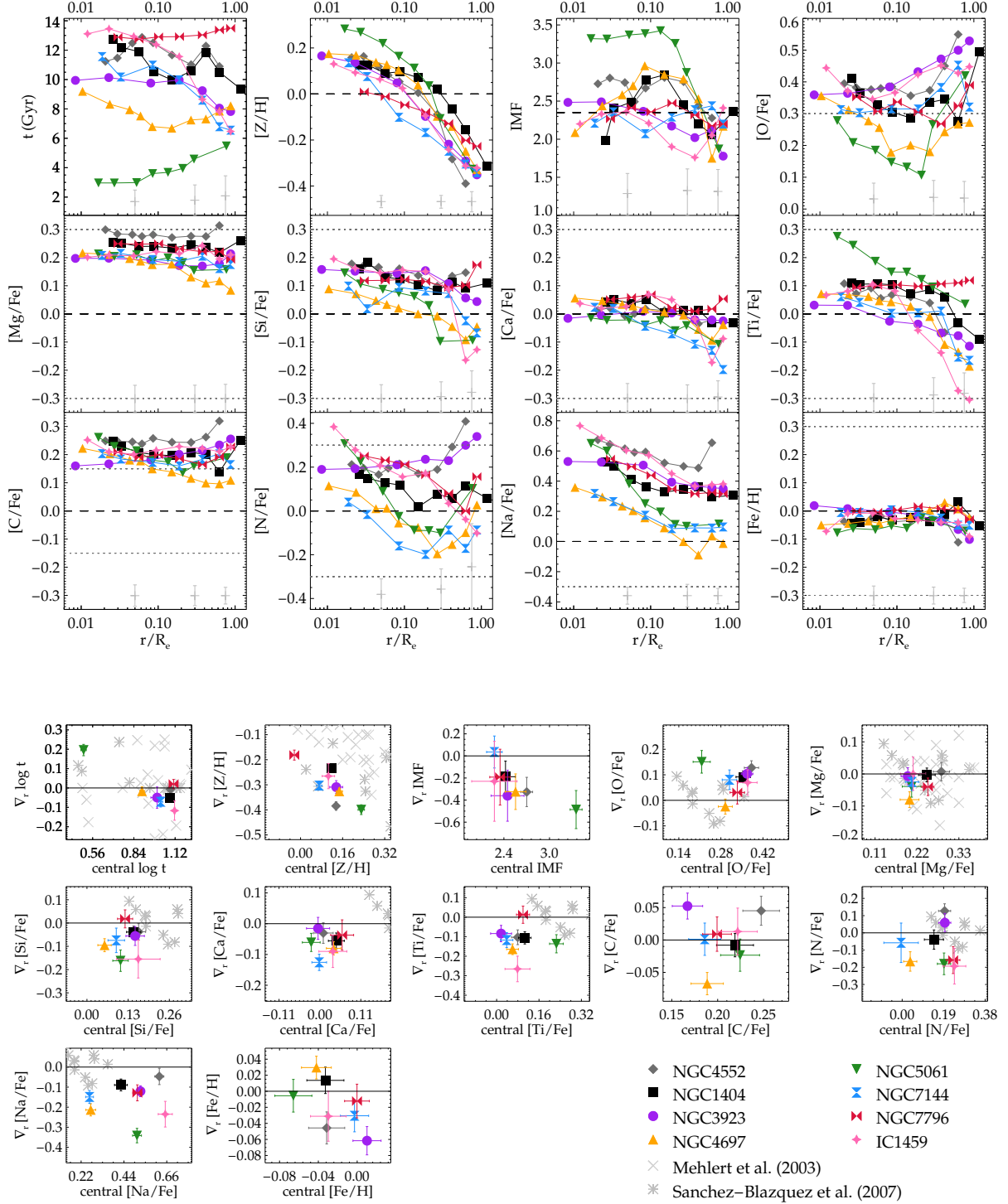


**Figure 3.** Top: Stellar population profiles for each galaxy as a function of  $r/R_e$ . Different colors and symbols denote different galaxies, as outlined in the figure legend; Gray plus symbols on the bottom of each panel are median uncertainties in three radial ranges; Horizontal dashed lines are for solar metallicity and elemental abundances; Horizontal dotted lines for elemental abundances illustrate the approximate reference values of the Conroy et al. (2018) model response functions, which were interpolated and extrapolated to measure elemental abundances. Bottom: Radial trends  $\nabla_r$  for each stellar population parameter and galaxy, as a function of the error-weighted mean of the central ( $r \leq 0.125 R_e$ ) values. Horizontal lines denote constant value with radius.

$\nabla_r$  are shown in Figure 3 (bottom) as a function of the central value, computed as the error-weighted mean of the measurements located at  $r \leq 0.125 R_e$ .

The low-mass IMF slope at  $<1 M_\odot$  scatters around a median value of 2.44, with values ranging from 1.8 to 3.4. NGC 5061 has a significantly steeper low-mass IMF slope than the Salpeter (1955) IMF slope of 2.35, with values up to 3.4 in the central  $0.1 R_e$ , but the low-mass IMF slope decrease at larger radii. Some galaxies exhibit a constant low-mass IMF slope with radius, though there are also galaxies with a decreasing low-mass IMF with radius ( $\nabla_r \text{IMF} = -0.4/\log(r/R_e)$ ).

Most galaxies are older than 8 Gyr, with some exceptions at larger radii. NGC 4697 has an intermediate age (6.7-9.2 Gyr); NGC 5061 is young,  $<6$  Gyr. Our linear age gradient ranges from  $-0.11$  to  $+0.18$  dex/ $\log(r/R_e)$ . NGC 5061 is the only galaxy with a significantly increasing age with radius, all other galaxies have a decreasing or constant age.

All galaxies have a negative [Z/H] gradient, with super-solar or roughly solar central values and decreasing to  $\sim -0.35$  dex. The galaxy with the steepest decreasing [Z/H] is NGC 5061 ( $-0.37$  dex/ $\log(r/R_e)$ ). NGC 7796 ( $-0.17$  dex/ $\log(r/R_e)$ ) on the other hand has the most shallow decreasing [Z/H], and also the lowest [Z/H] value in the center (0.01 dex). Interestingly, this galaxy is located in a low-density environment, whereas all of the other galaxies are either in clusters or groups (see Table 1).

Our measurements of [Fe/H] are close to solar (usually about  $-0.1$  to  $0.07$  dex) and either constant with radius or with a shallow slope ( $-0.06 \lesssim |\nabla_r [\text{Fe}/\text{H}]| \lesssim 0.03$  dex/ $\log(r/R_e)$ ); [O/Fe] spans 0.1 to 0.55 dex; [Mg/Fe] is super-solar ( $\sim 0.08$  to  $0.3$  dex); [Si/Fe] lies mostly within  $-0.16$  to  $0.2$  dex; [Ca/Fe] is near solar ( $\sim -0.2$  to  $0.1$  dex); [Na/Fe] is mostly super-solar ( $\sim 0.0$  to  $0.8$  dex); [C/Fe] is always super-solar ( $\sim 0.1$  to  $0.3$  dex), [N/Fe] and [Ti/Fe] have a wide spread ( $\sim -0.2$  to  $0.4$  dex and  $-0.3$  to  $0.3$  dex). For most elements, the mean abundance measurement uncertainties are  $\sim 0.05$  dex, and increase with radius, reflecting the decreasing S/N. The uncertainties of [N/Fe] are the largest, and they increase by a factor three from the center to the outer region, see gray colored symbols in the top panels of Figure 3.

We obtain the steepest radially decreasing gradients for [Na/Fe], [N/Fe], and [Ti/Fe] ( $\nabla_r [\text{X}/\text{Fe}] \lesssim -0.2$  dex/ $\log(r/R_e)$  for some galaxies, though the typical gradients are less steep ( $\nabla_r \sim -0.1$  to  $-0.2$  dex/ $\log(r/R_e)$ ). [Fe/H], [Mg/Fe], and [C/Fe] have more shallow radial trends, with  $-0.1 < \nabla_r < 0.05$  dex/ $\log(r/R_e)$ , see also Fig. 3, bottom. For a given element, the range of possible values in the sample increase

**Table 3.** Linear fit to the stellar population parameters (interpolated at  $0.1 R_e$ ) as a function of  $\sigma_{R_e/8}$ .

Parameter	Slope	Intercept	$\chi_{\text{red}}^2$
t	$0.038 \pm 0.007$	$2.6 \pm 1.5$	5.0
[Z/H]	$0.0020 \pm 0.0003$	$-0.47 \pm 0.06$	21.2
IMF	$0.0004 \pm 0.0025$	$2.4 \pm 0.6$	1.6
[O/Fe]	$0.0009 \pm 0.0004$	$0.13 \pm 0.10$	1.1
[Mg/Fe]	$0.0005 \pm 0.0003$	$0.11 \pm 0.07$	0.8
[Si/Fe]	$0.0008 \pm 0.0004$	$-0.07 \pm 0.09$	0.4
[Ca/Fe]	$0.0008 \pm 0.0004$	$-0.16 \pm 0.08$	0.6
[Ti/Fe]	$0.0006 \pm 0.0005$	$-0.08 \pm 0.11$	0.8
[C/Fe]	$0.0005 \pm 0.0003$	$0.09 \pm 0.06$	0.5
[N/Fe]	$0.0028 \pm 0.0007$	$-0.51 \pm 0.17$	0.9
[Na/Fe]	$0.0036 \pm 0.0004$	$-0.44 \pm 0.10$	1.4
[Fe/H]	$-0.0000 \pm 0.0002$	$-0.00 \pm 0.05$	0.5

with galaxy radius. This may indicate that the galaxies in our sample have different minor merger histories. The portion of stars brought to the galaxy via satellite accretion is larger at outer radii than in the center, where the stellar populations are dominated by in situ formation.

We compare our results to stellar population measurements of the same and similar galaxies in the literature in Appendix C.4. In Appendix D.2 we use the elemental abundances to constrain the star formation timescales. In Appendix E we summarise the results for each galaxy individually.

#### 4. CORRELATIONS OF STELLAR POPULATION PARAMETERS

##### 4.1. Correlations of Central Stellar Population Parameters with Central Velocity Dispersion

Several studies found global correlations of galaxy overall stellar population parameters (e.g. age, [Z/H], [Mg/Fe]) with the velocity dispersion, using individual galaxies (e.g. Trager et al. 2000b; Kuntschner et al. 2010) or stacked spectra (e.g. Graves et al. 2009; Thomas et al. 2010; Worthey et al. 2014; Conroy et al. 2014). Here, we test if we can reproduce correlations using our large set of stellar population parameters. Such correlations are important to understand the assembly and evolution of galaxies.

We investigated correlations with the velocity dispersion within  $R_e/8$ ,  $\sigma_{R_e/8}$ , using the Hyperleda reference values from Table 1. We also computed correlations with the total B-band magnitude  $M_B$ , and the dynamical mass  $\log(M_{\text{dym}}) = 2 \log(\sigma) + \log(R_e) + 3.1$ , with  $R_e$  in pc (Spolaor et al. 2009), using the values for  $M_B$ , and  $R_e$  as listed in Table 1. Since correlations with the latter



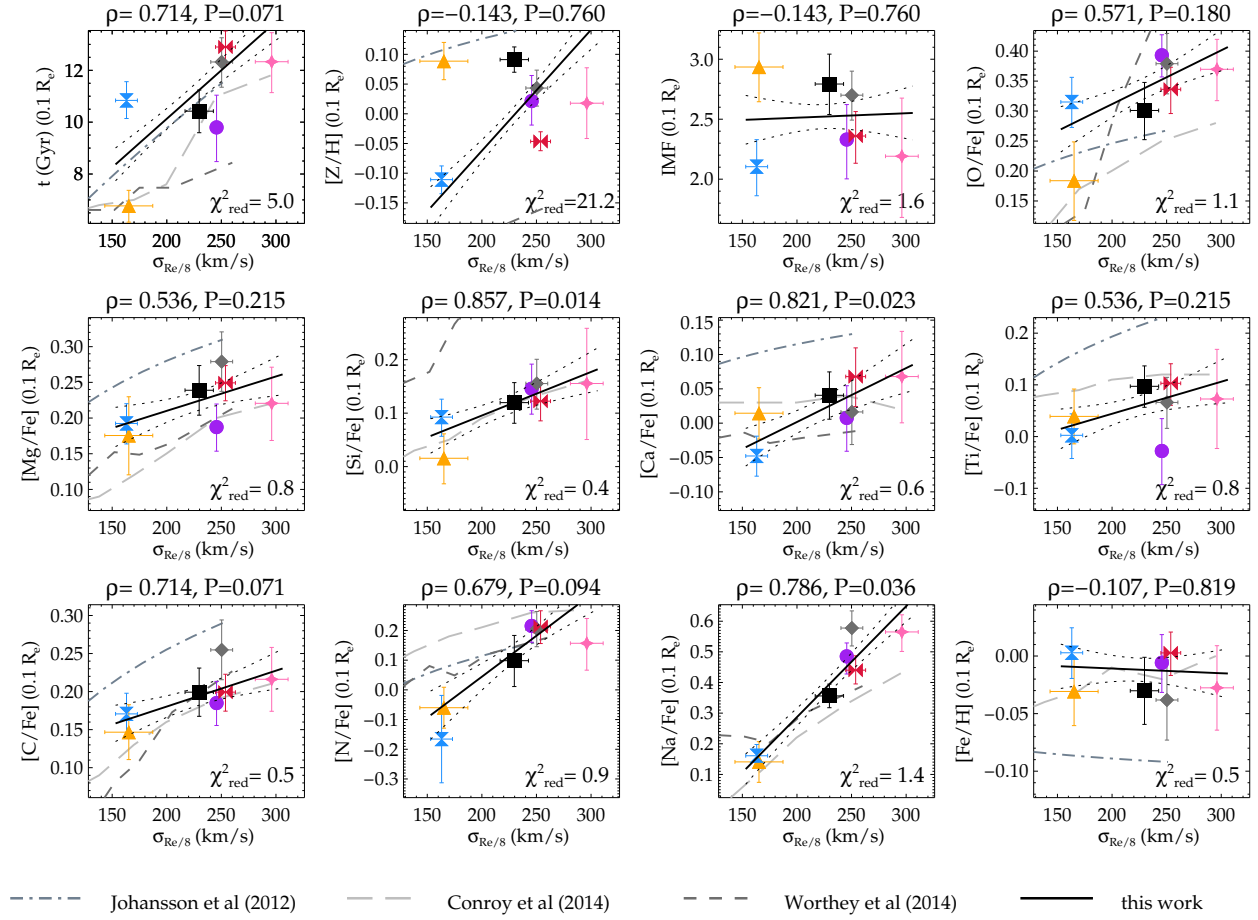


**Figure 4.** Stellar population parameters (interpolated at  $0.1 R_e$ ) as a function of  $\sigma_{R_e/8}$  for seven old early-type galaxies, denoted by different colored symbols. Spearman rank coefficient  $\rho$  and probability  $P$  are shown at the top of each panel. The solid black line shows a linear fit, the gray dotted lines the  $1\text{-}\sigma$  uncertainties of the fit, the respective  $\chi^2_{\text{red}}$  is denoted in the lower right corner of each panel. The dot-dashed, dashed, and long-dashed lines denote the relations found by [Johansson et al. \(2012\)](#); [Worthey et al. \(2014\)](#); [Conroy et al. \(2014\)](#).

parameters were usually less significant, we present only the correlations with  $\sigma_{R_e/8}$ . In our correlation analysis we do not consider NGC 5061, as it has a more extended star formation history and therefore the SSP results may be biased (Appendix D.1). We note that our sample size is relatively small (seven galaxies), and spans only a narrow range ( $\sigma_{R_e/8}=163\text{--}296 \text{ km s}^{-1}$ ,  $M_B=-20.3$  to  $-21.4$  mag,  $\log(M_{\text{dyn}}) = 2 \log(\sigma) + \log(R_e) + 3.1 = 11\text{--}12$ ).

We show the stellar population parameter values linearly interpolated to  $0.1 R_e$  as a function of  $\sigma_{R_e/8}$  in Figure 4. We performed linear fits, which are shown as solid black lines, the respective  $\chi^2_{\text{red}}$  are noted in the lower right corners. The linear fit results are listed in Table 3. Also shown in Figure 4 are the relations found by [Johansson et al. \(2012\)](#); [Worthey et al. \(2014\)](#); [Conroy et al. \(2014\)](#), based on the global galaxy stellar popula-

tions. [Johansson et al. \(2012\)](#) have a large data set of  $\sim 3800$  individual galaxies, while [Worthey et al. \(2014\)](#); [Conroy et al. \(2014\)](#) derived their relations from stacked galaxy spectra. This explains why our data have a larger scatter. Moreover, these studies used different methods and models. Nevertheless, we see comparable trends with  $\sigma_{R_e/8}$ .

For each parameter we computed the Spearman rank correlation coefficient  $\rho$  with  $\sigma_{R_e/8}$ , denoted on the top of each panel. There are some parameters with strong ( $|\rho| \geq 0.6$ ) or very strong ( $|\rho| \geq 0.8$ ) correlations at this radius, in particular  $[\text{Si}/\text{Fe}]$ ,  $[\text{Ca}/\text{Fe}]$ ,  $[\text{C}/\text{Fe}]$ , and  $[\text{Na}/\text{Fe}]$ .

We found no correlation of  $[\text{Z}/\text{H}]$  with  $\sigma_{R_e/8}$ , which has been reported in the literature (e.g. [Mehlert et al. 2003](#); [Thomas et al. 2010](#); [McDermid et al. 2015](#)), for

larger and/or more homogeneous samples. At a given value of  $\sigma_{R_e/8}$ , our  $[Z/H]$  values span up to 0.2 dex, which is within the range of scatter found in the literature for larger samples. We also tested whether the radial stellar population gradients  $\nabla_r$  correlate with any mass proxies. No correlations exceed  $\rho=0.58$ , only  $\nabla_r[\text{Mg}/\text{Fe}]$  and  $\nabla_r[\text{C}/\text{Fe}]$  have moderate correlations ( $\rho=0.46$  and  $0.57$ ,  $P=0.29$  and  $0.18$ ) with  $\sigma_{R_e/8}$ . Rawle et al. (2008) and Parikh et al. (2019) found no significant  $\nabla_r$  correlations, whereas Forbes et al. (2005); Spolaor et al. (2009); Ferreras et al. (2019); Krajnović et al. (2020) did, e.g. for  $\nabla_r[Z/H]$ . However, these studies have larger or more homogeneous samples, which allows them to detect correlations despite the intrinsic scatter among galaxies. It is possible that we do not find these correlations due to our small sample size, and narrow range of  $\sigma_{R_e/8}$ .

#### 4.2. Global Correlations of Central Values and Gradients

We investigated whether there are any correlations of the central stellar population parameters with each other, with the radial gradients  $\nabla_r$ , or among the gradients. We show the correlation matrixes in Figures 5, 6, 7, and 8. The upper right off-diagonal of Figures 5, 6 and all of Figure 8 are when excluding NGC 5061; the lower left off-diagonal of Figures 5, 6 and all of Figure 7 when including NGC 5061. Different colors and the eccentricity of the ellipses denote the strength of the correlations; the Spearman rank correlation coefficient  $\rho$  is also denoted on each panel.

We find a very strong positive correlation of the central  $[Z/H]$  and IMF slope. We caution that these parameters also have positive covariances in several PDFs of our fits, though on average the covariance is weak to moderate (upper right off-diagonal of Figure 9). We find other strong correlations of central values for various combinations of elemental abundances, e.g.  $[\text{Na}/\text{Fe}]$  with  $[\text{N}/\text{Fe}]$  and  $[\text{Si}/\text{Fe}]$ , or  $[\text{O}/\text{Fe}]$  with  $[\text{Si}/\text{Fe}]$ . However, these parameters have no strong covariances of their PDFs in our fits, with only  $[\text{Na}/\text{H}]$  and  $[\text{O}/\text{H}]$  showing moderate covariances in some fits. Most of the correlations in Figure 5 are positive, which is expected for elements that are, at least partially, produced by the same process, like  $\alpha$  elements in massive stars; O and Na, which are produced in both high-mass and to some extent in intermediate-mass stars; C and Ti, both produced in high mass stars; or N and Na, which are produced in intermediate-mass stars.

As shown in Figure 6, we find several correlations among stellar population gradients. As a consequence,  $[\text{N}/\text{Fe}]$  and  $[\text{Na}/\text{Fe}]$  not only correlate in the center, but

also at larger radii. Also the radial gradients of various  $\alpha$  elements correlate with one another (e.g. O and Mg, Si and Ti).

Further, we obtain an anti-correlation of the central  $[Z/H]$  with  $\nabla_r[Z/H]$  (Figures 7 and 8), which was also found by Sánchez-Blázquez et al. (2007) and Rawle et al. (2008). It is also shown in Figure 3. This means that the steepest  $\nabla_r[Z/H]$  is found in galaxies with high central  $[Z/H]$ , and that at  $1 R_e$  the range of  $[Z/H]$  values in our data set is more narrow. Likewise, the central  $[Z/H]$  anti-correlates with  $\nabla_r\text{IMF}$  such that galaxies with high central  $[Z/H]$  (and a more bottom-heavy IMF slope) tend to have a steeper decreasing  $\nabla_r\text{IMF}$ . Thus, the range of possible IMF slope values at  $1 R_e$  is narrower (1.7-2.4) than at  $0.01 R_e$  (2-3.3).

There are several further correlations of central stellar population parameters with another parameter's radial gradient. Some of the cases have only a strong correlation when excluding NGC 5061 (e.g.  $[\text{O}/\text{Fe}]$  with  $\nabla_r[\text{O}/\text{Fe}]$ ), and a weak correlation otherwise. They require further confirmation, as they may be caused by the low number of only seven objects, spanning a relatively narrow range of parameters.

#### 4.3. Correlations of Local Values for Individual Galaxies

Besides the correlations of our entire sample of galaxies, we also studied whether the local parameters of the individual galaxies correlate. We measured the Spearman rank correlation coefficients of our 12 stellar population parameters with each other, the local velocity dispersion  $\sigma$ , and the radius  $r/R_e$ . As for the radial gradient fitting, we omitted the most central measurements, as the spectrum is likely affected by seeing. We found several strong correlations ( $|\rho|>0.6$ ) and even some very strong correlations ( $|\rho|>0.8$ ). However, except for  $[Z/H]$  with  $r/R_e$ , the correlations never hold for all eight galaxies. Often the correlation for at least one galaxy is very weak, or even in the opposite direction. We show the parameter combinations in the lower left off-diagonal of Figure 9. Different colored ellipses denote different galaxies, solid lines a very strong ( $|\rho| \geq 0.8$ ), dashed lines a strong ( $0.6 \leq |\rho| < 0.8$ ), dot-dashed lines a moderate ( $0.4 \leq |\rho| < 0.6$ ), and dotted lines a weak or no correlation ( $|\rho| < 0.4$ ). On top of each panel we list the numbers of galaxies in different ranges of  $\rho$  ( $\rho \leq -0.8/ -0.8 < \rho \leq -0.6/ -0.6 < \rho < -0.4/ -0.4 < \rho < 0.4/ 0.4 < \rho < 0.6/ 0.6 \leq \rho < 0.8/ \rho \geq 0.8$ ). We also list the parameter combinations with at least five galaxies with a strong local correlation in Table 4.

For a large number of galaxies we find high negative correlations with  $r/R_e$  (bottom row in Figure 9),

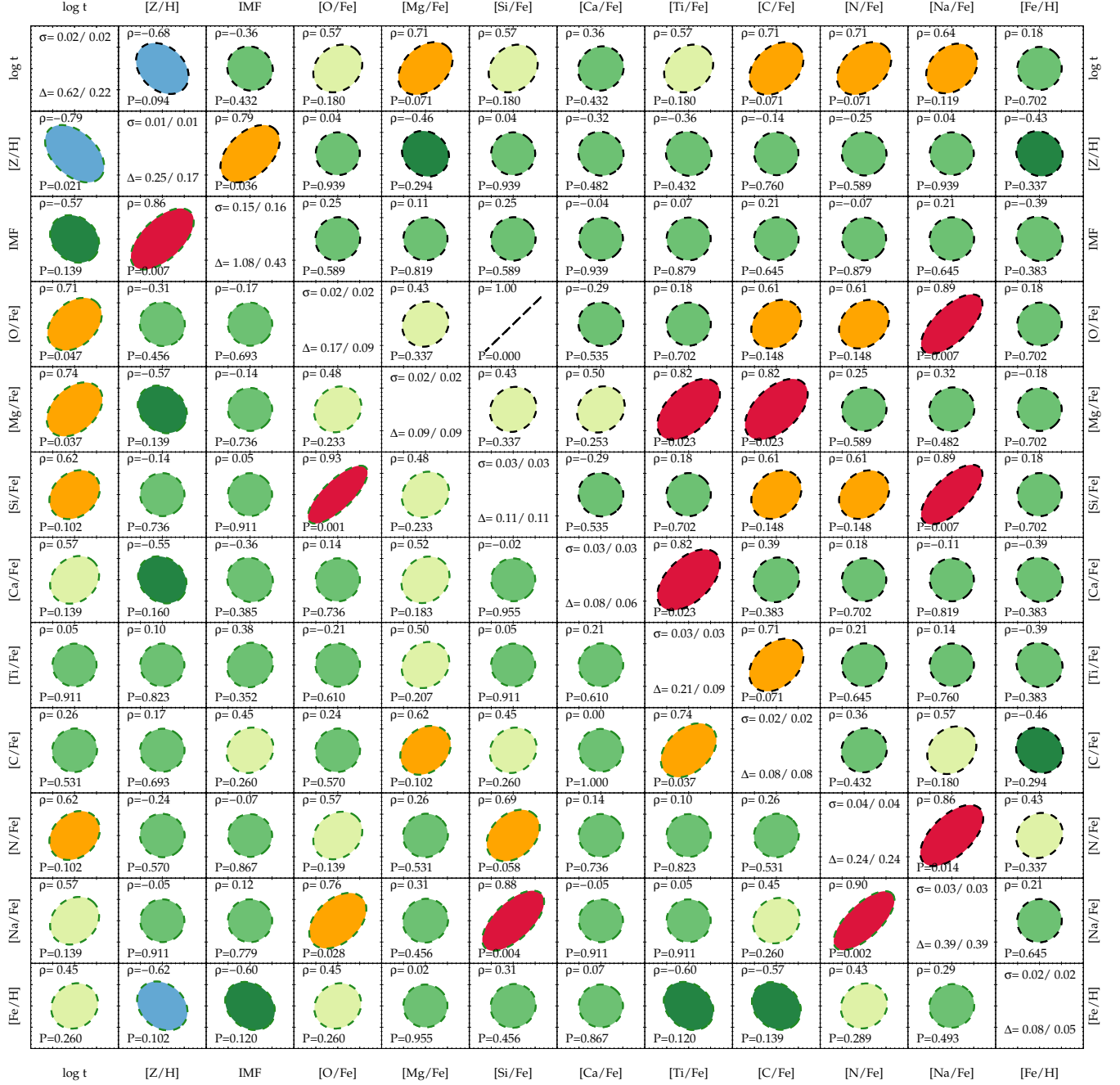


**Figure 5.** Correlation matrix for Central Stellar Population Parameters (error-weighted mean values at  $r \leq 0.125 R_e$ ). Larger eccentricities signify stronger correlations, i.e. greater  $|\rho|$ . Upper right off-diagonal cells when excluding NGC 5061, lower left when including NGC 5061. Strong positive (negative) correlations with  $\rho > 0.6$  ( $\rho < -0.6$ ) are marked with orange (light blue), very strong positive (negative) correlations with  $\rho > 0.8$  ( $\rho < -0.8$ ) with red (dark blue). Weak to moderate correlations ( $-0.6 \leq \rho \leq 0.6$ ) are shown in different shades of green.  $\rho$  and  $P$  are denoted in each panel, the numbers in the diagonal panels denote the mean uncertainty  $\sigma$  and the range of values  $\Delta$ , with and without NGC 5061, respectively, for each parameter.

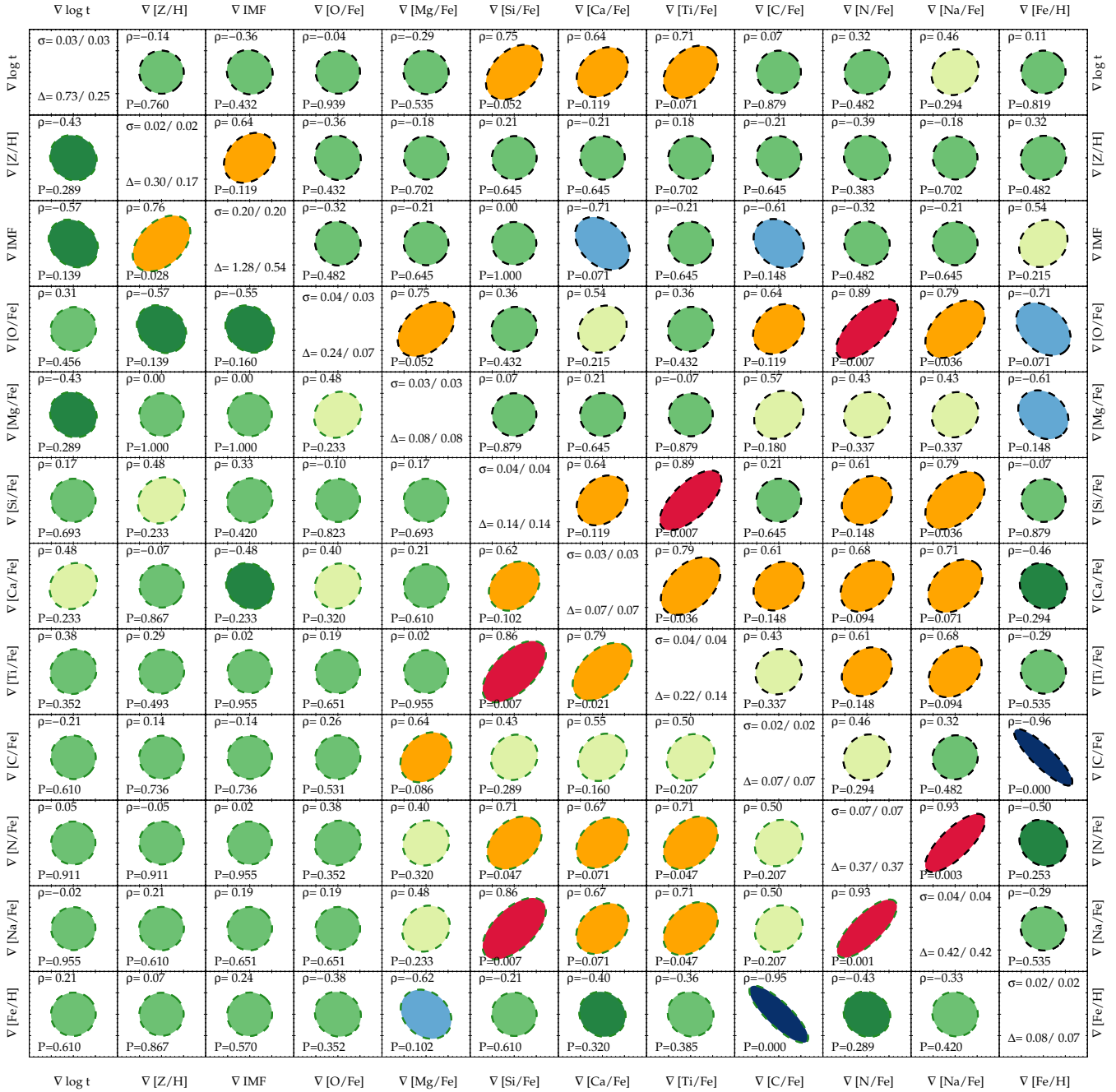
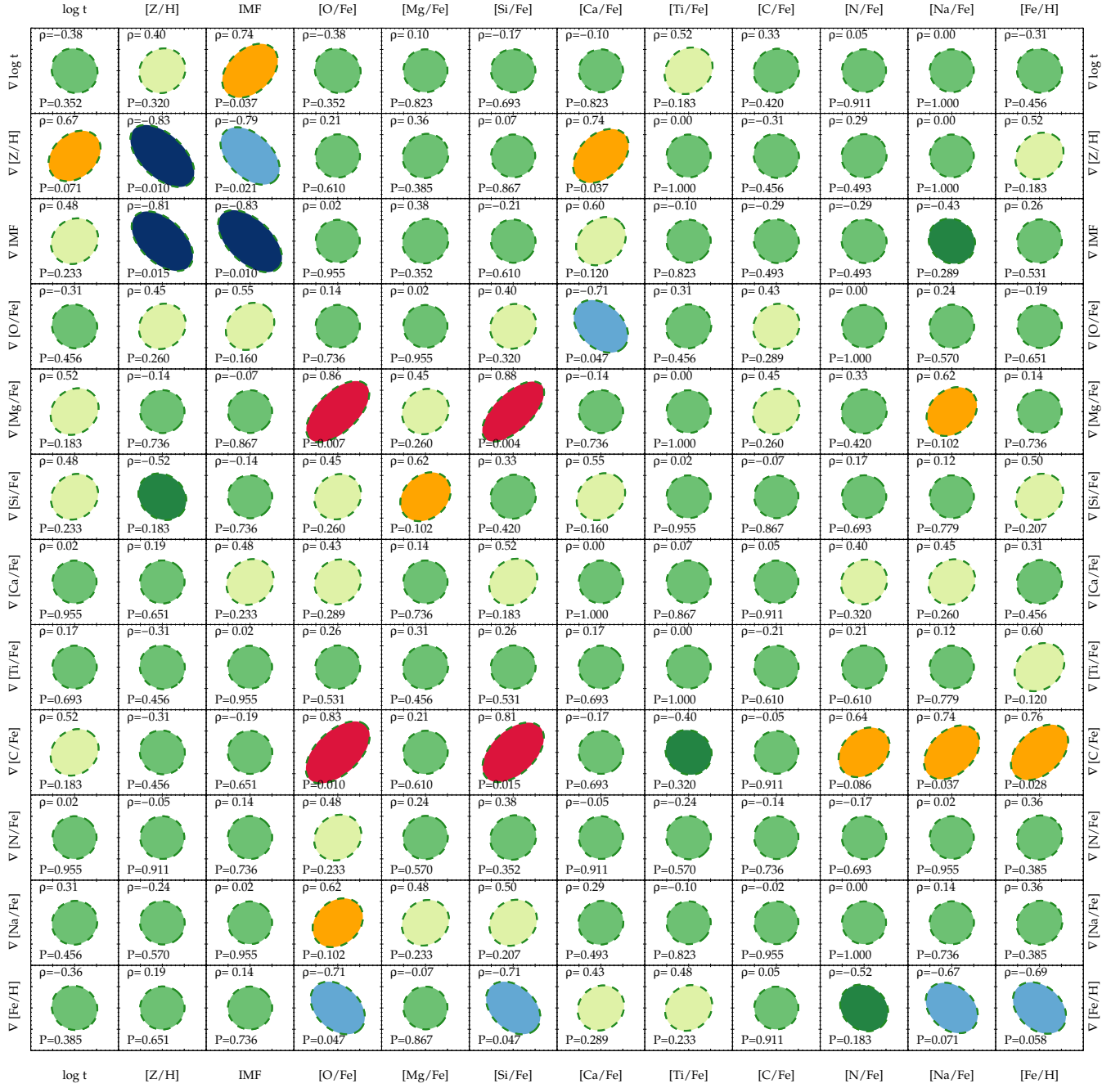


Figure 6. Correlation matrix for Radial Gradients  $\nabla_r$  of Stellar Population Parameters, colors and symbols as in Figure 5.



**Figure 7.** Correlation matrix for Central Stellar Population Parameters (error-weighted mean values at  $r \leq 0.125 R_e$ ) with Radial gradients  $\nabla_r$  for all eight galaxies (including NGC 5061).

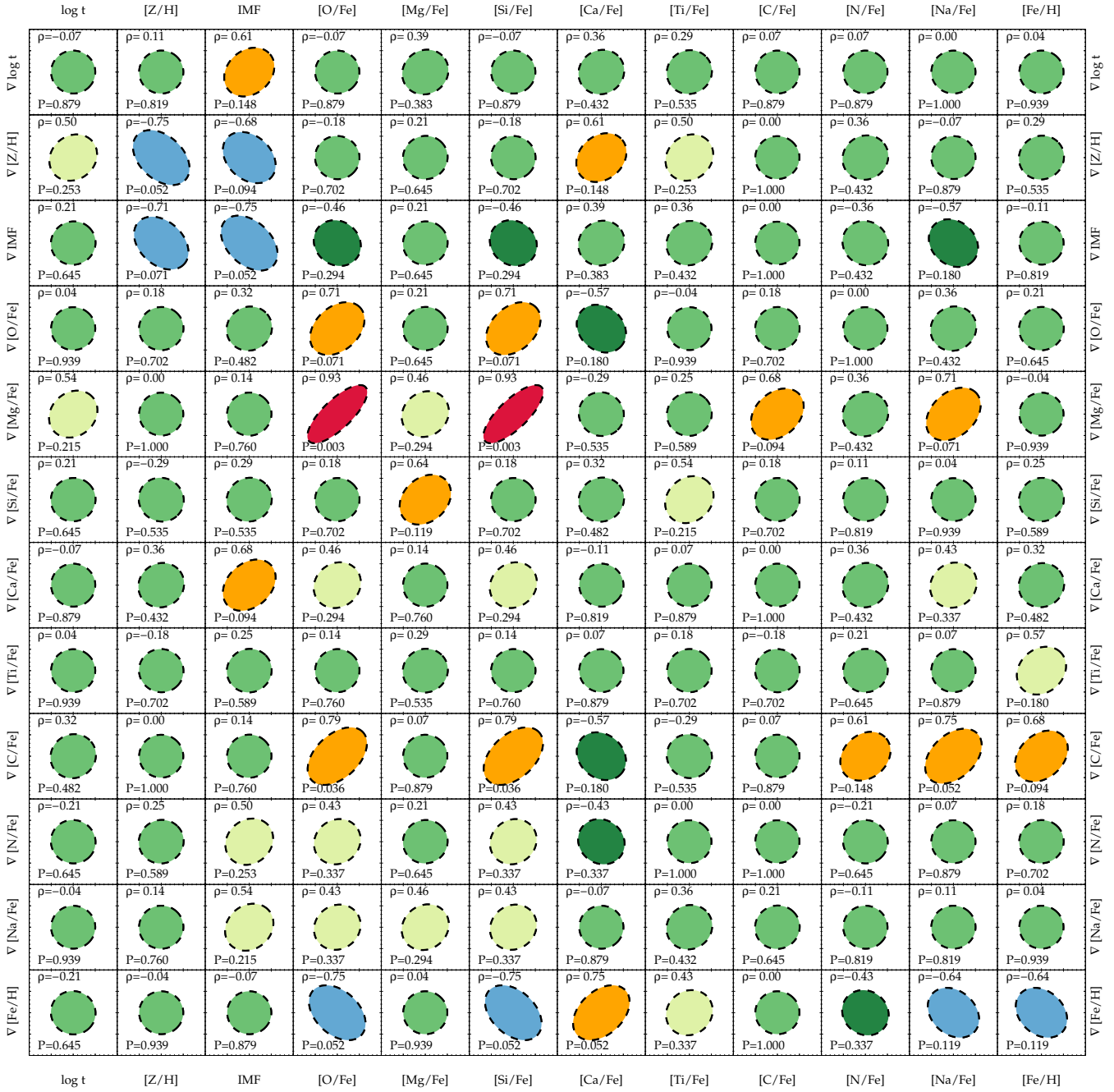
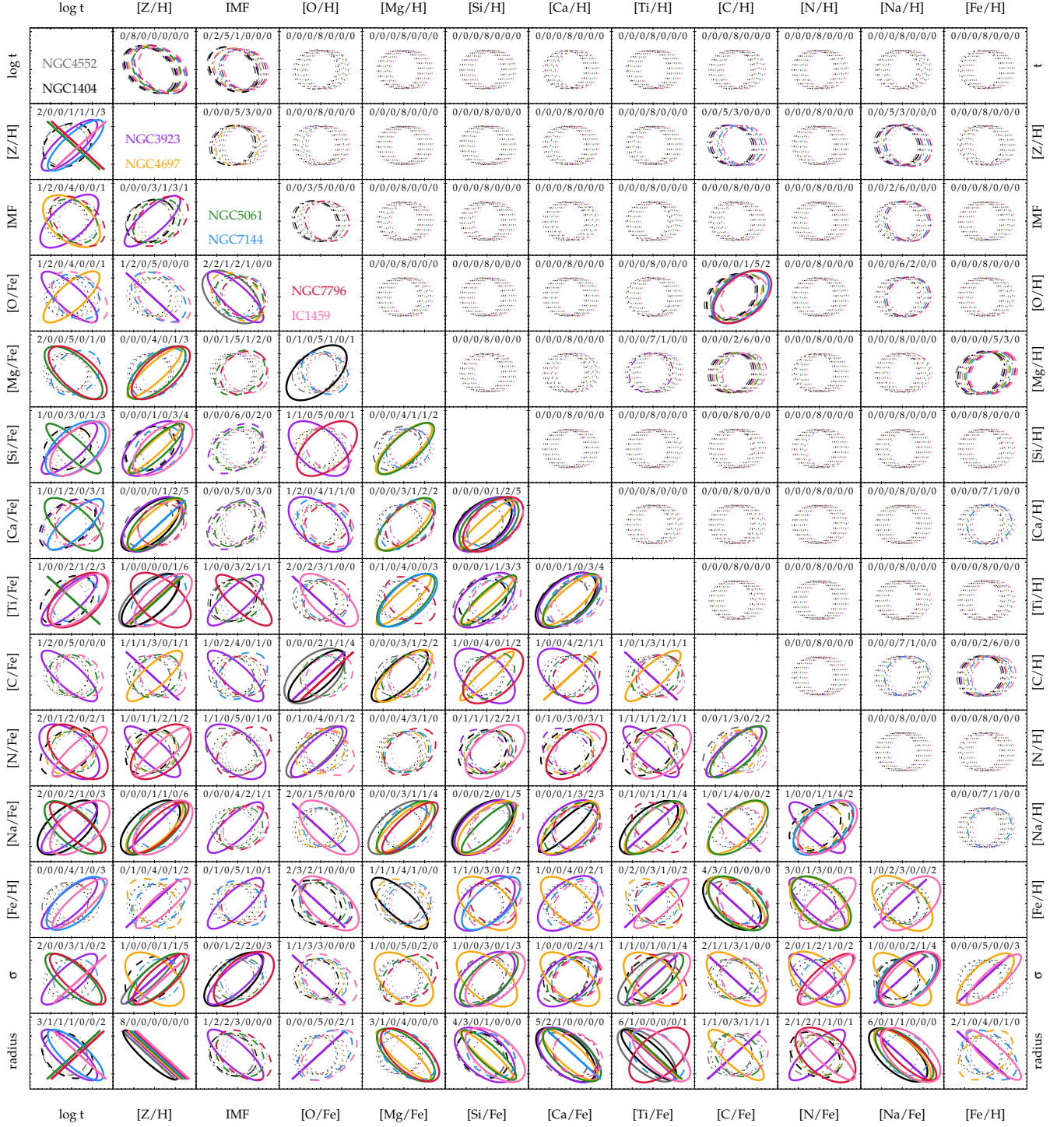


Figure 8. Same as Figure 7, but excluding NGC 5061.



**Figure 9.** Correlation matrix. Upper-right off-diagonal displays the mean covariances per galaxy of fitting parameter PDFs obtained in the PYSTAFF fit; Lower left off-diagonal the correlations of local values of Stellar Population Parameters for each individual galaxy. Different colors denote different galaxies as in Figure 1, solid thick lines very high correlations ( $|\rho| \geq 0.8$ ), dashed lines high ( $0.6 \leq |\rho| < 0.8$ ), dot-dashed lines moderate ( $0.4 \leq |\rho| < 0.6$ ), dotted lines no or weak correlations ( $|\rho| < 0.4$ ). In each panel we note the number of galaxies with  $\rho \leq -0.8$ / $-0.8 < \rho \leq -0.6$ / $-0.6 < \rho \leq -0.4$ / $-0.4 < \rho < 0.4$ / $0.4 \leq \rho < 0.6$ / $0.6 \leq \rho < 0.8$ / $\rho \geq 0.8$ . Each ellipse is slightly offset to the right to make them easier visible.

**Table 4.** Number of Galaxies with high Spearman Rank Correlation  $\rho$  for Local Stellar Population Parameters, excluding the central data points. We list only cases with at least five high correlations ( $|\rho| \geq 0.6$ )

Parameter	Parameter	sign	Number of galaxies with	
			$ \rho  \geq 0.8$	$0.6 \leq  \rho  < 0.8$
$r/R_e$	[Z/H]	neg.	8	0
$r/R_e$	[Si/Fe]	neg.	4	3
$r/R_e$	[Ca/Fe]	neg.	5	2
$r/R_e$	[Ti/Fe]	neg.	6	1
$r/R_e$	[Na/Fe]	neg.	6	0
$\sigma$	[Z/H]	pos.	5	1
$\sigma$	[Ca/Fe]	pos.	1	4
$\sigma$	[Ti/Fe]	pos.	4	1
$\sigma$	[Na/Fe]	pos.	4	1
$\log(t)$	[Ti/Fe]	pos.	3	2
[Z/H]	[Si/Fe]	pos.	4	3
[Z/H]	[Ca/Fe]	pos.	5	2
[Z/H]	[Ti/Fe]	pos.	6	1
[Z/H]	[Na/Fe]	pos.	6	0
[Fe/H]	[O/Fe]	neg.	2	3
[Fe/H]	[C/Fe]	neg.	4	3
[O/Fe]	[C/Fe] <sup>a</sup>	pos.	4	1
[Mg/Fe]	[Na/Fe]	pos.	4	1
[Si/Fe]	[Ca/Fe]	pos.	5	2
[Si/Fe]	[Ti/Fe]	pos.	3	3
[Si/Fe]	[Na/Fe]	pos.	5	1
[Ca/Fe]	[Ti/Fe]	pos.	4	3
[Ca/Fe]	[Na/Fe]	pos.	3	2
[Ti/Fe]	[Na/Fe]	pos.	4	1
[N/Fe]	[Na/Fe]	pos.	2	4

NOTE—a: Some of the Parameter PDFs are correlated.

confirming our radial gradient measurements in Section 3.1.2. Several  $\nabla_r$  are negative for [Z/H], [Si/Fe], [Ca/Fe], [Ti/Fe], and [Na/Fe], whereas e.g. the IMF slope, [N/Fe], or [O/Fe] have a non-monotonic radial behavior for some galaxies, leading to weaker correlations.

The correlations with  $\sigma$  (second row from bottom in Figure 9) are mostly positive, but this may be simply caused by the radially decreasing  $\sigma$  profile of most of our galaxies (see Figure 2). NGC 4697 (shown in yellow), a galaxy with a radially slightly increasing  $\sigma$ , has several very high negative correlations of stellar population parameters with  $\sigma$ , while the other galaxies have positive correlations. Also [Barbosa et al. \(2021b\)](#) found that the positive IMF- $\sigma$  relation does not hold for a galaxy with

radially increasing  $\sigma$ . We found that this is also the case for other stellar population parameters.

The positive correlations of several elemental abundances with [Z/H] (second column in Figure 9) are expected, as increased elemental abundances contribute to the overall [Z/H] of a galaxy. There is also a positive correlation of [Z/H] with the IMF slope for four galaxies. [Barbosa et al. \(2021b\)](#) suggest that such correlations may be connected to the positive covariance of IMF and [Z/H], however, in our spectral fitting the covariances are on average only weak to moderate ( $0.14 < \rho < 0.46$ ). Also correlations of O and C (5 galaxies), IMF slope and O, Mg and C (4 galaxies each) may be to some extent connected to the covariances of these parameters in the PDFs of the spectral fits, though these tend to be weaker than our local correlations (see upper right off-diagonal in Figure 9). We note that Fe and C in our fits have a positive covariance, so the negative local correlation found for seven galaxies cannot be due to a covariance of the parameters' PDFs.

Elements that are mostly produced in massive stars (e.g. Mg, Si, Ca, Ti) correlate with each other and with Na in several galaxies. Sodium also correlates with nitrogen, which is produced in intermediate-mass stars. This suggests that sodium is produced partially in high-mass, but also in intermediate-mass stars. On the other hand, correlations of nitrogen with other elements produced dominantly in high-mass stars tend to be weaker. This may indicate a non-uniform IMF slope shape at the high-mass end (i.e.  $>3 M_\odot$ ) as a function of galaxy radius. But it may also be caused by [Z/H]-dependent nitrogen yields (see Section 6). We discuss the ratios of different elemental abundances and clues on the element production in Section 5.

We found no strong local correlation with the low-mass IMF slope that holds for more than four galaxies. The strongest cases are a negative correlation of IMF slope with O, and a positive correlation with [Z/H] for four galaxies each. In both cases, the PDFs of these parameters have covariances in the same direction in some of our fits, though on average the covariances are only weak to moderate. [Barbosa et al. \(2021b\)](#) suggest that the IMF-[Z/H] correlation may be, at least partially, caused by a covariance of these parameters in stellar population fits. This correlation holds locally only for some of our galaxies, but is very high globally ( $\rho \geq 0.79$ , Figure 5). This suggests that the global correlation is not entirely caused by unresolved degeneracies in our fits, and these parameters may indeed correlate, though it is not clear if there is a causal relation.



## 5. RELATIVE ELEMENTAL ABUNDANCES AND ELEMENT PRODUCTION

Here we compare abundances of different elements, and how they may depend on  $[Z/H]$ . With a focus on oxygen, carbon, nitrogen, and sodium, we discuss some possible implication on the production of these elements.

We found that  $\alpha$  element abundances differ from element to element, as can be seen in Figure 10, where we show the elemental abundances as a function of atomic number of X, different panels denote different radial ranges. Overall, lower mass elements tend to have higher abundances, i.e.  $[O/Fe] > [Mg/Fe] > [Si/Fe] > [Ca/Fe]$ , though this does not always hold for  $[Ti/Fe]$ .

Oxygen is the most abundant element in the Universe (with the exception of hydrogen and helium, and followed by carbon and nitrogen), and thought to dominate  $[Z/H]$ . However, the measurement of oxygen is more complicated than e.g. Mg, as oxygen only appears in molecular transitions in combination with Ti in our spectra. Oxygen is also crucial to estimate C and N, as those exist in CO, CN, and C<sub>2</sub> molecules. Oxygen is to some extent also formed in intermediate-mass stars ( $\sim 10\%$ , Maiolino & Mannucci 2019). Therefore, it may not be surprising that O does deviate from  $\alpha$  elements such as Mg, meaning  $[\alpha/O] \neq 0$ . Though, we find deviations as large as  $[Mg/O] = -0.3$  dex (see Figure 11). Values ranging from  $-0.3$  to  $+0.6$  were also found in Milky Way bulge stars (McWilliam et al. 2008). Moreover, we found that the ratio of  $[X/O]$  seems to correlate with  $[Z/H]$  for several galaxies (see Figure 11). The general trends are similar for most  $[\alpha/O]$  and  $[C/O]$ , probably since  $\alpha$  elements and  $\sim 70\%$  of carbon are produced in massive stars (Romano et al. 2020).  $[X/O]$  is increasing with  $[Z/H]$  at  $[Z/H] < 0$ , then there is a flattening and sometimes a turnover towards higher  $[Z/H]$ , with decreasing  $[X/O]$  for higher  $[Z/H]$ . A possible explanation are lower oxygen yields at increasing  $[Z/H]$ , caused by higher mass loss (Maeder 1992; Meynet & Maeder 2002). At super-solar  $[Z/H]$  and in very massive stars, carbon yields decrease even more than oxygen yields, causing the turnover of  $[C/O]$  (Portinari et al. 1998).

Nitrogen is thought to be primarily produced by intermediate-mass stars ( $4-8 M_{\odot}$ ), with a small contribution of massive stars, that is more important at low  $[Z/H]$ . We find that  $[N/O]$  increases with  $[Z/H]$  for several galaxies, especially at  $[Z/H] \gtrsim -0.2$  dex. This may be since nitrogen is produced as secondary element, from intermediate-mass stars that formed from gas that was already enriched with C and O (Maiolino & Mannucci 2019). At lower  $[Z/H]$ , studies of nitrogen and oxygen in the gas phase found a flattening of  $[N/O]$ , which is attributed to the primary contribution from massive stars

(Maiolino & Mannucci 2019).  $[Z/H]$ -dependent yields may also cause the weak local correlations of  $\alpha$  elements to N, found in Section 4.3. Similar to studies of  $N/O$  in the gas phase, we see indications of a flattening of  $[N/O]$  in individual galaxies at the outer radii, where  $[Z/H]$  decreases. However, we caution that our nitrogen measurements at large radii have large uncertainties, exceeding 0.1 dex.

Most galaxies have increasing  $[Na/O]$  with  $[Z/H]$  over the entire range. The correlation of  $[Na/O]$  with  $[Z/H]$  is even higher than of  $[Na/Fe]$  with  $[Z/H]$  (Section 4.3), with a high Spearman rank correlation coefficient  $\rho > 0.65$  for all galaxies. The behavior of  $[Na/Fe]$  in the Milky Way bulge indicates that Na may be produced in massive stars, and Na yields increase with  $[Fe/H]$  (McWilliam 2016). This may explain why there is no flattening of  $[Na/O]$  with  $[Z/H]$ , as we see for other  $[X/O]$  ratios. N has only few high local correlations with other elements, with the exception of Na. Six galaxies have high local correlations of Na and N, which is mainly produced in intermediate-mass stars. This may suggest that Na is, to a larger extent than  $\alpha$  elements, formed in intermediate-mass stars.

To summarise, different  $[X/O]$  ratios show different behaviors with  $[Z/H]$  at the high- and low- $[Z/H]$  end. Most  $\alpha$  elements behave in a similar way. Oxygen and carbon production appear to be suppressed at high  $[Z/H]$ , but this is not the case for sodium.

## 6. DISCUSSION

### 6.1. Limitations of our Stellar Population Measurements

One caveat in our study is that we assumed a single stellar population, although we see signs of mixed stellar populations at larger radii (Appendix D.1). These outer stars were possibly brought in from minor mergers, or formed later in a star formation event triggered by a galaxy merger, as part of the second stage of galaxy assembly. Neglecting the star formation history may bias our SSP parameters at larger radii. For example, the light-weighted age is biased to lower values. For NGC 5061, this bias seems to exist even over the entire galaxy, not just in the outer region. Including a second stellar population in the fit, as done by van Dokkum et al. (2017), is probably a better approximation, and we are planning to implement this in the future. Although the assumption of a SSP is an oversimplification, we found that most of our galaxies are dominated by an old, metal-rich stellar population, at least in the inner regions (Appendix D.1), and we can still study differences among the galaxies in our sample.

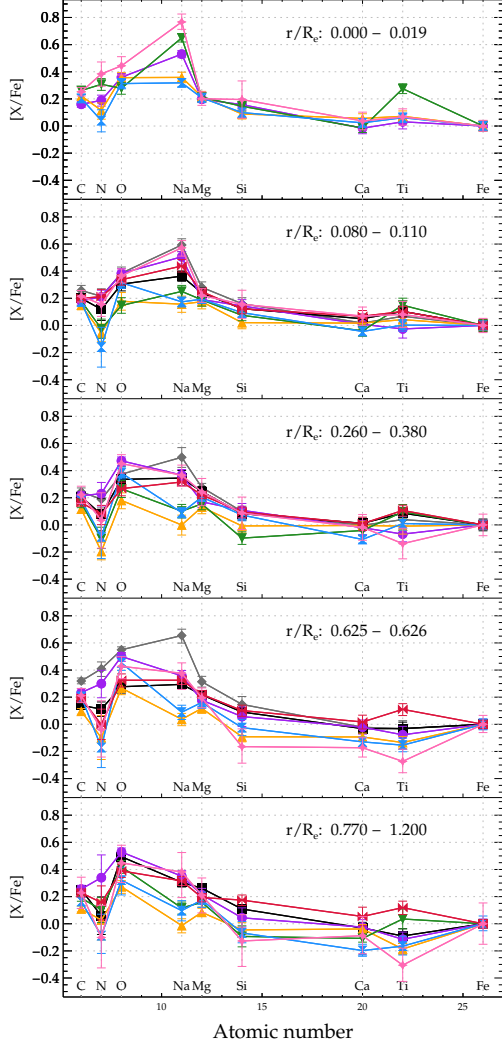


**Figure 10.** Elemental abundances  $[X/Fe]$  as function of atomic number for five different radial bins ( $0-0.019 R_e$ ,  $0.08-0.11 R_e$ ,  $0.26-0.38 R_e$ ,  $0.625-0.626 R_e$ , and  $0.77-1.2 R_e$ ). Different colors and symbols denote different galaxies, as in previous Figures.

The SSP model spectra themselves are based on various assumptions: They are built from atomic and molecular line lists, which may be incomplete, and model atmospheres that assume local thermodynamic equilibrium (LTE). However, we see no systematic residuals in our fits that would indicate a missing line, and the relative error introduced by the LTE assumption is negligible ( $\ll 1\%$ ), except for the Ca H&K region (Conroy et al. 2018), which we did not include in the fits.

In addition, our fitting method has certain restrictions: The elemental abundance measurements are obtained by applying linear multiplicative response functions for each individual element (Vaughan et al.

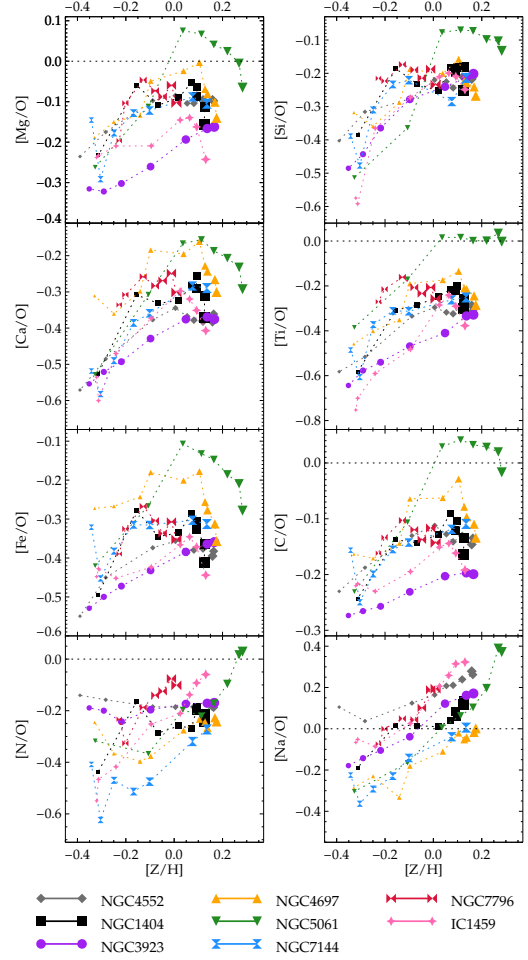


**Figure 11.** Elemental abundances  $[X/O]$  as function of total metallicity  $[Z/H]$  for eight galaxies, denoted by different colors and symbols. Decreasing symbol sizes denote increasing galaxy radius.

2018a,b). The response functions of the Conroy et al. (2018) models are computed at reference values. In some of our fits, the resulting elemental abundances of  $[C/H]$  and  $[O/H]$  exceed the reference value, meaning our results are an extrapolation. The fitting code PYSTAFF applies a Taylor expansion near the reference value. Compared to a linear extrapolation, our results for  $[O/H]$  that exceed the reference values of 0.3 dex are biased to lower values. The bias increases with increasing values of  $[O/H]$ , reaching up to 0.1 dex. The bias in  $[C/H]$  for values beyond the reference values of 0.15 dex is smaller,  $<0.05$  dex (see Appendix C.2). For other elements (Mg, Si, Ca, Ti, N, Na, Fe), our results are mostly within the reference values of the response functions, and for this reason unaffected by problems related to extrapolation.

### 6.2. Variations of the IMF

We measured the low-mass IMF slope ( $0.08\text{-}1 M_{\odot}$ ) and found some indications for global correlations, but few local correlations.

Several studies have suggested a local correlation of the IMF with other SP parameters, but we can confirm these correlations only for subsets of our sample. For example, Parikh et al. (2018) used stacked galaxy spectra and found local high positive correlations of the IMF slope with  $[Z/H]$ ,  $[Na/Fe]$ ,  $\sigma$ ,  $r/R_e$ , and age, while we obtain these correlations for no more than four galaxies in our sample. Why do we find these correlations only for some galaxies? Concerning the IMF- $[Z/H]$  correlation, Barbosa et al. (2021b) suggest that it is, at least partially, due to a degeneracy of these parameters in spectral fits. We also see a correlation of these parameters in the PDFs of some, but not all spectral fits. Thus, the strength of this correlation may be overestimated in other studies. The IMF- $[Na/Fe]$  correlation of Parikh et al. (2018) may be a consequence of local  $[Z/H]$ - $[Na/Fe]$  correlations (Table 4); thus, breaking the IMF- $[Z/H]$  degeneracy in our fits means we will not detect an IMF- $[Na/Fe]$  correlation. Some galaxies in our sample have a relatively flat IMF profile, and hence no correlation with  $r/R_e$ . Lastly, the IMF- $\sigma$  correlation does not hold for galaxies with a radially increasing  $\sigma$  (Barbosa et al. 2021b); hence there is no simple causal relation of IMF and  $\sigma$ .

The lack of correlations between the IMF slope and elemental abundances may not be surprising. We measured the low-mass end of the IMF slope ( $<1 M_{\odot}$ ), whereas the elements were mostly produced in more massive stars ( $>3 M_{\odot}$ ). The IMF may be more complicated than a single slope at  $<1 M_{\odot}$  and the Salpeter slope at  $>1 M_{\odot}$ , and require a non-parametric description (Conroy et al. 2017) over the entire stellar mass range. We may even see a variation of the IMF in the intermediate-mass range in our Na and N abundances: At a given value of  $[Z/H]$ ,  $[Na/Fe]$  and  $[N/Fe]$  vary by roughly 0.3–0.4 dex from galaxy to galaxy, while various  $\alpha/Fe$  have a range of only  $\sim 0.15$  dex. Also  $[C/Fe]$  varies by about 0.15 dex, but the upper end of our  $[C/Fe]$  range may be biased to lower values by  $\lesssim 0.05$  dex (Appendix C.2). One possible explanation is that the IMF slope in the intermediate-mass range ( $3\text{-}8 M_{\odot}$ ), where most of N and some Na and C are produced, varies among individual galaxies.

Instead of local, we see some global IMF correlations: Galaxies with higher central  $[Z/H]$  tend to have a higher central IMF slope, steeper than Salpeter, but becoming more Salpeter-like with increasing radius (see Section 4.2). Galaxies with lower central  $[Z/H]$  tend to have

a radially flat, and Salpeter-to sub-Salpeter IMF slope. Whether there is causal relation for the correlation of central  $[Z/H]$  and IMF slope is unclear. At  $r > 0.5 R_e$  the variation of possible IMF slopes is comparable to the measurement uncertainties, and therefore consistent with no IMF variations.

### 6.3. Global $\sigma$ Correlations and Possible Influence of Galaxy Properties

Several studies have found global correlations of galaxy properties such as  $\sigma_{R_e/8}$  with stellar populations parameters  $t$ ,  $[Z/H]$ , and elemental abundances (for a review see Maiolino & Mannucci 2019). These relations are fundamental to our understanding of galaxy formation and evolution, and an important test bench for galaxy evolution models.

We found some strong correlations with  $\sigma_{R_e/8}$  for our sample of seven galaxies that are known in the literature, while some literature correlations are only weak. However, the galaxies are non-uniform concerning their star formation activity, AGN activity, and environment. Could these influence and weaken our SP- $\sigma$  correlations? Thomas et al. (2010) showed that star formation activity influences the SP- $\sigma$  relationships. For this reason, we excluded NGC 5061 from our correlation analysis. Most galaxies in our sample are passive, though IC 1459 is a LINER. Graves et al. (2007) found that LINER galaxies follow similar  $\sigma$  correlations for  $[Z/H]$  and abundances as passive galaxies, which led us to include IC 1459. The galaxies in our sample are located in different environments (isolated, galaxy groups, and clusters). Thomas et al. (2010) found that the correlations of the global galaxy age (considering only old galaxies),  $[Z/H]$ , and  $[\alpha/Fe]$  with  $\sigma$  are not affected. On the other hand, Ferreras et al. (2019), who measured radial stellar population gradients, found some variations between cluster and field/group environments, but only at a  $1\text{-}2\sigma$  level. We found that the isolated galaxy NGC 7796 has overall flatter radial gradients and lower  $[Z/H]$ . The flatter gradients may be caused by lower galaxy minor merger rates in low-density environments (Lin et al. 2010), but it is not clear if the lower  $[Z/H]$  in the center of NGC 7796 compared to other galaxies with similar  $\sigma_{R_e/8}$  in our sample is related to the environment.

The weaker global correlation of e.g.  $[Z/H]$  and  $[Mg/Fe]$  to  $\sigma_{R_e/8}$  in our study compared to the literature may simply be caused by intrinsic scatter among the galaxies in our study. We summarise the properties of the individual galaxies in Appendix E. We found that variations between the individual galaxies of our small sample exceed global correlations. Also, elemental abundances cover a wider range with increasing radius com-

pared to the center, as some galaxies have steep, others have shallow elemental abundance gradients. This emphasises the complexity of possible evolutionary paths of different early-type galaxies.

## 7. SUMMARY

In this paper we analyzed long-slit spectroscopic data in the wavelength range 4000-8600 Å for eight early-type galaxies (NGC 1404, NGC 3923, NGC 4552, NGC 4697, NGC 5061, NGC 7144, NGC 7796, IC 1459). We used full spectral fitting and the single stellar population (SSP) models of Conroy et al. (2018) to measure the following SSP parameters: age  $t$ , metallicity  $[Z/H]$ , low-mass IMF slope in the mass range  $0.08-1 M_{\odot}$ , and the elemental abundances  $[O/Fe]$ ,  $[Mg/Fe]$ ,  $[Si/Fe]$ ,  $[Ca/Fe]$ ,  $[Ti/Fe]$ ,  $[C/Fe]$ ,  $[N/Fe]$ ,  $[Na/Fe]$ ,  $[Fe/H]$ . Our measurements as a function of radius extend to  $\sim 1 R_e$ , and we fit radial gradients  $\nabla_r$  of each stellar population parameter as a function of  $\log(r/R_e)$ . We found a wide range of properties, with ages ranging from 3-13 Gyr. All galaxies have radially decreasing  $[Z/H]$ . Some galaxies have a radially constant, Salpeter-like IMF, and other galaxies have a super-Salpeter IMF in the center, decreasing to sub-Salpeter IMF at  $\sim 0.5 R_e$ .

To understand how various SSP parameters depend on each other, we calculated the Spearman rank correlation coefficient  $\rho$  of various parameters. Our data set allows us to test whether there are both global and local correlations of stellar population parameters with each other, or other galaxy properties.

We found high global correlations among central stellar population parameters (e.g.  $[Z/H]$  correlates with the IMF slope;  $[Si/Fe]$  with  $[Na/Fe]$ ), radial gradients (e.g.  $\nabla_r[Fe/H]$  anti-correlates with  $\nabla_r[C/Fe]$ ;  $\nabla_r[N/Fe]$  correlates with  $\nabla_r[Na/Fe]$ ), and of central values with gradients (e.g.  $[Z/H]$  anti-correlates with both  $\nabla_r[Z/H]$  and  $\nabla_r$ IMF). Some correlations may, to some extent, be strengthened by covariances of the SP parameters in our spectral fitting. We also calculated the Spearman rank coefficient,  $\rho$ , of our SSP parameters at  $0.1 R_e$  with the central stellar velocity dispersion  $\sigma_{R_e/8}$  for seven galaxies (excluding NGC 5061, which may have biased SSP parameters), and performed a linear fit.  $\sigma_{R_e/8}$  is a proxy for the galaxy’s central gravitational potential. Several of our linear relations are in good agreement with relations from the literature, though some parameters have a large scatter and hence only weak to moderate correlations. Our sample size is small (seven galaxies when excluding NGC 5061); therefore, our global correlations require confirmation with a larger number of galaxies.

We tested if there are local correlations for each individual galaxy. The most common is a very strong anti-

correlation of  $[Z/H]$  with the galaxy’s radius (i.e. negative  $\nabla_r[Z/H]$ ); it holds for all galaxies. Further, there are strong positive correlations (i) of  $[Z/H]$  and some elemental abundances (Ca, Ti, Na) with local  $\sigma$  for at least five galaxies, (ii) of  $[Z/H]$  with several elemental abundances (e.g. Ca, Si, Ti, Na), and (iii) of several elemental abundances with each other (e.g. Ca with Si, Ti, Na). Correlations of various elemental abundances can be expected if they are produced by the same process, e.g.  $\alpha$  elements produced in explosions of massive stars. We caution that in a few cases (e.g. O with C), the parameters also have correlated probability distribution functions, which may to some extent cause the high local correlations. While these correlations are interesting, they do not necessarily indicate a causal relation of parameters.

## ACKNOWLEDGMENTS

We would like to thank Barry Madore and the Las Campanas staff who helped us to obtain the data, Sam Vaughan for sharing the code PYSTAFF, and Charlie Conroy for sharing the SSP models. We also thank the referee for very constructive comments and suggestions. We acknowledge the usage of the HyperLeda database (<http://leda.univ-lyon1.fr>, Makarov et al. 2014). This paper includes data gathered with the 6.5 meter Magellan Telescopes located at Las Campanas Observatory, Chile. This research has made use of the NASA/IPAC Extragalactic Database (NED) which is operated by the Jet Propulsion Laboratory, California Institute of Technology, under contract with the National Aeronautics and Space Administration. This research has made use of the SIMBAD database, operated at CDS, Strasbourg, France. This research has made use of NASA’s Astrophysics Data System Bibliographic Services. This research made use of ds9, a tool for data visualization supported by the Chandra X-ray Science Center (CXC) and the High Energy Astrophysics Science Archive Center (HEASARC) with support from the JWST Mission office at the Space Telescope Science Institute for 3D visualization.

*Facilities:* Magellan (IMACS)

*Software:* EMCEE (Foreman-Mackey et al. 2013), L.A.Cosmic (van Dokkum et al. 2012), MOLECFIT (Kausch et al. 2015; Smette et al. 2015), pPXF (Cappellari 2017), PYSTAFF (Vaughan et al. 2018b), Matplotlib (Hunter 2007), NumPy (van der Walt et al. 2011), IRAF (Tody 1986, 1993), corner (Foreman-Mackey 2016)

## APPENDIX

## A. CORRECTION FOR GALAXY ROTATION

Several galaxies of our sample have rotational velocities of  $\sim 100 \text{ km s}^{-1}$  or varying rotation profiles (Franx et al. 1989; Dejonghe et al. 1996; Koprolin & Zeilinger 2000; Emsellem et al. 2004), which we accounted for in the following ways: for NGC 1404, NGC 4697, NGC 5061, and NGC 4552 we extracted spectra on both sides of the slit separately, measured the radial velocity shift with pPXF (Cappellari 2017), and corrected the radial velocities before summing the two spectra with the same distance to the galaxy center and from the two sides of the slit. In this step we also fit Balmer gas emission flux and subtracted it. We used a different approach for IC 1459, which has a counter-rotating stellar core. This galaxy has strong gas emission lines, but the gas emission does not co-rotate with the stars and is asymmetric about the nucleus (Cappellari et al. 2002). We separately extracted and analyzed the northern and southern spectra out to  $0.5 R_e$ , to improve the emission line subtraction. For the outer radii  $>0.5 R_e$ , we combined the two regions, to ensure sufficiently high S/N. The central rotation is  $\sim 100 \text{ km s}^{-1}$ . The rotation sense changes between  $0.1$  and  $0.19 R_e$ , and at  $0.375 R_e$ , the rotation is  $\sim 60 \text{ km s}^{-1}$ . Ignoring the rotation in the outer radial bins means that we will overestimate the velocity dispersion, as we actually measure the root-mean-square velocity,  $V_{\text{rms}} = \sqrt{V^2 + \sigma^2}$ . This has only a minor effect on  $\sigma$  ( $\sim 5 \text{ km s}^{-1}$ ), but we later correct for the rotation assuming a constant rotation velocity of  $50 \text{ km s}^{-1}$  at  $r > 0.5 R_e$  (Franx & Illingworth 1988).

For the remaining galaxies (NGC 7144, NGC 7796, NGC 3923) we did not correct the stellar rotation of the spectra. We tested if this is acceptable by extracting spectra on both the northern and southern side of the slit and cross-correlating them. We obtained only small shifts, usually  $\lesssim 0.5$  pixel; that is,  $< 10 \text{ km s}^{-1}$  for NGC 7144 (see Franx et al. 1989 for rotation curve), NGC 7796 (see Bertin et al. 1994), and NGC 3923 at our PA of observations. This means that, technically, for these galaxies our measurement of  $\sigma$  is actually the root-mean-square velocity,  $V_{\text{rms}}$ . The rotation velocity of these galaxies is comparably low and the profiles rather flat, and we simply correct  $V_{\text{rms}}$  to  $\sigma$  by subtracting in quadrature the literature values for the rotation at the axis closest to our observations; that is  $40 \text{ km s}^{-1}$  for NGC 7144 (Franx et al. 1989; Saglia et al. 1993),  $30 \text{ km s}^{-1}$  for NGC 7796 (Bertin et al. 1994), and  $\sim 0 \text{ km s}^{-1}$  for NGC 3923 (Carter et al. 1988).

To summarise, we corrected the galaxy rotation where necessary. We neglected rotation for galaxies with low and constant rotation velocity, allowing us to increase the S/N of the spectra.

## B. DATA QUALITY

To estimate the S/N of our data, we used DER\_SNR (Stoehr et al. 2007), on 100 pixel wide segments of unconvolved and rebinned spectra, with steps of 50 pixels. DER\_SNR is a robust algorithm that uses only the spectrum flux, and assumes that the noise is normally distributed and uncorrelated two pixels apart. While this assumption may not be strictly true for our rebinned spectra (see Section 2.2), we can still learn how the S/N varies from galaxy to galaxy, for different radius bins for a single galaxy, and as a function of wavelength. We show the S/N in Figure 12.

For all galaxies, we find an increase of S/N with wavelength from  $< 4000 \text{ \AA}$  to  $\sim 6000 \text{ \AA}$ , in some cases followed by a decrease to  $7000 \text{ \AA}$ . The CaT region has usually similar or lower values of S/N, due to the lower exposure times, with the exception of IC 1459 with PA= $0^\circ$ . All galaxies have similar S/N, usually in the range of 50 to  $300/\text{\AA}$ .

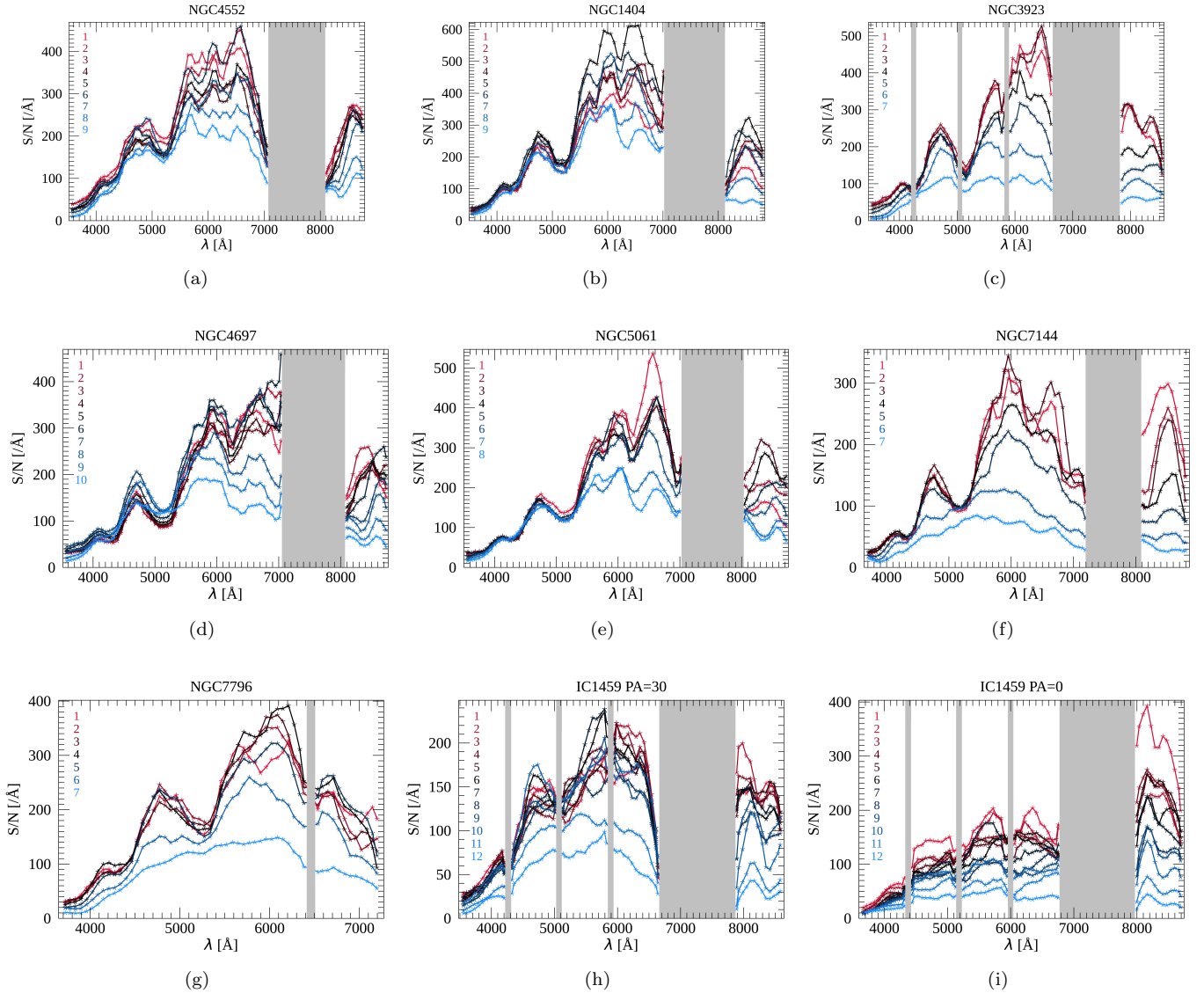
## C. SINGLE STELLAR POPULATION (SSP) FITTING

C.1. *Treatment of Gas Emission Lines and Systematic Uncertainties*

All SSP PYSTAFF fits included Balmer gas emission lines. We tied the individual Balmer lines to the same kinematics and fixed the relative fluxes of the Balmer lines ( $H\delta=0.259 H\beta$ ,  $H\gamma=0.468 H\beta$ ,  $H\alpha=2.86 H\beta$ , Osterbrock 1989; Reynolds et al. 1997). We constrained the gas kinematics to be close to the stellar kinemat-

ics ( $\pm 30 \text{ km s}^{-1}$ )<sup>4</sup>, to ensure that we obtain a reasonable emission line flux estimate. An overestimation of the Balmer emission line flux biases our age result to younger ages, and an underestimated gas emission to older ages.

<sup>4</sup> The exception is IC 1459, as the gas and stellar kinematics are decoupled for this galaxy (Cappellari et al. 2002).

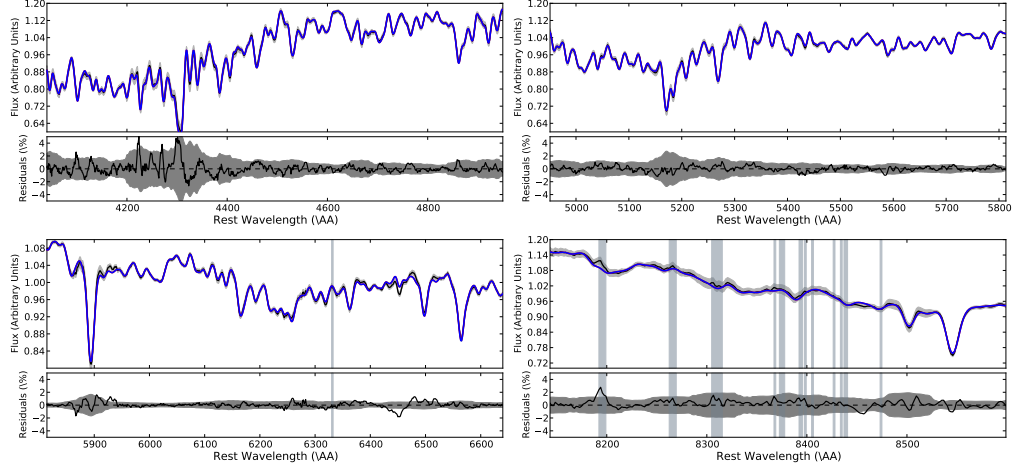
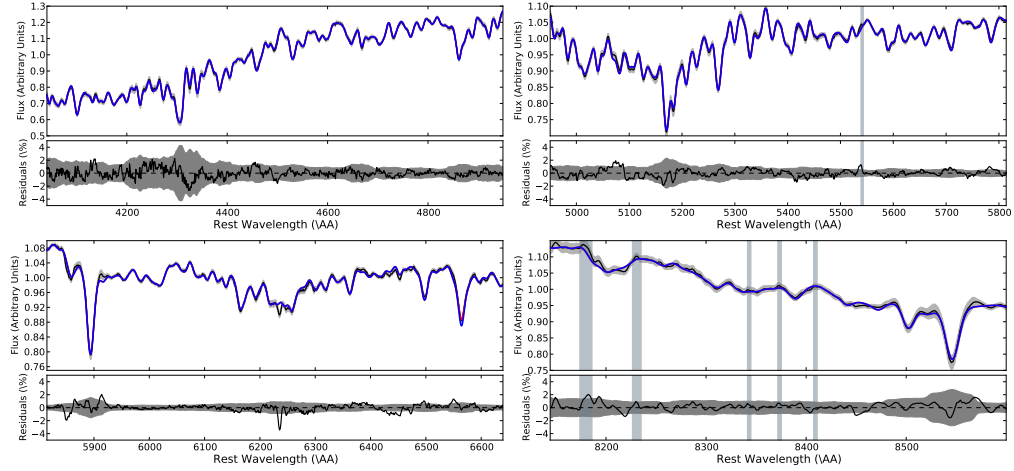
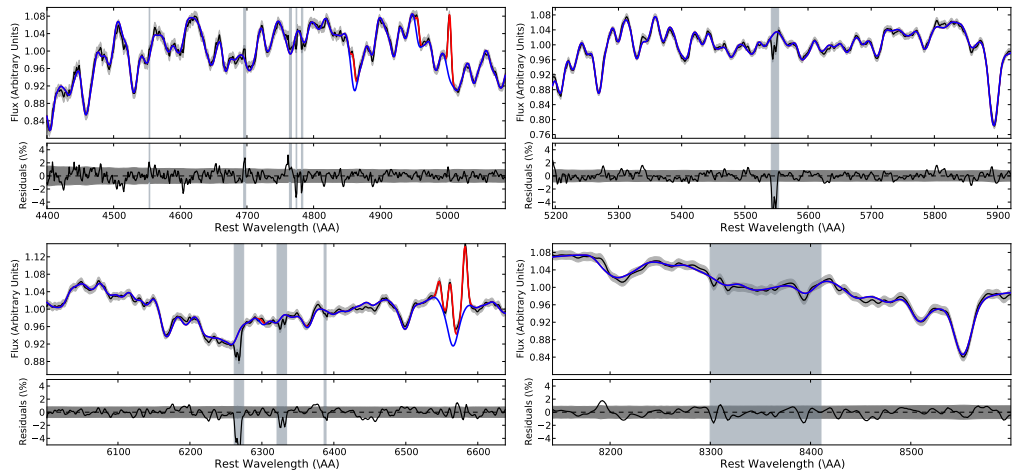


**Figure 12.** Signal-to-noise ratio as function of wavelength for each galaxy. The different colors denote central spectra (red) to spectra at large radii (blue). Note the different ranges of the wavelength and S/N axes for different galaxies. Spectral regions without coverage are shown as gray shaded regions.

For IC 1459 it was necessary to fit further emission line flux doublets: [N II] ( $[\text{N II}]_{\lambda 6548.03} = 0.33 [\text{N II}]_{\lambda 6583.41}$ ), [O III] ( $[\text{O III}]_{\lambda 4958.92} = 0.33 [\text{O III}]_{\lambda 5006.84}$ ), [O I] ( $[\text{O I}]_{\lambda 6363.67} = 0.33 [\text{O I}]_{\lambda 6300.30}$ ), and [N I] ( $[\text{N I}]_{\lambda 5200.39} = 0.7 [\text{N I}]_{\lambda 5197.90}$ ). We fit the Balmer gas kinematics separately from the other emission line doublets. The results between the kinematics of Balmer and the other emission lines differ by usually no more than  $\sim 50 \text{ km s}^{-1}$ . We show three examples of the data and best-fit model spectra in Figure 13. The gas emission is prominent in the spectrum of IC 1459 (bottom panel).

We fit each spectrum using two different wavelength regions, as listed in Table 5. The wavelength ranges are split into four sections, and in each section we

fit a Legendre polynomial to correct the continuum shape. The polynomial order is the nearest integer to  $(\lambda_{\text{upper}} - \lambda_{\text{lower}})/100$ . We also list the emission lines that were included for each fit. In most cases, we have one set of fits with two Balmer lines,  $\text{H}\gamma$  and  $\text{H}\beta$ , and a second set with longer wavelengths, that includes in addition  $\text{H}\delta$  and  $\text{H}\alpha$ . Usually the results from the two fits are in agreement within  $1\sigma$ . However, due to the different wavelength regions and Balmer lines, there can be differences in the results for the Balmer line flux, and as a consequence, the stellar population age  $t$ . We find that the shorter wavelength fits result in a larger gradient of the Balmer line flux and  $t$  compared to the longer wavelength fits that include  $\text{H}\delta$  and  $\text{H}\alpha$ . For each


 (a) PySTAFF fit of NGC 4697,  $r=0.15 R_e$ 

 (b) PySTAFF fit of NGC 5061,  $r=0.13 R_e$ 

 (c) PySTAFF fit of IC 1459,  $r=0.1875 R_e$  south

**Figure 13.** Examples of spectra (black), the PySTAFF best-fit stellar population models (blue), and gas emission (red). The gray color along the spectrum illustrates the noise level; vertical grey regions are excluded from the fit due to bad pixels, sky, telluric, or fringe residuals. The plots also show the fit residuals in percent as a function of wavelength. The examples are NGC 4697 at  $r=0.15 R_e$ , NGC 5061 at  $r=0.13 R_e$ , and IC 1459 at  $r=0.1875 R_e$  south and PA=0.

**Table 5.** Summary of PYSTAFF Fit Settings

Galaxy	Approximate Rest-wavelength Fitting Range (Å)	Emission Lines
NGC 4552	4230–4950, 4950–5814, 5814–6455, 8143–8600	H $\gamma$ , H $\beta$
(M 89)	4040–4950, 4950–5814, 5814–6640, 8143–8600	H $\delta$ , H $\gamma$ , H $\beta$ , H $\alpha$
NGC 1404	4230–4950, 4950–5814, 5814–6455, 8143–8600	H $\gamma$ , H $\beta$
	4040–4950, 4950–5814, 5814–6640, 8143–8600	H $\delta$ , H $\gamma$ , H $\beta$ , H $\alpha$
NGC 3923 <sup>b,d</sup>	4285–4893, 5144–5813, 5885–6417, 8164–8524	H $\gamma$ , H $\beta$
	4040–5030, 5090–5814, 5885–6640, 8143–8524	H $\delta$ , H $\gamma$ , H $\beta$ , H $\alpha$
NGC 4697	4230–4950, 4950–5814, 5814–6455, 8143–8600	H $\gamma$ , H $\beta$
	4040–4950, 4950–5814, 5814–6640, 8143–8600	H $\delta$ , H $\gamma$ , H $\beta$ , H $\alpha$
NGC 5061	4230–4950, 4950–5814, 5814–6455, 8143–8600	H $\gamma$ , H $\beta$
	4040–4950, 4950–5814, 5814–6640, 8143–8600	H $\delta$ , H $\gamma$ , H $\beta$ , H $\alpha$
NGC 7144	4230–4950, 4950–5814, 5814–6455, 8143–8600	H $\gamma$ , H $\beta$
	4040–4950, 4950–5814, 5814–6640, 8143–8600	H $\delta$ , H $\gamma$ , H $\beta$ , H $\alpha$
NGC 7796 <sup>a</sup>	4230–4685, 4685–5238, 5238–5802, 5802–6455	H $\gamma$ , H $\beta$
	4040–4685, 4685–5238, 5238–5802, 5802–6640	H $\delta$ , H $\gamma$ , H $\beta$ , H $\alpha$
IC 1459 (PA=0°) <sup>c,d</sup>	4400–5088, 5195–5921, 6001–6455, 8143–8600	H $\beta$ , [OI], [OIII], [NII]
	4400–5088, 5195–5921, 6001–6640, 8143–8600	H $\beta$ , H $\alpha$ , [OI], [OIII], [NII]
IC 1459 (PA=30°) <sup>b,c,d</sup>	4276–4992, 5091–5813, 5906–6455, 8144–8580	H $\gamma$ , H $\beta$ , [OI], [OIII], [NII], [NI]
	4040–4992, 5091–5813, 5906–6640, 8144–8580	H $\delta$ , H $\gamma$ , H $\beta$ , H $\alpha$ , [OI], [OIII], [NII], [NI]

NOTE—a: no CaT, b: shorter CaT, c: shorter optical range, d: wavelength gaps



galaxy spectrum, we computed the error-weighted mean obtained by the two fits and used it as final results. We used the standard deviation of the two fits as the systematic uncertainty, added in quadrature to the mean statistical uncertainty of the two fits. The final results are shown in Figure 3 and listed in Table 6.

One exception is IC 1459, for which we have two sets of observations that we fit separately, and for each of them we fit the spectra north and south of the galaxy center out to  $0.5 R_e$  separately. The stellar population parameter trends of these sets are mostly similar. There are some differences, which are probably caused by the slightly different wavelength regions of the two sets. For example, the NaD feature lies in a chip gap in the PA=30° spectra, leading to larger statistical uncertainties and a higher [Na/H] estimate. We chose a narrower fitting range of [Na/H] for the PA=30° spectra based on the PA=0° results. On the other hand, the Mgb feature is missing in the PA=0° spectra. As this causes large differences for [Mg/H] and influences some other elemental abundances, we narrowed the fitting range of [Mg/H] for the PA=0° fits to values close to the PA=30° results. Again, we computed the error-weighted mean of each stellar parameter at a given radius, combining the results obtained from four different spectra and two different fit settings. In the outer bins, where the S/N of the PA=0° spectra is significantly lower than the PA=30° spectra due to the smaller slit width, we use only the results obtained from the PA=30° data.

### C.2. Extrapolation of Elemental Response Functions

We measured elemental abundances by applying linear multiplicative response functions for each individual element (Vaughan et al. 2018a,b), using the response functions of Conroy et al. (2018). These are computed at reference values of  $[X/H]=\pm 0.3$  dex for most elements,  $[C/H]=\pm 0.15$  dex, and  $[Na/H]=\pm 0.3, +0.6$ , and  $+0.9$  dex. PYSTAFF applies a Taylor expansion near the reference value to obtain the response functions at a given value of  $[X/H]$ . In most of our spectral fits, the elemental abundance value does not exceed the reference value. However, for  $[O/H]$  and  $[C/H]$ , we often obtain results that exceed the reference value. For  $[O/H]$ , we reach values as high as 0.44 dex, and for  $[C/H]$  0.26 dex.

We compared the Taylor expansion to a linear extrapolation of the response function in Figure 14. For a SSP with age  $t=10$  Gyr,  $[Z/H]=0.2$  dex,  $x_1=x_2=2.3$ ,  $[Na/H]=0.6$  dex, and otherwise  $[X/H]=0$  dex, we show the flux ratio of  $[C/H]$  (left panel) and  $[O/H]$  (right panel) enhanced SSP models to a model with  $[C/H]=0$  dex and  $[O/H]=0$  dex, respectively. Solid lines

denote the PYSTAFF Taylor expansion at different values, dashed lines denote a simple linear extrapolation from  $[C/H]=0$  and  $[C/H]=0.15$  dex to the denoted values (0.25, 0.30, and 0.35 dex). For carbon, we see that the linear extrapolation (orange and black dashed lines) has lower flux ratios than the respective PYSTAFF Taylor expansion (pink and red) at the same values. This means that the PYSTAFF extrapolated model deviates more from the solar-scaled model at a given value than a simple linear extrapolation. For a certain observed spectrum with non-solar abundance, the required PYSTAFF abundance value to match the spectrum will be lower. Our comparison with linearly interpolated models in 0.05 dex steps (Figure 14) suggests that this effect is  $<0.05$  dex for  $[C/H]$ .

For  $[O/H]$  (right panel) the difference is larger. A PYSTAFF model with  $[O/H]=0.5$  dex (solid red) deviates more from the  $[O/H]=0.0$  dex spectrum than a linearly extrapolated  $[O/H]=0.6$  dex spectrum (dashed orange). Our PYSTAFF extrapolated model at  $[O/H]=0.4$  dex is similar to the linearly interpolated  $[O/H]=0.5$  dex model. We conclude that our  $[O/H]$  measurements that exceed the reference value of  $[O/H]=0.3$  dex may be biased to lower values by up to 0.1 dex compared to other methods of extrapolation.

### C.3. Stellar Population Results per Radial Bin and Galaxy

We list our final SSP fit results in Table 6. The results were obtained by fitting the spectra in the wavelength ranges and with the emission lines listed in Table 5. We used two wavelength fitting ranges for each spectrum and list the error-weighted mean of the two settings, the standard deviation of the two settings is included in the listed uncertainties.

### C.4. Comparison to Other Studies

#### C.4.1. Ages and $[Z/H]$

Our ranges of age  $t$  and  $[Z/H]$ , and the respective gradient measurements, are within typical values of elliptical galaxies found in other studies, including those by Mehlert et al. (2003); Sánchez-Blázquez et al. (2007); Annibali et al. (2007); Kuntschner et al. (2010); González Delgado et al. (2014); Wilkinson et al. (2015); Krajnović et al. (2020).

Some studies derived ages and  $[Z/H]$  for individual galaxies in our sample, though sometimes only for the center. We are in agreement to within the uncertainties for the ages of NGC 1404 (Trager et al. 2000b; Amblard et al. 2014), NGC 4552 (Trager et al. 2000a; Thomas et al. 2005; Amblard et al. 2014; Martín-Navarro et al. 2015a; McDerimid et al. 2015; van Dokkum et al. 2017),

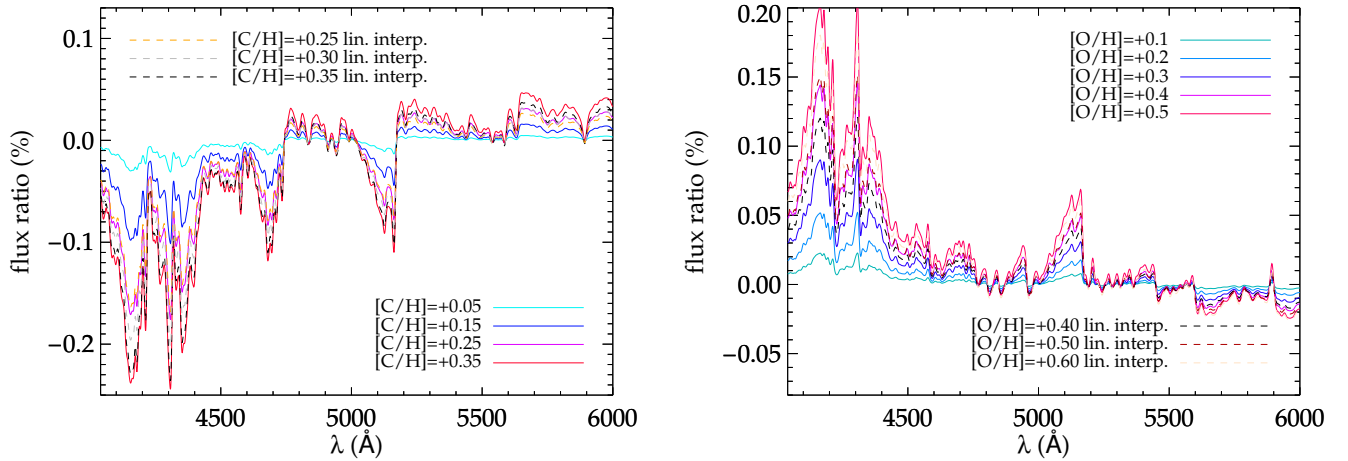


**Figure 14.** Flux ratio of [C/H] enhanced (left) and [O/H] enhanced (right) SSP models with respect to solar models. Solid lines denote the PYSTAFF Taylor expansion, dashed lines a simple linear extrapolation.

NGC 3923 (Amblard et al. 2014; Carlsten et al. 2017), NGC 4697 (Trager et al. 2000a; Thomas et al. 2005; Annibali et al. 2007; Serra & Oosterloo 2010; McDermid et al. 2015), NGC 5061 (Amblard et al. 2014), NGC 7796 (Thomas et al. 2005; Rosa et al. 2018), and IC 1459 (Amblard et al. 2014). However, some studies found younger ages by several Gyr than we did and we are not in agreement to within the uncertainties, in particular for NGC 3923 (Thomas et al. 2005), NGC 4697 (Amblard et al. 2014), NGC 4552 (Annibali et al. 2007) and IC 1459 (Annibali et al. 2007; Serra & Oosterloo 2010; Prichard et al. 2019).

We evaluated the accuracy and precision of our PYSTAFF fits of NGC 3923 in Feldmeier-Krause et al. (2020) using SSP model spectra to simulate realistic observations by adding noise in several realizations. Indeed, the ages tend to be slightly overestimated ( $\sim 0.5$  Gyr). We conclude that our ages may be biased to older ages, but this is only a small effect. Our ages agree with several studies in the literature to within their  $1\sigma$  uncertainties.

Most studies in the literature used different methods and SSP models, which are computed using different isochrones and have different approaches to deal with the metallicity [Z/H] (see review by Conroy 2013). One exception is the work by Prichard et al. (2019), who used PYSTAFF and Conroy et al. (2018) SSP models, as we did, to analyze MUSE ( $\sim 4700$ – $6800$  Å) and KMOS data ( $\sim 8100$ – $9000$ ,  $9700$ – $10100$  Å) of IC 1459. They binned their data in three concentric rings and found a slightly negative metallicity gradient, though it is consistent with being constant [Z/H]=0.15 dex out to  $\sim 0.2 R_e$ .

We analyzed five spectral bins in the same radial range as their three spectra, and found decreasing [Z/H] from 0.13 to  $-0.09$  dex (deviating from Prichard et al. 2019 by  $1.0$ – $3.2 \sigma$ ), while our ages are higher by 4 Gyr in the center and  $\sim 2.5$  Gyr in the outer region (deviating by  $2.7$ – $1.5 \sigma$ ). Prichard et al. (2019) did not include the emission line doublet [N I] $_{\lambda\lambda 5197.90, 5200.39}$  to their fit, and their Figure 7 shows residuals in the spectra at  $5200$  Å, especially in the center. We tested fitting our central spectrum and neglecting [N I] emission. The change of most parameters was within  $1 \sigma$ ; the age decreased by 1 Gyr, [Z/H] decreased by 0.01 dex. Since [N I] emission decreases with increasing radius, neglecting it has the largest effect in the center, and may decrease the age difference there from  $2.7$  to  $\sim 2.1 \sigma$ . Though, the effect of including [N I] may be different for the wavelength region used by Prichard et al. (2019). The lower [Z/H] we obtain at  $0.2 R_e$  does not come from [N I]. Using fixed solar [Z/H], Baldwin et al. (2018) showed that ages measured from near-infrared spectra are less precise than from optical spectra. The different wavelength regions might cause the age discrepancy of  $2 \sigma$ , and in combination with the age-metallicity anti-correlation, cause the discrepancy of [Z/H].

#### C.4.2. Elemental Abundances

Our elemental abundance measurements are in rough agreement with studies of other galaxies. In particular, the ranges of Fe, Mg, Ca, C and N agree with the results of Schiavon (2007), Graves et al. (2007) and Smith et al. (2009), and the ranges of Mg, O, C, Ca, and Na with van Dokkum et al. (2017). In addition, our ranges of

Fe and Ca agree with [Conroy et al. \(2014\)](#) and [Greene et al. \(2015\)](#). Though, Mg, C, and N of [Greene et al. \(2015\)](#) tend to be higher; while Mg, C, and O of [Conroy et al. \(2014\)](#) tend to be lower. Also, we have a wider range of values for N, Si, Ti than [Conroy et al. \(2014\)](#). Our ranges of N and Na roughly agree with [Worthey et al. \(2014\)](#), but we have higher values of Mg, Ca, and C, and a narrower range of O, and Si.

The different results are, to some extent, caused by different approaches and data: [Schiavon \(2007\)](#), [Conroy et al. \(2014\)](#), and [Worthey et al. \(2014\)](#) did not measure radial gradients but rather total galaxy parameters. Most of the aforementioned studies used stacked spectra. Only [Smith et al. \(2009\)](#) and [van Dokkum et al. \(2017\)](#) analyzed individual galaxies, [Worthey et al. \(2014\)](#) derived abundances for both stacked spectra and individual galaxies. Their analysis showed that the elemental abundance ranges spanned by individual galaxies exceeds the abundance trends of stacked spectra binned by velocity dispersion. This explains why several of our abundance ranges are larger than in studies of stacked spectra in the literature.

#### C.4.3. Elemental Abundance Gradients

There are several papers on abundance gradients of individual galaxies. Often they do not measure individual elements but  $[\alpha/\text{Fe}]$ , as the data quality is too low to measure individual elemental abundances. These studies (e.g. [Mehlert et al. 2003](#)) usually rely on the Mg**b** feature, and obtain  $[\alpha/\text{Fe}]$  values and gradients in agreement with our  $[\text{Mg}/\text{Fe}]$ . Further, our central values and  $\nabla_r$  of  $[\text{Mg}/\text{Fe}]$  and  $[\text{C}/\text{Fe}]$  are within the ranges found by [Ferreiras et al. \(2019\)](#).

Few studies measured elemental abundance gradients for a larger number of elements. [Greene et al. \(2013, 2015\)](#) and [Parikh et al. \(2019\)](#) used spectral indices of stacked galaxy spectra. Our values for  $\nabla_r[\text{Mg}/\text{Fe}]$ ,  $\nabla_r[\text{Ca}/\text{Fe}]$ ,  $\nabla_r[\text{N}/\text{Fe}]$ ,  $\nabla_r[\text{Na}/\text{Fe}]$ , and  $\nabla_r[\text{Ti}/\text{Fe}]$  are similar to the results of [Parikh et al. \(2019\)](#) for most galaxies, though we obtain a steeper decreasing  $[\text{Z}/\text{H}]$ . As [Greene et al. \(2013, 2015\)](#), we obtain rather flat  $[\text{Mg}/\text{Fe}]$  and mild age gradients. However, we obtain relatively flat profiles for  $[\text{Fe}/\text{H}]$  and  $[\text{C}/\text{Fe}]$ , while [Greene et al. \(2013, 2015\)](#) find a steeper decrease with radius. One major difference with these studies is that they have no fitting parameter  $[\text{Z}/\text{H}]$ , which has a steep radial gradient in our analysis. The different treatment of metallicity in the [Schiavon \(2007\)](#) compared to the [Conroy et al. \(2018\)](#) SSP models that we use may cause their large  $\nabla_r[\text{Fe}/\text{H}]$  as opposed to our flat  $\nabla_r[\text{Fe}/\text{H}]$ . Further, [Greene et al. \(2015\)](#) found radially varying  $[\text{C}/\text{Fe}]$  and flat  $[\text{N}/\text{Fe}]$ , and we find the opposite. [Greene et al.](#)

(2013, 2015) measured  $[\text{C}/\text{Fe}]$  using the C<sub>2</sub>4668 index, and used this result to infer  $[\text{N}/\text{Fe}]$  from the CN<sub>1</sub> index. The predictions of the [Schiavon \(2007\)](#) and [Conroy et al. \(2018\)](#) SSP models for these Lick indices differ at ages  $>6$  Gyr, which may cause our discrepant results.

[van Dokkum et al. \(2017\)](#) measured elemental abundances as a function of radius for six galaxies, including NGC 4552, using full spectral fitting. Our general trends for  $[\text{Mg}/\text{Fe}]$ ,  $[\text{Ca}/\text{Fe}]$ ,  $[\text{Na}/\text{Fe}]$ ,  $[\text{C}/\text{Fe}]$  are similar, but [van Dokkum et al. \(2017\)](#) find steeper increasing  $[\text{O}/\text{Fe}]$ , steeper decreasing  $[\text{Fe}/\text{H}]$ , and overall older ages. They do not show their results for  $[\text{Z}/\text{H}]$ , Si, Ti, and N, so we cannot compare these. [van Dokkum et al. \(2017\)](#) fit more parameters than we do, in particular they include several other elemental abundances (K, V, Cr, Mn, Co, Ni, Sr, Ba), and a second, younger population in their fit. This likely causes the older age of their dominant stellar population compared to our SSP fit. It is not clear how other measurements may be affected, and if including a second stellar population can account for the different results.

## D. STAR FORMATION HISTORY AND TIME-SCALE

### D.1. Star Formation History

In Section 3 we fit a best-fit single stellar population (SSP) spectrum. Early-type galaxies are often dominated by an old population, which makes this approach reasonable for these cases. However, early-type galaxies can also have an extended star formation history or several bursts of star formation ([Thomas et al. 2005, 2010](#)). In particular, we obtained a young SSP age for NGC 5061 (3–5.5 Gyr). Here, we investigate if this galaxy has an unusual star formation history compared to the other galaxies.

We derived the star formation history using the program pPXF ([Cappellari & Emsellem 2004; Cappellari 2012, 2017](#)) and the [Conroy et al. \(2018\)](#) models with solar abundances as templates. We applied regularization as described by [Cappellari \(2017\)](#). The code pPXF obtains a best-fit model by assigning weights to the template spectra, which span a grid in age and  $[\text{Z}/\text{H}]$ . The best-fit spectrum is a linear combination of the template spectra, and we obtain the weights assigned to each individual template. We show the weight distributions obtained for the central spectra of five galaxies in Figure 15, assuming a Kroupa IMF slope. Applying the weights, we derived mass-weighted age and metallicity distributions, with a set of models with either [Kroupa \(2001\)](#)-like IMF slopes (i.e.  $x_1=1.3$ ,  $x_2=2.3$ ), or a bottom-heavy IMF ( $x_1=3.1$ ,  $x_2=3.3$ ). The bottom-heavy IMF resulted in slightly lower ages, but the overall

age and metallicity distributions are similar between the two sets of models.

The age distribution of NGC 5061 is more extended than the age distribution of the other galaxies in our sample. Most galaxies are dominated by old stars, formed  $\sim 9$ –13 Gyr ago, and have only a small weight contribution of younger ages. Some galaxies have contributions of lower  $[Z/H]$  at larger radii, indicating accreted material. However, the best fit for NGC 5061 gives non-zero contributions of model spectra with ages over the entire age range of the input models (1–13.5 Gyr). The mass-weighted NGC 5061 ages obtained with pPXF are higher (6–10 Gyr) than the light-weighted age obtained with PYSTAFF (3–5.5 Gyr). Young stars are brighter than old stars, and therefore they contribute more to light-weighted SSP age measurements than to mass-weighted SFH age (see also Serra & Trager 2007; McDermid et al. 2015).

Raimann et al. (2005) estimated the flux contributed by stars with ages of 3 Myr, 100 Myr, 1 Gyr, and 10 Gyr in NGC 5061, NGC 1404, and NGC 3923. Their analysis suggests comparable contributions of stars with 10 Gyr between the galaxies, but a relatively larger contribution of 100 Myr stars in NGC 5061 (6–12%) compared to the other two galaxies (3–6%). We cannot comment on this result, as we use SSP models in the age range of 1–13.5 Gyr. However, this work confirms that the contribution of young stars in NGC 5061 is larger than in other galaxies of our sample. We conclude that the PYSTAFF approach to find the best-fit single stellar population model is less appropriate for NGC 5061, as it has a higher fraction of young stars that bias the results compared to other galaxies in our sample.

#### D.2. Star Formation Time-scale Estimate

Various elements formed at different time-scales. In particular,  $\alpha$ -elements (O, Mg, Ca, Si, Ti) are formed in SN II explosions of massive stars, whereas Fe-peak elements are predominantly generated in SN Ia explosions, which happen later. The  $\alpha$ -element oxygen is, in addition, produced in low-to intermediate mass stars ( $0.8$ – $3.5 M_{\odot}$ , e.g. Marigo 2001), while nitrogen and carbon are formed in intermediate-mass stars ( $3$ – $8 M_{\odot}$ ). This means that the ratios of different elemental abundances depend on the star formation time-scale  $\Delta t$ .

Thomas et al. (2005) derived a relation for  $\Delta t$  and  $[\alpha/Fe]$ , using simulations of chemical evolution for toy galaxies with various extended star formation histories. Applying their relation to  $[Mg/Fe]$ , we calculated the star formation time-scales as a function of galaxy radius (see Figure 16, top panel). For most galaxies,  $\Delta t$  is consistent with being constant with radius within

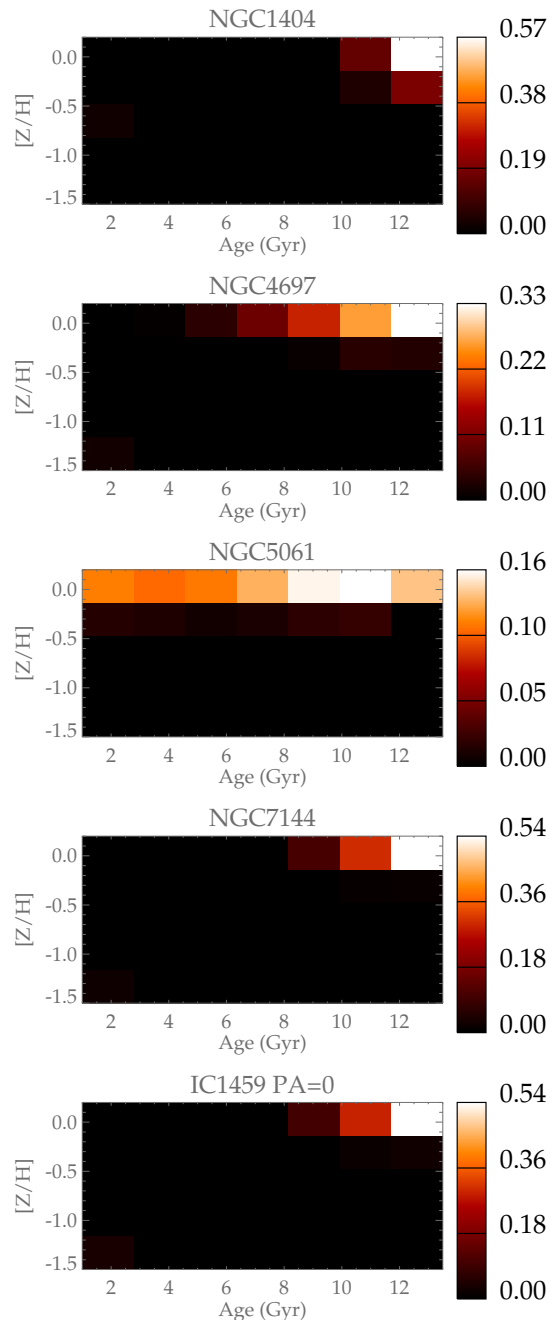


**Figure 15.** Star formation histories of several galaxies in the most central bin, assuming a Kroupa IMF. The colors denote mass weights. All galaxies have solar to super-solar  $[Z/H]$ , and are dominated by old stellar populations  $>10$  Gyr, including the galaxies which are not shown for brevity (NGC 3923, NGC 4552, NGC 7796). Only NGC 5061 has weight contributions  $>0.12$  at all age bins.

$1\sigma$ . Other galaxies show an increasing  $\Delta t$  with radius (NGC 4697, NGC 5061, and NGC 7796). NGC 4552, NGC 1404, and NGC 7796 have the shortest star formation time-scales. These galaxies are rather old and have

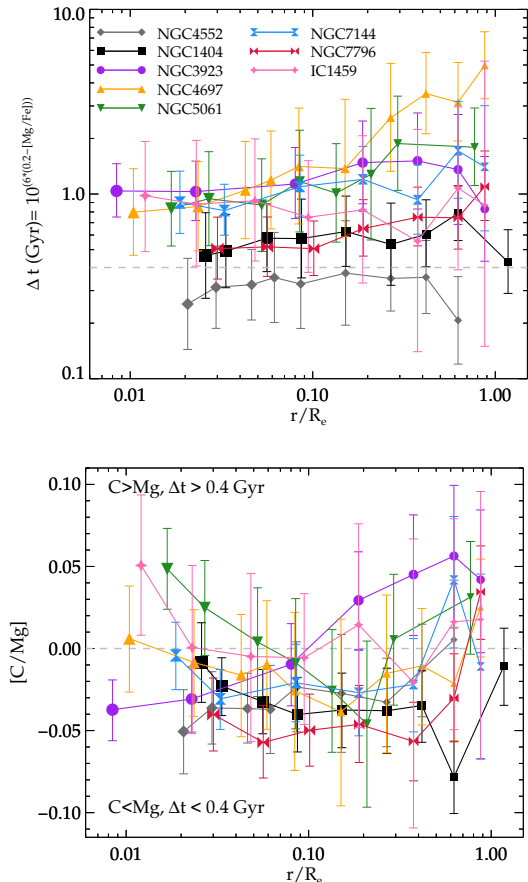


**Figure 16.** Star formation time-scale  $\Delta t$  for various galaxies, using the relation for  $[\alpha/\text{Fe}]$  derived by Thomas et al. (2005). In the upper panel we show  $\Delta t$ , in the lower panel  $[\text{C}/\text{Mg}]$  as function of radius. A value of  $[\text{C}/\text{Mg}] \lesssim 0$  indicates  $\Delta t < 0.4$  Gyr,  $[\text{C}/\text{Mg}] > 0$  longer time-scales. Different colors and symbols denote different galaxies, decreasing symbol size larger  $r/R_e$ .

a high velocity dispersion, which is in agreement with Thomas et al. (2005), who found that massive galaxies tend to have shorter  $\Delta t$  and therefore have older SSP ages than less massive galaxies (see also Longhetti et al. 2005; De Lucia et al. 2006).

We checked the consistency of our star formation time-scale estimate by comparing C and Mg. Johansson et al. (2012) argue that  $[\text{C}/\text{Mg}] = 0$  sets a limit on  $\Delta t$ , because a significant contribution of C comes from intermediate-mass stars. The lifetime of  $3 M_\odot$  stars is  $\sim 0.4$  Gyr (Portinari et al. 1998), and this is the star formation time-scale required to reach  $[\text{C}/\text{Mg}] = 0$ , or  $[\text{C}/\text{Fe}] = [\text{Mg}/\text{Fe}]$ . We show  $[\text{C}/\text{Mg}]$  as a function of radius in the lower panel of Figure 16. Here we have  $[\text{C}/\text{Mg}] < 0$  dex (indicating  $\Delta t \lesssim 0.4$  Gyr) for a larger number of galaxies compared to  $\Delta t$  from Mg and the Thomas et al. (2005) relation. NGC 4552, NGC 1404,

and NGC 7796 have low values of  $[\text{C}/\text{Mg}]$ , indicating again the short  $\Delta t$ . Some galaxies (e.g. NGC 4697, NGC 5061) have different radial trends in the two panels. These galaxies also have radially varying IMF slopes.

The time-scale estimate has several caveats, which may account for the differences: We assumed that  $[\alpha/\text{Fe}]$  used by Thomas et al. (2005) equals our  $[\text{Mg}/\text{Fe}]$ , which is not necessarily true (see also Conroy et al. 2014). When estimating the time-scale using  $[\text{C}/\text{Mg}]$ , only stellar masses from  $3 M_\odot$  upwards are considered, whereas  $[\text{Mg}/\text{Fe}]$  considers lower masses. Both time-scale indicators are based on the assumption of a constant IMF in all galaxies, which we have not found for the low-mass IMF in our data. Martín-Navarro et al. (2018) argue that the star formation time-scale alone cannot explain the observed  $[\text{Mg}/\text{Fe}]$  patterns of elliptical galaxies. Another caveat is that  $[\text{Z}/\text{H}]$  is not considered, although both Mg and C yields are  $[\text{Z}/\text{H}]$  dependent (Yan et al. 2019), and all galaxies have a significant  $[\text{Z}/\text{H}]$  gradient ( $\nabla_r [\text{Z}/\text{H}] = -0.13$  to  $-0.44$  dex/ $\log(r/R_e)$ ).

## E. NOTES ON INDIVIDUAL GALAXIES

Here, we summarise the properties of individual galaxies compared to others in the sample. Overall, we find a wide range of elemental abundance gradients, which reflects the different formation histories for individual galaxies in our sample.

**IC 1459** is old in the center, with a decreasing age. Remarkable are the steeply decreasing element abundance gradients (e.g. of Si, Ti, N, and Na), with high values in the center, and low values at  $1 R_e$  compared to other galaxies. This galaxy has an AGN and strong gas emission lines, which results in relatively large measurement uncertainties in the center. The ionised gas emission, counter-rotating core, shell-like remnants (Forbes et al. 1995) all are compatible with a gas-rich major merger, though the accretion of two counter-rotating cold gas streams in the first stage of IC 1459’s formation cannot be ruled out (Prichard et al. 2019). The rather young age and low elemental abundances at large radii suggest that a significant portion of younger, possibly accreted, stellar populations contributes to the total light. IC 1459 is the central galaxy in a rather small group.

**NGC 3923** has an extended shell system, and may have experienced a major merger event (Carlsten et al. 2017). Like IC 1459, this galaxy is the central galaxy in a group. However, we found significant differences in the stellar populations. NGC 3923 is  $\sim 10$  Gyr old, which makes it the youngest among the massive ( $\sigma > 200 \text{ km s}^{-1}$ ) galaxies. Carlsten et al. (2017) found

indications for a young sub-population in this galaxy. Also remarkable, and possibly connected to the younger age, are the relatively low values of  $[\text{O}/\text{Fe}]$ ,  $[\text{Mg}/\text{Fe}]$ ,  $[\text{Ca}/\text{Fe}]$ ,  $[\text{Ti}/\text{Fe}]$ ,  $[\text{C}/\text{Fe}]$  and high values of  $[\text{Fe}/\text{H}]$  in the center, suggesting a longer and thus apparently later episode of initial star formation. Some abundances are increasing with radius (C, N, O), whereas most  $\alpha$  elements,  $[\text{Fe}/\text{H}]$ , and  $[\text{Na}/\text{Fe}]$  are radially constant or slightly decreasing, as for other galaxies. However, the  $[\text{Na}/\text{Fe}]$  profile is relatively shallow. As a result, NGC 3923 has relatively high C, N, O, and Na at large radii compared to other galaxies. As these elements are produced, at least partially, in intermediate-mass stars, this may indicate that the IMF was initially favoring intermediate-mass over high-mass stars, thus enhancing C, N, O, and Na.

**NGC 1404** is the second brightest early-type galaxy of the Fornax cluster, though it is probably part of an infalling subgroup (Drinkwater et al. 2001; Machacek et al. 2005). The radial shape of the velocity dispersion is non-monotonic, possibly indicating overlapping structures. Iodice et al. (2019) see indications of a kinematically decoupled component in the central  $\sim 9''$ , with a double-peaked  $\sigma$ . This region corresponds to the inner six bins of our data, and explains our irregular  $\sigma$  profile. Not only the kinematics, but also the stellar populations in the inner region have non-monotonic radial profiles, e.g. age, IMF slope, C, N, O.

**NGC 4552** is in the Virgo cluster. It has a high, radially constant age and a steeply decreasing  $[\text{Z}/\text{H}]$  (Lonoce et al. 2021). The IMF slope is slightly decreasing with radius. Some peculiar properties of this galaxy are the non-monotonic  $[\text{Na}/\text{Fe}]$  profile, with higher values both in the center and at the outermost bin, and a radially increasing  $[\text{C}/\text{Fe}]$ ,  $[\text{N}/\text{Fe}]$  and  $[\text{O}/\text{Fe}]$  in the outer region, similar to NGC 3923. Both NGC 1404 and NGC 4552 have rather high values of  $[\text{Mg}/\text{Fe}]$  and  $[\text{C}/\text{Mg}]$ , which indicate short star formation time-scales. McDermid et al. (2015) found that Virgo cluster galaxies have systematically higher  $[\alpha/\text{Fe}]$  than non-Virgo galaxies, and suggest a suppression of extended star formation in Virgo galaxies.

**NGC 7796** is dominated by a very old stellar population at all radii, while  $[\text{Z}/\text{H}]$  is rather low compared to other galaxies, and it has a more shallow gradient. The IMF slope is consistent with being constant and Salpeter-like. For this galaxy we do not have CaT data, which is helpful to constrain the IMF (Feldmeier-Krause et al. 2020). Concerning elemental abundances, we found unusually flat radial profiles for O, Si, Ca, Ti, C, and Fe compared to other galaxies in our sample.  $[\text{Ca}/\text{Fe}]$ ,  $[\text{Si}/\text{Fe}]$ , and  $[\text{Ti}/\text{Fe}]$  in the outer regions are

higher than for any other galaxy. NGC 7796 is a field galaxy, which suggests a relatively low contribution of galaxy mergers (Lin et al. 2010), and hence flatter stellar population gradients.  $[\text{Mg}/\text{Fe}]$  is relatively high, and slightly decreasing as a function of radius. Our study confirms that this galaxy formed stars very fast and efficiently (Rosa et al. 2018).

**NGC 4697** is younger than other galaxies of our sample ( $< 9$  Gyr), and has on average lower elemental abundances, in particular  $[\text{O}/\text{Fe}]$ ,  $[\text{Mg}/\text{Fe}]$ ,  $[\text{Si}/\text{Fe}]$ ,  $[\text{C}/\text{Fe}]$ ,  $[\text{N}/\text{Fe}]$ ,  $[\text{Na}/\text{Fe}]$ . This suggests a longer timescale for initial star formation, with enough time to enrich the gas with  $[\text{Fe}/\text{H}]$ .  $[\text{Fe}/\text{H}]$  appears to be radially increasing, and several other elements therefore radially decreasing. The velocity dispersion is, together with NGC 7144, the lowest in our sample; thus the galaxy is less massive. This is in agreement with the model suggested by Thomas et al. (2010), that stars in a galaxy with high mass formed faster and earlier than in a less massive galaxy. NGC 4697 is also the only galaxy in our sample with a radially increasing  $\sigma$ . The IMF slope is non-monotonic, but overall slightly radially decreasing.

**NGC 7144**, part of a sparse group, has a radially decreasing age, but constant, Salpeter-like IMF slope.  $[\text{Z}/\text{H}]$  and several elemental abundances (Si, Ca, N, Na) are rather low. The radial gradients of Si, Ca, Ti are rather steeply decreasing, but flat for C and N.

**NGC 5061** has the youngest SSP age, and an extended star formation history (see Appendix D.1). Thus, the SSP values we measure are possibly inaccurate. The  $[\text{Z}/\text{H}]$  and IMF slope of NGC 5061 have the highest values of all galaxies in the center, while  $[\text{O}/\text{Fe}]$  is lowest. Also the  $[\text{Ti}/\text{Fe}]$  values in the center are higher than for the other galaxies.  $[\text{Na}/\text{Fe}]$  is decreasing steeply.

## F. ANALYSIS OF THE GIANT LOW-SURFACE BRIGHTNESS SPIRAL GALAXY UGC 1382

We observed UGC 1382 on September 20, 2014, believing it is an elliptical galaxy. However, Hagen et al. (2016) obtained deep photometry and discovered a disk and spiral arms surrounding UGC 1382. They classified UGC 1382 as giant low-surface brightness galaxy (LSBG). Here we describe the analysis and results for this galaxy. Due to its classification, we did not include this galaxy in our analysis of early-type galaxies.

We observed UGC 1382 with a slit width of  $1''.5$ , an exposure time of 50 min, and at a PA of  $90^\circ$  with the  $600\ell/9^\circ 78$  grating during a cloudy night. This causes the rather low S/N of the optical spectra compared to the data of other galaxies, and made the CaT data, and spectra at  $< 4390 \text{ \AA}$ , unusable. Due to the classification

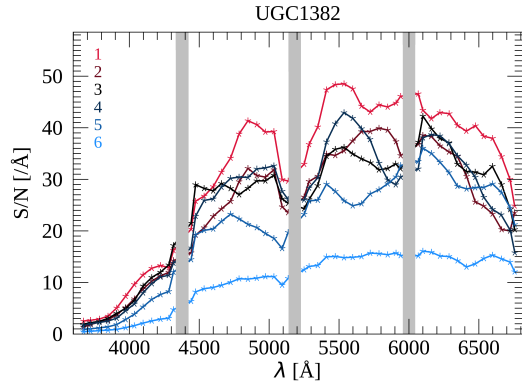


**Figure 17.** Signal-to-noise ratio as function of wavelength for UGC 1382, colors and symbols as in Figure 12.

as spiral galaxy, we did not repeat the observation to increase the S/N. Our optical spectra cover the bulge ( $R_e=3''.4$ ), which dominates the spectra of the inner four radial bins, and the inner disk out to  $1 R_e$  ( $16''$ , Hagen et al. 2016). We reduced the data in a similar way as described in Section 2.2. The S/N was so low that we did not extract the northern and southern spectra separately, but simply summed the spectra without correcting rotation. Still, the UGC 1382 spectra have the lowest S/N,  $<50$  at all radii and wavelengths, see Figure 12. This is caused by the poor observing conditions at the time of the observations.

The low S/N required some changes in the fitting procedure compared to the other galaxies. In the PYSTAFF SSP fit, we included the emission lines  $H\beta$ ,  $H\alpha$ , [OI], [OIII], [NII], similar to IC 1459, but we tied the gas kinematics of all emission lines together. We used the wavelength ranges 4340–4659, 4659–5053, 5122–5857, 5942–6635 Å, which is shorter than for the other galaxies. We used only one wavelength setting for this galaxy, as shortening the wavelength region even further may lead to less accurate results. Thus, we do not have systematic uncertainties from varying the wavelength region. Due to the low S/N, the fits already have rather large statistical errors.

Compared to the other galaxies, we obtain higher [Si/Fe] ( $\sim 0.2$  to  $0.4$  dex), [Ca/Fe] ( $\sim 0.0$  to  $0.15$  dex), [Ti/Fe] ( $\sim 0.15$  to  $0.35$  dex) values, and lower [N/Fe] ( $\sim -0.35$  to  $0.1$  dex) and [Na/Fe] ( $\sim -0.3$  to  $0.3$  dex). Several of our stellar population parameters have a large scatter over the radial range (e.g. IMF, [O/Fe], [C/Fe], [Ti/Fe], see also Table 6). For this reason, we are not sure how robust the elemental abundance and IMF measurements are. Also the radial gradient fits have large uncertainties. Rather robust measurements are the flat age ( $\sim 10$  Gyr), and the shallow [Z/H] gradient ( $-0.12$  dex/ $\log(r/R_e)$ ), with overall low values of [Z/H] ( $-0.05$  to  $-0.2$  dex), similar to the also isolated, but slightly older NGC 7796. The behavior of [Z/H], shared by UGC 1382 and NGC 7796 may be connected to their isolated locations.

**Table 6.** Stellar population results, as function of galaxy radius  $r/R_e$ , where we take the slit width into account, and distance from the galaxy center along the slit  $x/R_e$ . IMF denotes the low-mass IMF slope ( $0.08-1.0 M_\odot$ ). Uncertainties are quadratic sum of statistical and systematic uncertainties.

$r/R_e$	$x/R_e$	$\sigma$	$t$	[Z/H]	IMF	[O/Fe]	[Mg/Fe]	[Si/Fe]	[Ti/Fe]	[Fe/H]	[Na/Fe]	[C/Fe]	[N/Fe]	
		( $\text{km s}^{-1}$ )	(Gyr)	(dex)		(dex)	(dex)	(dex)	(dex)	(dex)	(dex)	(dex)	(dex)	
NGC 4552														
M89														
0.021	0.005	282 $^{+2}$	11.2 $^{+1.1}$	0.16 $^{+0.02}$	2.7 $^{+0.3}$	0.39 $^{+0.06}$	0.30 $^{+0.04}$	0.18 $^{+0.04}$	0.01 $^{+0.05}$	0.11 $^{+0.05}$	-0.04 $^{+0.04}$	0.67 $^{+0.07}$	0.25 $^{+0.04}$	0.21 $^{+0.06}$
0.030	0.022	262 $^{+2}$	11.5 $^{+0.7}$	0.16 $^{+0.01}$	2.8 $^{+0.2}$	0.38 $^{+0.04}$	0.28 $^{+0.04}$	0.17 $^{+0.04}$	0.02 $^{+0.05}$	0.07 $^{+0.04}$	-0.04 $^{+0.03}$	0.64 $^{+0.04}$	0.25 $^{+0.03}$	0.20 $^{+0.05}$
0.046	0.042	255 $^{+2}$	12.5 $^{+0.6}$	0.12 $^{+0.01}$	2.7 $^{+0.1}$	0.38 $^{+0.04}$	0.28 $^{+0.03}$	0.17 $^{+0.04}$	-0.01 $^{+0.04}$	0.09 $^{+0.04}$	-0.03 $^{+0.03}$	0.62 $^{+0.03}$	0.25 $^{+0.03}$	0.17 $^{+0.05}$
0.062	0.058	252 $^{+2}$	12.9 $^{+0.7}$	0.08 $^{+0.02}$	2.5 $^{+0.2}$	0.38 $^{+0.04}$	0.28 $^{+0.04}$	0.14 $^{+0.04}$	0.00 $^{+0.05}$	0.06 $^{+0.05}$	-0.02 $^{+0.03}$	0.59 $^{+0.04}$	0.24 $^{+0.04}$	0.19 $^{+0.05}$
0.086	0.084	248 $^{+2}$	12.5 $^{+0.8}$	0.05 $^{+0.02}$	2.7 $^{+0.2}$	0.39 $^{+0.05}$	0.28 $^{+0.04}$	0.16 $^{+0.05}$	0.02 $^{+0.05}$	0.07 $^{+0.05}$	-0.04 $^{+0.03}$	0.59 $^{+0.05}$	0.26 $^{+0.04}$	0.21 $^{+0.06}$
0.151	0.150	241 $^{+3}$	11.7 $^{+1.6}$	0.01 $^{+0.05}$	2.8 $^{+0.3}$	0.36 $^{+0.07}$	0.27 $^{+0.05}$	0.14 $^{+0.05}$	0.01 $^{+0.05}$	0.06 $^{+0.05}$	-0.03 $^{+0.04}$	0.52 $^{+0.09}$	0.24 $^{+0.05}$	0.17 $^{+0.07}$
0.268	0.267	224 $^{+3}$	11.0 $^{+1.3}$	-0.09 $^{+0.04}$	2.8 $^{+0.4}$	0.37 $^{+0.06}$	0.28 $^{+0.03}$	0.10 $^{+0.04}$	-0.00 $^{+0.03}$	0.04 $^{+0.04}$	-0.03 $^{+0.02}$	0.50 $^{+0.07}$	0.24 $^{+0.03}$	0.19 $^{+0.06}$
0.417	0.417	213 $^{+3}$	12.3 $^{+0.9}$	-0.28 $^{+0.02}$	2.4 $^{+0.2}$	0.45 $^{+0.03}$	0.28 $^{+0.03}$	0.13 $^{+0.04}$	-0.04 $^{+0.04}$	-0.07 $^{+0.04}$	-0.03 $^{+0.02}$	0.49 $^{+0.07}$	0.26 $^{+0.02}$	0.29 $^{+0.04}$
0.625	0.625	216 $^{+5}$	10.9 $^{+1.8}$	-0.39 $^{+0.03}$	2.3 $^{+0.1}$	0.55 $^{+0.02}$	0.31 $^{+0.04}$	0.15 $^{+0.06}$	-0.02 $^{+0.04}$	-0.03 $^{+0.06}$	-0.11 $^{+0.02}$	0.65 $^{+0.05}$	0.32 $^{+0.02}$	0.41 $^{+0.05}$
NGC1404														
0.026	0.005	238 $^{+2}$	12.7 $^{+0.6}$	0.12 $^{+0.02}$	2.0 $^{+0.3}$	0.41 $^{+0.04}$	0.26 $^{+0.04}$	0.16 $^{+0.04}$	0.04 $^{+0.04}$	0.11 $^{+0.04}$	-0.04 $^{+0.03}$	0.53 $^{+0.07}$	0.25 $^{+0.04}$	0.17 $^{+0.06}$
0.033	0.022	226 $^{+2}$	12.2 $^{+0.4}$	0.13 $^{+0.01}$	2.4 $^{+0.2}$	0.36 $^{+0.04}$	0.25 $^{+0.03}$	0.18 $^{+0.04}$	0.05 $^{+0.03}$	0.11 $^{+0.04}$	-0.04 $^{+0.03}$	0.50 $^{+0.06}$	0.23 $^{+0.03}$	0.15 $^{+0.08}$
0.056	0.050	232 $^{+2}$	11.9 $^{+0.7}$	0.09 $^{+0.02}$	2.5 $^{+0.2}$	0.33 $^{+0.04}$	0.24 $^{+0.03}$	0.13 $^{+0.03}$	0.04 $^{+0.03}$	0.11 $^{+0.04}$	-0.02 $^{+0.03}$	0.41 $^{+0.06}$	0.21 $^{+0.03}$	0.13 $^{+0.07}$
0.087	0.083	242 $^{+2}$	10.5 $^{+0.8}$	0.10 $^{+0.02}$	2.8 $^{+0.3}$	0.30 $^{+0.05}$	0.24 $^{+0.04}$	0.12 $^{+0.04}$	0.05 $^{+0.03}$	0.10 $^{+0.04}$	-0.03 $^{+0.03}$	0.36 $^{+0.04}$	0.20 $^{+0.03}$	0.12 $^{+0.08}$
0.152	0.150	242 $^{+2}$	10.0 $^{+0.9}$	0.07 $^{+0.02}$	2.8 $^{+0.2}$	0.29 $^{+0.04}$	0.23 $^{+0.03}$	0.10 $^{+0.04}$	0.00 $^{+0.03}$	0.07 $^{+0.04}$	-0.02 $^{+0.03}$	0.33 $^{+0.04}$	0.20 $^{+0.03}$	0.12 $^{+0.11}$
0.268	0.267	236 $^{+2}$	10.6 $^{+1.7}$	0.02 $^{+0.05}$	2.5 $^{+0.4}$	0.34 $^{+0.05}$	0.25 $^{+0.04}$	0.08 $^{+0.05}$	0.01 $^{+0.04}$	0.09 $^{+0.04}$	-0.04 $^{+0.03}$	0.35 $^{+0.06}$	0.21 $^{+0.03}$	0.08 $^{+0.12}$
0.418	0.417	218 $^{+2}$	11.8 $^{+0.9}$	-0.07 $^{+0.02}$	2.2 $^{+0.2}$	0.35 $^{+0.03}$	0.24 $^{+0.03}$	0.11 $^{+0.04}$	0.01 $^{+0.03}$	0.06 $^{+0.04}$	-0.01 $^{+0.02}$	0.36 $^{+0.03}$	0.20 $^{+0.03}$	0.06 $^{+0.07}$
0.626	0.625	208 $^{+2}$	10.5 $^{+0.7}$	-0.16 $^{+0.02}$	2.1 $^{+0.2}$	0.28 $^{+0.04}$	0.22 $^{+0.02}$	0.09 $^{+0.03}$	-0.03 $^{+0.03}$	-0.03 $^{+0.05}$	0.03 $^{+0.02}$	0.29 $^{+0.03}$	0.14 $^{+0.02}$	0.11 $^{+0.05}$
1.175	1.175	196 $^{+4}$	9.4 $^{+1.0}$	-0.31 $^{+0.02}$	2.4 $^{+0.1}$	0.49 $^{+0.02}$	0.26 $^{+0.03}$	0.11 $^{+0.03}$	-0.03 $^{+0.04}$	-0.09 $^{+0.05}$	-0.05 $^{+0.02}$	0.31 $^{+0.03}$	0.25 $^{+0.02}$	0.06 $^{+0.14}$
NGC3923														
0.008	0.004	257 $^{+2}$	9.9 $^{+1.3}$	0.17 $^{+0.03}$	2.5 $^{+0.3}$	0.36 $^{+0.03}$	0.20 $^{+0.02}$	0.16 $^{+0.04}$	-0.02 $^{+0.04}$	0.03 $^{+0.05}$	0.02 $^{+0.02}$	0.53 $^{+0.03}$	0.16 $^{+0.02}$	0.19 $^{+0.04}$
0.023	0.022	254 $^{+3}$	10.1 $^{+1.4}$	0.14 $^{+0.03}$	2.5 $^{+0.3}$	0.36 $^{+0.03}$	0.20 $^{+0.03}$	0.15 $^{+0.04}$	-0.01 $^{+0.04}$	0.03 $^{+0.05}$	0.01 $^{+0.02}$	0.53 $^{+0.03}$	0.17 $^{+0.02}$	0.19 $^{+0.04}$
0.080	0.080	240 $^{+3}$	9.8 $^{+1.5}$	0.05 $^{+0.04}$	2.4 $^{+0.3}$	0.38 $^{+0.04}$	0.19 $^{+0.03}$	0.14 $^{+0.05}$	0.01 $^{+0.05}$	-0.03 $^{+0.07}$	-0.00 $^{+0.02}$	0.51 $^{+0.04}$	0.18 $^{+0.03}$	0.21 $^{+0.05}$
0.188	0.188	216 $^{+2}$	10.0 $^{+0.6}$	-0.10 $^{+0.02}$	2.2 $^{+0.2}$	0.43 $^{+0.03}$	0.17 $^{+0.04}$	0.15 $^{+0.05}$	0.00 $^{+0.05}$	-0.04 $^{+0.06}$	-0.02 $^{+0.03}$	0.39 $^{+0.07}$	0.20 $^{+0.03}$	0.24 $^{+0.06}$
0.375	0.375	212 $^{+4}$	9.2 $^{+1.1}$	-0.22 $^{+0.02}$	2.0 $^{+0.3}$	0.47 $^{+0.03}$	0.17 $^{+0.04}$	0.11 $^{+0.05}$	-0.02 $^{+0.05}$	-0.07 $^{+0.06}$	-0.04 $^{+0.03}$	0.37 $^{+0.04}$	0.22 $^{+0.03}$	0.23 $^{+0.09}$
0.625	0.625	205 $^{+5}$	8.1 $^{+1.6}$	-0.29 $^{+0.03}$	2.1 $^{+0.2}$	0.50 $^{+0.03}$	0.18 $^{+0.05}$	0.06 $^{+0.07}$	-0.02 $^{+0.05}$	-0.08 $^{+0.06}$	-0.07 $^{+0.03}$	0.36 $^{+0.04}$	0.23 $^{+0.03}$	0.30 $^{+0.10}$
0.875	0.875	197 $^{+5}$	7.8 $^{+1.8}$	-0.35 $^{+0.04}$	1.8 $^{+0.3}$	0.53 $^{+0.03}$	0.21 $^{+0.05}$	0.04 $^{+0.07}$	-0.02 $^{+0.05}$	-0.11 $^{+0.05}$	-0.10 $^{+0.02}$	0.35 $^{+0.04}$	0.26 $^{+0.03}$	0.34 $^{+0.17}$
NGC4697														
0.010	0.005	165 $^{+2}$	9.2 $^{+0.7}$	0.18 $^{+0.02}$	2.1 $^{+0.3}$	0.36 $^{+0.04}$	0.22 $^{+0.04}$	0.09 $^{+0.04}$	0.06 $^{+0.03}$	0.07 $^{+0.04}$	-0.05 $^{+0.03}$	0.36 $^{+0.04}$	0.22 $^{+0.03}$	0.11 $^{+0.06}$
0.024	0.022	146 $^{+2}$	8.3 $^{+0.6}$	0.17 $^{+0.02}$	2.4 $^{+0.2}$	0.31 $^{+0.04}$	0.21 $^{+0.04}$	0.07 $^{+0.04}$	0.05 $^{+0.03}$	0.07 $^{+0.04}$	-0.04 $^{+0.03}$	0.29 $^{+0.04}$	0.20 $^{+0.03}$	0.09 $^{+0.05}$
0.043	0.042	150 $^{+2}$	7.9 $^{+0.5}$	0.14 $^{+0.02}$	2.6 $^{+0.2}$	0.28 $^{+0.04}$	0.20 $^{+0.04}$	0.05 $^{+0.04}$	0.03 $^{+0.04}$	0.06 $^{+0.04}$	-0.04 $^{+0.03}$	0.23 $^{+0.04}$	0.18 $^{+0.03}$	0.01 $^{+0.07}$
0.059	0.058	149 $^{+2}$	7.5 $^{+0.5}$	0.13 $^{+0.02}$	2.7 $^{+0.2}$	0.26 $^{+0.05}$	0.19 $^{+0.04}$	0.03 $^{+0.04}$	0.03 $^{+0.04}$	0.05 $^{+0.04}$	-0.04 $^{+0.03}$	0.20 $^{+0.05}$	0.18 $^{+0.03}$	0.01 $^{+0.06}$

Table 6 continued



Table 6 (continued)

$r/R_e$	$x/R_e$	$\sigma$	$t$	$[Z/H]$	IMF	$[O/Fe]$	$[Mg/Fe]$	$[Si/Fe]$	$[Ca/Fe]$	$[Ti/Fe]$	$[Fe/H]$	$[Na/Fe]$	$[C/Fe]$	$[N/Fe]$	
		( $\text{km s}^{-1}$ )	(Gyr)	(dex)		(dex)	(dex)	(dex)	(dex)	(dex)	(dex)	(dex)	(dex)	(dex)	
0.084	0.083	152 <sup>+2</sup> <sub>-2</sub>	6.8 <sup>+0.5</sup> <sub>-0.5</sub>	0.10 <sup>+0.03</sup> <sub>-0.03</sub>	3.0 <sup>+0.3</sup> <sub>-0.3</sub>	0.18 <sup>+0.06</sup> <sub>-0.07</sub>	0.18 <sup>+0.05</sup> <sub>-0.05</sub>	0.02 <sup>+0.04</sup> <sub>-0.05</sub>	0.02 <sup>+0.04</sup> <sub>-0.04</sub>	0.04 <sup>+0.05</sup> <sub>-0.05</sub>	-0.03 <sup>+0.03</sup> <sub>-0.03</sub>	0.16 <sup>+0.06</sup> <sub>-0.06</sub>	0.15 <sup>+0.03</sup> <sub>-0.03</sub>	-0.06 <sup>+0.07</sup> <sub>-0.06</sub>	
0.150	0.150	156 <sup>+3</sup> <sub>-3</sub>	6.7 <sup>+0.8</sup> <sub>-0.9</sub>	0.04 <sup>+0.05</sup> <sub>-0.05</sub>	2.8 <sup>+0.3</sup> <sub>-0.3</sub>	0.20 <sup>+0.07</sup> <sub>-0.07</sub>	0.18 <sup>+0.06</sup> <sub>-0.06</sub>	-0.00 <sup>+0.05</sup> <sub>-0.06</sub>	0.01 <sup>+0.04</sup> <sub>-0.04</sub>	0.03 <sup>+0.06</sup> <sub>-0.06</sub>	-0.02 <sup>+0.03</sup> <sub>-0.04</sub>	0.09 <sup>+0.09</sup> <sub>-0.09</sub>	0.14 <sup>+0.04</sup> <sub>-0.04</sub>	-0.08 <sup>+0.08</sup> <sub>-0.08</sub>	
0.267	0.267	169 <sup>+3</sup> <sub>-3</sub>	7.2 <sup>+0.6</sup> <sub>-0.6</sub>	-0.10 <sup>+0.03</sup> <sub>-0.03</sub>	2.8 <sup>+0.3</sup> <sub>-0.3</sub>	0.18 <sup>+0.06</sup> <sub>-0.06</sub>	0.13 <sup>+0.05</sup> <sub>-0.05</sub>	-0.01 <sup>+0.05</sup> <sub>-0.05</sub>	-0.00 <sup>+0.03</sup> <sub>-0.03</sub>	-0.01 <sup>+0.06</sup> <sub>-0.06</sub>	0.00 <sup>+0.02</sup> <sub>-0.02</sub>	-0.00 <sup>+0.07</sup> <sub>-0.07</sub>	0.12 <sup>+0.03</sup> <sub>-0.03</sub>	-0.20 <sup>+0.06</sup> <sub>-0.06</sub>	
0.417	0.417	168 <sup>+3</sup> <sub>-3</sub>	7.3 <sup>+0.5</sup> <sub>-0.5</sub>	-0.14 <sup>+0.02</sup> <sub>-0.02</sub>	2.5 <sup>+0.2</sup> <sub>-0.2</sub>	0.24 <sup>+0.04</sup> <sub>-0.04</sub>	0.11 <sup>+0.04</sup> <sub>-0.04</sub>	-0.04 <sup>+0.04</sup> <sub>-0.04</sub>	-0.06 <sup>+0.03</sup> <sub>-0.03</sub>	-0.11 <sup>+0.05</sup> <sub>-0.05</sub>	0.03 <sup>+0.02</sup> <sub>-0.02</sub>	-0.09 <sup>+0.05</sup> <sub>-0.06</sub>	0.10 <sup>+0.02</sup> <sub>-0.02</sub>	-0.15 <sup>+0.08</sup> <sub>-0.07</sub>	
0.625	0.625	163 <sup>+3</sup> <sub>-3</sub>	7.9 <sup>+0.9</sup> <sub>-0.9</sub>	-0.25 <sup>+0.02</sup> <sub>-0.02</sub>	1.8 <sup>+0.3</sup> <sub>-0.3</sub>	0.27 <sup>+0.05</sup> <sub>-0.05</sub>	0.12 <sup>+0.03</sup> <sub>-0.03</sub>	-0.09 <sup>+0.04</sup> <sub>-0.04</sub>	-0.09 <sup>+0.03</sup> <sub>-0.03</sub>	-0.13 <sup>+0.05</sup> <sub>-0.04</sub>	0.01 <sup>+0.02</sup> <sub>-0.02</sub>	0.04 <sup>+0.04</sup> <sub>-0.05</sub>	0.10 <sup>+0.02</sup> <sub>-0.02</sub>	-0.10 <sup>+0.16</sup> <sub>-0.16</sub>	
0.875	0.875	156 <sup>+5</sup> <sub>-5</sub>	8.2 <sup>+0.8</sup> <sub>-0.8</sub>	-0.33 <sup>+0.02</sup> <sub>-0.02</sub>	2.2 <sup>+0.2</sup> <sub>-0.2</sub>	0.27 <sup>+0.05</sup> <sub>-0.05</sub>	0.08 <sup>+0.03</sup> <sub>-0.03</sub>	-0.05 <sup>+0.04</sup> <sub>-0.05</sub>	-0.04 <sup>+0.03</sup> <sub>-0.03</sub>	-0.19 <sup>+0.04</sup> <sub>-0.04</sub>	-0.02 <sup>+0.02</sup> <sub>-0.02</sub>	-0.01 <sup>+0.05</sup> <sub>-0.05</sub>	0.11 <sup>+0.02</sup> <sub>-0.02</sub>	0.03 <sup>+0.15</sup> <sub>-0.15</sub>	
NGC5061															
0.017	0.005	206 <sup>+2</sup> <sub>-2</sub>	3.0 <sup>+0.2</sup> <sub>-0.2</sub>	0.28 <sup>+0.02</sup> <sub>-0.02</sub>	3.3 <sup>+0.1</sup> <sub>-0.1</sub>	0.28 <sup>+0.04</sup> <sub>-0.04</sub>	0.21 <sup>+0.03</sup> <sub>-0.03</sub>	0.15 <sup>+0.04</sup> <sub>-0.04</sub>	-0.01 <sup>+0.03</sup> <sub>-0.03</sub>	0.28 <sup>+0.04</sup> <sub>-0.04</sub>	-0.08 <sup>+0.03</sup> <sub>-0.03</sub>	0.65 <sup>+0.03</sup> <sub>-0.03</sub>	0.26 <sup>+0.03</sup> <sub>-0.03</sub>	0.31 <sup>+0.04</sup> <sub>-0.04</sub>	
0.027	0.022	184 <sup>+2</sup> <sub>-2</sub>	3.0 <sup>+0.2</sup> <sub>-0.2</sub>	0.27 <sup>+0.02</sup> <sub>-0.02</sub>	3.3 <sup>+0.1</sup> <sub>-0.1</sub>	0.21 <sup>+0.05</sup> <sub>-0.05</sub>	0.20 <sup>+0.04</sup> <sub>-0.04</sub>	0.11 <sup>+0.04</sup> <sub>-0.04</sub>	-0.02 <sup>+0.04</sup> <sub>-0.04</sub>	0.24 <sup>+0.04</sup> <sub>-0.04</sub>	-0.06 <sup>+0.03</sup> <sub>-0.03</sub>	0.60 <sup>+0.04</sup> <sub>-0.04</sub>	0.23 <sup>+0.04</sup> <sub>-0.04</sub>	0.23 <sup>+0.05</sup> <sub>-0.05</sub>	
0.053	0.050	179 <sup>+2</sup> <sub>-2</sub>	3.0 <sup>+0.2</sup> <sub>-0.2</sub>	0.22 <sup>+0.02</sup> <sub>-0.02</sub>	3.4 <sup>+0.1</sup> <sub>-0.1</sub>	0.19 <sup>+0.06</sup> <sub>-0.06</sub>	0.21 <sup>+0.04</sup> <sub>-0.04</sub>	0.09 <sup>+0.04</sup> <sub>-0.04</sub>	-0.02 <sup>+0.04</sup> <sub>-0.04</sub>	0.19 <sup>+0.04</sup> <sub>-0.04</sub>	-0.07 <sup>+0.03</sup> <sub>-0.03</sub>	0.38 <sup>+0.04</sup> <sub>-0.04</sub>	0.21 <sup>+0.03</sup> <sub>-0.03</sub>	0.09 <sup>+0.07</sup> <sub>-0.07</sub>	
0.085	0.083	181 <sup>+2</sup> <sub>-2</sub>	3.6 <sup>+0.2</sup> <sub>-0.2</sub>	0.16 <sup>+0.02</sup> <sub>-0.02</sub>	3.4 <sup>+0.1</sup> <sub>-0.1</sub>	0.15 <sup>+0.06</sup> <sub>-0.06</sub>	0.19 <sup>+0.05</sup> <sub>-0.05</sub>	0.07 <sup>+0.04</sup> <sub>-0.04</sub>	-0.04 <sup>+0.04</sup> <sub>-0.04</sub>	0.15 <sup>+0.05</sup> <sub>-0.05</sub>	-0.05 <sup>+0.03</sup> <sub>-0.03</sub>	0.25 <sup>+0.04</sup> <sub>-0.04</sub>	0.18 <sup>+0.03</sup> <sub>-0.03</sub>	-0.02 <sup>+0.07</sup> <sub>-0.07</sub>	
0.134	0.133	174 <sup>+2</sup> <sub>-2</sub>	3.7 <sup>+0.2</sup> <sub>-0.2</sub>	0.11 <sup>+0.02</sup> <sub>-0.02</sub>	3.4 <sup>+0.1</sup> <sub>-0.1</sub>	0.13 <sup>+0.06</sup> <sub>-0.06</sub>	0.20 <sup>+0.04</sup> <sub>-0.04</sub>	0.06 <sup>+0.05</sup> <sub>-0.05</sub>	-0.02 <sup>+0.04</sup> <sub>-0.04</sub>	0.15 <sup>+0.05</sup> <sub>-0.05</sub>	-0.06 <sup>+0.03</sup> <sub>-0.03</sub>	0.20 <sup>+0.05</sup> <sub>-0.05</sub>	0.17 <sup>+0.03</sup> <sub>-0.03</sub>	-0.09 <sup>+0.08</sup> <sub>-0.08</sub>	
0.209	0.208	176 <sup>+3</sup> <sub>-3</sub>	4.0 <sup>+0.4</sup> <sub>-0.4</sub>	0.04 <sup>+0.04</sup> <sub>-0.04</sub>	3.3 <sup>+0.2</sup> <sub>-0.2</sub>	0.11 <sup>+0.08</sup> <sub>-0.08</sub>	0.18 <sup>+0.06</sup> <sub>-0.06</sub>	0.03 <sup>+0.07</sup> <sub>-0.07</sub>	-0.06 <sup>+0.05</sup> <sub>-0.05</sub>	0.12 <sup>+0.07</sup> <sub>-0.07</sub>	-0.02 <sup>+0.04</sup> <sub>-0.04</sub>	0.11 <sup>+0.08</sup> <sub>-0.08</sub>	0.14 <sup>+0.05</sup> <sub>-0.05</sub>	-0.09 <sup>+0.11</sup> <sub>-0.11</sub>	
0.292	0.292	168 <sup>+3</sup> <sub>-3</sub>	4.6 <sup>+0.2</sup> <sub>-0.2</sub>	-0.11 <sup>+0.02</sup> <sub>-0.02</sub>	2.9 <sup>+0.2</sup> <sub>-0.2</sub>	0.27 <sup>+0.06</sup> <sub>-0.06</sub>	0.15 <sup>+0.04</sup> <sub>-0.04</sub>	-0.10 <sup>+0.05</sup> <sub>-0.05</sub>	-0.04 <sup>+0.04</sup> <sub>-0.04</sub>	0.10 <sup>+0.05</sup> <sub>-0.05</sub>	-0.03 <sup>+0.03</sup> <sub>-0.03</sub>	0.10 <sup>+0.05</sup> <sub>-0.05</sub>	0.16 <sup>+0.03</sup> <sub>-0.03</sub>	-0.10 <sup>+0.07</sup> <sub>-0.07</sub>	
0.770	0.770	167 <sup>+5</sup> <sub>-5</sub>	5.5 <sup>+0.9</sup> <sub>-0.9</sub>	-0.33 <sup>+0.03</sup> <sub>-0.03</sub>	1.9 <sup>+0.3</sup> <sub>-0.3</sub>	0.42 <sup>+0.05</sup> <sub>-0.05</sub>	0.16 <sup>+0.03</sup> <sub>-0.03</sub>	-0.09 <sup>+0.08</sup> <sub>-0.08</sub>	-0.11 <sup>+0.03</sup> <sub>-0.03</sub>	0.03 <sup>+0.07</sup> <sub>-0.07</sub>	-0.07 <sup>+0.02</sup> <sub>-0.02</sub>	0.12 <sup>+0.04</sup> <sub>-0.04</sub>	0.19 <sup>+0.02</sup> <sub>-0.02</sub>	0.10 <sup>+0.09</sup> <sub>-0.09</sub>	
NGC7144															
0.019	0.007	158 <sup>+1</sup> <sub>-1</sub>	11.6 <sup>+0.7</sup> <sub>-0.7</sub>	0.14 <sup>+0.02</sup> <sub>-0.02</sub>	2.2 <sup>+0.2</sup> <sub>-0.2</sub>	0.31 <sup>+0.04</sup> <sub>-0.04</sub>	0.21 <sup>+0.03</sup> <sub>-0.03</sub>	0.10 <sup>+0.03</sup> <sub>-0.03</sub>	0.02 <sup>+0.03</sup> <sub>-0.03</sub>	0.06 <sup>+0.04</sup> <sub>-0.04</sub>	-0.01 <sup>+0.02</sup> <sub>-0.02</sub>	0.32 <sup>+0.03</sup> <sub>-0.03</sub>	0.20 <sup>+0.03</sup> <sub>-0.03</sub>	0.04 <sup>+0.08</sup> <sub>-0.08</sub>	
0.033	0.028	154 <sup>+2</sup> <sub>-2</sub>	10.2 <sup>+0.4</sup> <sub>-0.4</sub>	0.08 <sup>+0.01</sup> <sub>-0.01</sub>	2.4 <sup>+0.1</sup> <sub>-0.1</sub>	0.30 <sup>+0.03</sup> <sub>-0.03</sub>	0.21 <sup>+0.02</sup> <sub>-0.02</sub>	0.02 <sup>+0.08</sup> <sub>-0.08</sub>	0.02 <sup>+0.03</sup> <sub>-0.03</sub>	0.04 <sup>+0.03</sup> <sub>-0.03</sub>	-0.01 <sup>+0.02</sup> <sub>-0.02</sub>	0.26 <sup>+0.03</sup> <sub>-0.03</sub>	0.18 <sup>+0.02</sup> <sub>-0.02</sub>	-0.02 <sup>+0.12</sup> <sub>-0.12</sub>	
0.085	0.083	147 <sup>+1</sup> <sub>-1</sub>	11.0 <sup>+0.7</sup> <sub>-0.7</sub>	-0.10 <sup>+0.02</sup> <sub>-0.02</sub>	2.1 <sup>+0.3</sup> <sub>-0.3</sub>	0.32 <sup>+0.04</sup> <sub>-0.04</sub>	0.19 <sup>+0.03</sup> <sub>-0.03</sub>	0.09 <sup>+0.03</sup> <sub>-0.03</sub>	-0.04 <sup>+0.03</sup> <sub>-0.03</sub>	0.00 <sup>+0.04</sup> <sub>-0.04</sub>	0.00 <sup>+0.02</sup> <sub>-0.02</sub>	0.17 <sup>+0.04</sup> <sub>-0.04</sub>	0.17 <sup>+0.03</sup> <sub>-0.03</sub>	-0.16 <sup>+0.15</sup> <sub>-0.15</sub>	
0.188	0.188	138 <sup>+2</sup> <sub>-2</sub>	10.0 <sup>+0.5</sup> <sub>-0.5</sub>	-0.17 <sup>+0.02</sup> <sub>-0.02</sub>	2.3 <sup>+0.2</sup> <sub>-0.2</sub>	0.31 <sup>+0.04</sup> <sub>-0.04</sub>	0.19 <sup>+0.03</sup> <sub>-0.03</sub>	0.08 <sup>+0.04</sup> <sub>-0.04</sub>	-0.07 <sup>+0.03</sup> <sub>-0.03</sub>	0.00 <sup>+0.05</sup> <sub>-0.05</sub>	-0.00 <sup>+0.02</sup> <sub>-0.02</sub>	0.09 <sup>+0.04</sup> <sub>-0.04</sub>	0.16 <sup>+0.03</sup> <sub>-0.03</sub>	-0.20 <sup>+0.15</sup> <sub>-0.15</sub>	
0.375	0.375	129 <sup>+2</sup> <sub>-2</sub>	8.6 <sup>+0.8</sup> <sub>-0.8</sub>	-0.25 <sup>+0.02</sup> <sub>-0.02</sub>	2.4 <sup>+0.1</sup> <sub>-0.1</sub>	0.38 <sup>+0.04</sup> <sub>-0.04</sub>	0.21 <sup>+0.03</sup> <sub>-0.03</sub>	0.07 <sup>+0.04</sup> <sub>-0.04</sub>	-0.11 <sup>+0.03</sup> <sub>-0.03</sub>	0.01 <sup>+0.05</sup> <sub>-0.05</sub>	-0.03 <sup>+0.02</sup> <sub>-0.02</sub>	0.09 <sup>+0.04</sup> <sub>-0.04</sub>	0.18 <sup>+0.03</sup> <sub>-0.03</sub>	-0.09 <sup>+0.16</sup> <sub>-0.16</sub>	
0.625	0.625	139 <sup>+3</sup> <sub>-3</sub>	6.8 <sup>+1.0</sup> <sub>-1.0</sub>	-0.30 <sup>+0.04</sup> <sub>-0.04</sub>	2.4 <sup>+0.2</sup> <sub>-0.2</sub>	0.45 <sup>+0.05</sup> <sub>-0.05</sub>	0.16 <sup>+0.04</sup> <sub>-0.04</sub>	-0.02 <sup>+0.06</sup> <sub>-0.06</sub>	-0.13 <sup>+0.03</sup> <sub>-0.03</sub>	-0.15 <sup>+0.05</sup> <sub>-0.05</sub>	-0.05 <sup>+0.03</sup> <sub>-0.03</sub>	0.09 <sup>+0.05</sup> <sub>-0.05</sub>	0.20 <sup>+0.04</sup> <sub>-0.04</sub>	-0.17 <sup>+0.15</sup> <sub>-0.15</sub>	
0.875	0.875	142 <sup>+4</sup> <sub>-4</sub>	6.6 <sup>+1.1</sup> <sub>-1.0</sub>	-0.34 <sup>+0.05</sup> <sub>-0.05</sub>	2.2 <sup>+0.2</sup> <sub>-0.2</sub>	0.32 <sup>+0.11</sup> <sub>-0.11</sub>	0.18 <sup>+0.06</sup> <sub>-0.06</sub>	-0.07 <sup>+0.07</sup> <sub>-0.07</sub>	-0.20 <sup>+0.05</sup> <sub>-0.05</sub>	-0.17 <sup>+0.07</sup> <sub>-0.07</sub>	-0.05 <sup>+0.04</sup> <sub>-0.04</sub>	0.10 <sup>+0.08</sup> <sub>-0.08</sub>	0.16 <sup>+0.06</sup> <sub>-0.06</sub>	-0.09 <sup>+0.13</sup> <sub>-0.13</sub>	
NGC7796															
0.030	0.015	246 <sup>+2</sup> <sub>-2</sub>	12.9 <sup>+0.6</sup> <sub>-0.6</sub>	0.01 <sup>+0.02</sup> <sub>-0.02</sub>	2.3 <sup>+0.2</sup> <sub>-0.2</sub>	0.35 <sup>+0.04</sup> <sub>-0.04</sub>	0.25 <sup>+0.03</sup> <sub>-0.03</sub>	0.12 <sup>+0.04</sup> <sub>-0.04</sub>	0.05 <sup>+0.04</sup> <sub>-0.04</sub>	0.09 <sup>+0.04</sup> <sub>-0.04</sub>	-0.00 <sup>+0.02</sup> <sub>-0.02</sub>	0.55 <sup>+0.03</sup> <sub>-0.03</sub>	0.21 <sup>+0.03</sup> <sub>-0.03</sub>	0.25 <sup>+0.04</sup> <sub>-0.04</sub>	
0.056	0.050	241 <sup>+2</sup> <sub>-2</sub>	12.7 <sup>+0.8</sup> <sub>-0.8</sub>	-0.01 <sup>+0.02</sup> <sub>-0.02</sub>	2.4 <sup>+0.2</sup> <sub>-0.2</sub>	0.31 <sup>+0.04</sup> <sub>-0.04</sub>	0.25 <sup>+0.03</sup> <sub>-0.03</sub>	0.12 <sup>+0.04</sup> <sub>-0.04</sub>	0.06 <sup>+0.04</sup> <sub>-0.04</sub>	0.10 <sup>+0.04</sup> <sub>-0.04</sub>	-0.00 <sup>+0.02</sup> <sub>-0.02</sub>	0.50 <sup>+0.04</sup> <sub>-0.04</sub>	0.19 <sup>+0.03</sup> <sub>-0.03</sub>	0.23 <sup>+0.05</sup> <sub>-0.05</sub>	
0.101	0.098	236 <sup>+2</sup> <sub>-2</sub>	12.9 <sup>+0.6</sup> <sub>-0.6</sub>	-0.05 <sup>+0.02</sup> <sub>-0.02</sub>	2.4 <sup>+0.2</sup> <sub>-0.2</sub>	0.34 <sup>+0.04</sup> <sub>-0.04</sub>	0.25 <sup>+0.02</sup> <sub>-0.02</sub>	0.12 <sup>+0.03</sup> <sub>-0.03</sub>	0.07 <sup>+0.04</sup> <sub>-0.04</sub>	0.10 <sup>+0.04</sup> <sub>-0.04</sub>	0.00 <sup>+0.02</sup> <sub>-0.02</sub>	0.44 <sup>+0.05</sup> <sub>-0.05</sub>	0.20 <sup>+0.02</sup> <sub>-0.02</sub>	0.21 <sup>+0.05</sup> <sub>-0.05</sub>	
0.189	0.188	234 <sup>+2</sup> <sub>-2</sub>	12.9 <sup>+0.6</sup> <sub>-0.6</sub>	-0.08 <sup>+0.02</sup> <sub>-0.02</sub>	2.5 <sup>+0.2</sup> <sub>-0.2</sub>	0.30 <sup>+0.04</sup> <sub>-0.04</sub>	0.23 <sup>+0.02</sup> <sub>-0.02</sub>	0.12 <sup>+0.04</sup> <sub>-0.04</sub>	0.02 <sup>+0.04</sup> <sub>-0.04</sub>	0.10 <sup>+0.04</sup> <sub>-0.04</sub>	0.02 <sup>+0.02</sup> <sub>-0.02</sub>	0.35 <sup>+0.03</sup> <sub>-0.03</sub>	0.18 <sup>+0.03</sup> <sub>-0.03</sub>	0.16 <sup>+0.05</sup> <sub>-0.05</sub>	
0.376	0.375	228 <sup>+2</sup> <sub>-2</sub>	13.0 <sup>+0.6</sup> <sub>-0.6</sub>	-0.13 <sup>+0.02</sup> <sub>-0.02</sub>	2.3 <sup>+0.3</sup> <sub>-0.3</sub>	0.27 <sup>+0.05</sup> <sub>-0.05</sub>	0.22 <sup>+0.03</sup> <sub>-0.03</sub>	0.09 <sup>+0.04</sup> <sub>-0.04</sub>	0.01 <sup>+0.05</sup> <sub>-0.05</sub>	0.11 <sup>+0.04</sup> <sub>-0.04</sub>	0.01 <sup>+0.02</sup> <sub>-0.02</sub>	0.32 <sup>+0.03</sup> <sub>-0.03</sub>	0.16 <sup>+0.03</sup> <sub>-0.03</sub>	0.08 <sup>+0.06</sup> <sub>-0.06</sub>	
0.626	0.625	214 <sup>+3</sup> <sub>-3</sub>	13.4 <sup>+0.6</sup> <sub>-0.6</sub>	-0.20 <sup>+0.02</sup> <sub>-0.02</sub>	2.2 <sup>+0.3</sup> <sub>-0.3</sub>	0.33 <sup>+0.05</sup> <sub>-0.05</sub>	0.22 <sup>+0.03</sup> <sub>-0.03</sub>	0.10 <sup>+0.04</sup> <sub>-0.04</sub>	0.02 <sup>+0.05</sup> <sub>-0.05</sub>	0.11 <sup>+0.05</sup> <sub>-0.05</sub>	0.00 <sup>+0.02</sup> <sub>-0.02</sub>	0.32 <sup>+0.03</sup> <sub>-0.03</sub>	0.19 <sup>+0.03</sup> <sub>-0.03</sub>	-0.00 <sup>+0.11</sup> <sub>-0.11</sub>	
0.875	0.875	215 <sup>+3</sup> <sub>-3</sub>	13.5 <sup>+0.7</sup> <sub>-0.7</sub>	-0.23 <sup>+0.02</sup> <sub>-0.02</sub>	2.2 <sup>+0.3</sup> <sub>-0.3</sub>	0.39 <sup>+0.05</sup> <sub>-0.05</sub>	0.19 <sup>+0.03</sup> <sub>-0.03</sub>	0.17 <sup>+0.04</sup> <sub>-0.04</sub>	0.05 <sup>+0.07</sup> <sub>-0.07</sub>	0.12 <sup>+0.05</sup> <sub>-0.05</sub>	-0.03 <sup>+0.02</sup> <sub>-0.02</sub>	0.32 <sup>+0.03</sup> <sub>-0.03</sub>	0.23 <sup>+0.03</sup> <sub>-0.03</sub>	0.16 <sup>+0.12</sup> <sub>-0.12</sub>	
UGC1382															
0.028	0.016	182 <sup>+3</sup> <sub>-3</sub>	9.5 <sup>+0.9</sup> <sub>-0.9</sub>	-0.05 <sup>+0.02</sup> <sub>-0.02</sub>	3.1 <sup>+0.2</sup> <sub>-0.2</sub>	0.24 <sup>+0.08</sup> <sub>-0.10</sub>	0.29 <sup>+0.04</sup> <sub>-0.04</sub>	0.22 <sup>+0.06</sup> <sub>-0.06</sub>	0.15 <sup>+0.05</sup> <sub>-0.05</sub>	0.19 <sup>+0.05</sup> <sub>-0.05</sub>	-0.02 <sup>+0.03</sup> <sub>-0.03</sub>	0.06 <sup>+0.16</sup> <sub>-0.16</sub>	0.23 <sup>+0.03</sup> <sub>-0.03</sub>	-0.36 <sup>+0.09</sup> <sub>-0.09</sub>	
0.052	0.047	179 <sup>+4</sup> <sub>-4</sub>	10.9 <sup>+1.4</sup> <sub>-1.4</sub>	-0.05 <sup>+0.03</sup> <sub>-0.03</sub>	2.4 <sup>+0.4</sup> <sub>-0.4</sub>	0.51 <sup>+0.04</sup> <sub>-0.04</sub>	0.26 <sup>+0.05</sup> <sub>-0.05</sub>	0.31 <sup>+0.06</sup> <sub>-0.06</sub>	0.17 <sup>+0.05</sup> <sub>-0.05</sub>	0.36 <sup>+0.05</sup> <sub>-0.05</sub>	-0.08 <sup>+0.03</sup> <sub>-0.03</sub>	0.23 <sup>+0.15</sup> <sub>-0.15</sub>	0.35 <sup>+0.04</sup> <sub>-0.04</sub>	-0.32 <sup>+0.07</sup> <sub>-0.07</sub>	
0.097	0.094	173 <sup>+3</sup> <sub>-3</sub>	9.7 <sup>+1.0</sup> <sub>-0.9</sub>	-0.05 <sup>+0.03</sup> <sub>-0.03</sub>	3.2 <sup>+0.1</sup> <sub>-0.1</sub>	0.27 <sup>+0.09</sup> <sub>-0.11</sub>	0.26 <sup>+0.05</sup> <sub>-0.05</sub>	0.21 <sup>+0.07</sup> <sub>-0.07</sub>	0.00 <sup>+0.06</sup> <sub>-0.06</sub>	0.22 <sup>+0.06</sup> <sub>-0.06</sub>	-0.04 <sup>+0.03</sup> <sub>-0.03</sub>	0.33 <sup>+0.15</sup> <sub>-0.15</sub>	0.25 <sup>+0.04</sup> <sub>-0.04</sub>	-0.34 <sup>+0.09</sup> <sub>-0.09</sub>	
0.189	0.188	157 <sup>+3</sup> <sub>-3</sub>	10.5 <sup>+1.3</sup> <sub>-1.1</sub>	-0.07 <sup>+0.03</sup> <sub>-0.03</sub>	2.7 <sup>+0.3</sup> <sub>-0.3</sub>	0.19 <sup>+0.08</sup> <sub>-0.06</sub>	0.17 <sup>+0.05</sup> <sub>-0.05</sub>	0.33 <sup>+0.06</sup> <sub>-0.06</sub>	0.15 <sup>+0.06</sup> <sub>-0.06</sub>	0.17 <sup>+0.06</sup> <sub>-0.06</sub>	-0.11 <sup>+0.03</sup> <sub>-0.03</sub>	0.26 <sup>+0.18</sup> <sub>-0.18</sub>	0.18 <sup>+0.04</sup> <sub>-0.04</sub>	-0.1	

Table 6 (continued)

$r/R_e$	$x/R_e$	$\sigma$ ( $\text{km s}^{-1}$ )	$t$ (Gyr)	[Z/H] (dex)	IMF	[O/Fe] (dex)	[Mg/Fe] (dex)	[Si/Fe] (dex)	[Ca/Fe] (dex)	[Ti/Fe] (dex)	[Fe/H] (dex)	[Na/Fe] (dex)	[C/Fe] (dex)	[N/Fe] (dex)
IC1459														
0.012	0.004	307 <sup>+8</sup> <sub>-8</sub>	13.1 <sup>+0.9</sup> <sub>-1.0</sub>	0.13 <sup>+0.02</sup> <sub>-0.02</sub>	2.2 <sup>+0.4</sup> <sub>-0.5</sub>	0.44 <sup>+0.07</sup> <sub>-0.07</sub>	0.20 <sup>+0.05</sup> <sub>-0.05</sub>	0.20 <sup>+0.14</sup> <sub>-0.14</sub>	0.04 <sup>+0.07</sup> <sub>-0.06</sub>	0.07 <sup>+0.06</sup> <sub>-0.06</sub>	-0.07 <sup>+0.03</sup> <sub>-0.03</sub>	0.77 <sup>+0.06</sup> <sub>-0.05</sub>	0.25 <sup>+0.03</sup> <sub>-0.03</sub>	0.38 <sup>+0.09</sup> <sub>-0.09</sub>
0.023	0.020	295 <sup>+11</sup> <sub>-11</sub>	13.5 <sup>+0.7</sup> <sub>-0.8</sub>	0.09 <sup>+0.05</sup> <sub>-0.05</sub>	2.3 <sup>+0.4</sup> <sub>-0.5</sub>	0.37 <sup>+0.05</sup> <sub>-0.05</sub>	0.21 <sup>+0.06</sup> <sub>-0.06</sub>	0.16 <sup>+0.08</sup> <sub>-0.09</sub>	0.02 <sup>+0.06</sup> <sub>-0.06</sub>	0.08 <sup>+0.08</sup> <sub>-0.08</sub>	-0.01 <sup>+0.03</sup> <sub>-0.03</sub>	0.69 <sup>+0.07</sup> <sub>-0.07</sub>	0.21 <sup>+0.04</sup> <sub>-0.04</sub>	0.28 <sup>+0.11</sup> <sub>-0.11</sub>
0.048	0.047	290 <sup>+8</sup> <sub>-8</sub>	12.9 <sup>+0.7</sup> <sub>-0.9</sub>	0.06 <sup>+0.04</sup> <sub>-0.04</sub>	2.4 <sup>+0.5</sup> <sub>-0.5</sub>	0.35 <sup>+0.04</sup> <sub>-0.05</sub>	0.21 <sup>+0.05</sup> <sub>-0.06</sub>	0.15 <sup>+0.11</sup> <sub>-0.11</sub>	0.03 <sup>+0.05</sup> <sub>-0.05</sub>	0.10 <sup>+0.08</sup> <sub>-0.08</sub>	-0.01 <sup>+0.03</sup> <sub>-0.03</sub>	0.60 <sup>+0.06</sup> <sub>-0.06</sub>	0.20 <sup>+0.03</sup> <sub>-0.03</sub>	0.21 <sup>+0.07</sup> <sub>-0.07</sub>
0.094	0.094	284 <sup>+9</sup> <sub>-9</sub>	12.4 <sup>+1.1</sup> <sub>-1.2</sub>	0.02 <sup>+0.06</sup> <sub>-0.06</sub>	2.2 <sup>+0.5</sup> <sub>-0.5</sub>	0.37 <sup>+0.05</sup> <sub>-0.05</sub>	0.22 <sup>+0.05</sup> <sub>-0.05</sub>	0.16 <sup>+0.10</sup> <sub>-0.11</sub>	0.07 <sup>+0.07</sup> <sub>-0.07</sub>	0.08 <sup>+0.10</sup> <sub>-0.10</sub>	-0.03 <sup>+0.04</sup> <sub>-0.04</sub>	0.57 <sup>+0.05</sup> <sub>-0.06</sub>	0.22 <sup>+0.04</sup> <sub>-0.04</sub>	0.16 <sup>+0.08</sup> <sub>-0.09</sub>
0.188	0.188	272 <sup>+13</sup> <sub>-13</sub>	11.6 <sup>+1.7</sup> <sub>-1.7</sub>	-0.09 <sup>+0.04</sup> <sub>-0.04</sub>	1.9 <sup>+0.5</sup> <sub>-0.5</sub>	0.42 <sup>+0.05</sup> <sub>-0.05</sub>	0.21 <sup>+0.07</sup> <sub>-0.07</sub>	0.15 <sup>+0.09</sup> <sub>-0.10</sub>	0.05 <sup>+0.05</sup> <sub>-0.05</sub>	-0.06 <sup>+0.09</sup> <sub>-0.09</sub>	-0.03 <sup>+0.03</sup> <sub>-0.03</sub>	0.45 <sup>+0.09</sup> <sub>-0.10</sub>	0.23 <sup>+0.03</sup> <sub>-0.03</sub>	0.17 <sup>+0.11</sup> <sub>-0.11</sub>
0.375	0.375	252 <sup>+14</sup> <sub>-14</sub>	8.7 <sup>+1.7</sup> <sub>-1.7</sub>	-0.24 <sup>+0.06</sup> <sub>-0.06</sub>	1.8 <sup>+0.4</sup> <sub>-0.5</sub>	0.45 <sup>+0.07</sup> <sub>-0.07</sub>	0.24 <sup>+0.10</sup> <sub>-0.10</sub>	0.09 <sup>+0.12</sup> <sub>-0.12</sub>	-0.02 <sup>+0.09</sup> <sub>-0.09</sub>	-0.14 <sup>+0.11</sup> <sub>-0.11</sub>	-0.04 <sup>+0.06</sup> <sub>-0.06</sub>	0.37 <sup>+0.07</sup> <sub>-0.08</sub>	0.22 <sup>+0.06</sup> <sub>-0.06</sub>	0.03 <sup>+0.20</sup> <sub>-0.21</sub>
0.625	0.625	256 <sup>+13</sup> <sub>-13</sub>	7.8 <sup>+3.0</sup> <sub>-3.0</sub>	-0.31 <sup>+0.18</sup> <sub>-0.18</sub>	2.1 <sup>+0.4</sup> <sub>-0.6</sub>	0.43 <sup>+0.07</sup> <sub>-0.07</sub>	0.19 <sup>+0.07</sup> <sub>-0.07</sub>	-0.16 <sup>+0.13</sup> <sub>-0.12</sub>	-0.17 <sup>+0.07</sup> <sub>-0.07</sub>	-0.27 <sup>+0.09</sup> <sub>-0.08</sub>	-0.04 <sup>+0.05</sup> <sub>-0.04</sub>	0.38 <sup>+0.08</sup> <sub>-0.12</sub>	0.21 <sup>+0.05</sup> <sub>-0.05</sub>	-0.04 <sup>+0.21</sup> <sub>-0.20</sub>
0.875	0.875	251 <sup>+17</sup> <sub>-17</sub>	6.5 <sup>+2.5</sup> <sub>-2.5</sub>	-0.32 <sup>+0.21</sup> <sub>-0.21</sub>	2.4 <sup>+0.7</sup> <sub>-0.7</sub>	0.45 <sup>+0.13</sup> <sub>-0.14</sub>	0.21 <sup>+0.13</sup> <sub>-0.13</sub>	-0.13 <sup>+0.19</sup> <sub>-0.19</sub>	-0.09 <sup>+0.13</sup> <sub>-0.13</sub>	-0.31 <sup>+0.12</sup> <sub>-0.12</sub>	-0.09 <sup>+0.11</sup> <sub>-0.11</sub>	0.38 <sup>+0.11</sup> <sub>-0.19</sub>	0.23 <sup>+0.12</sup> <sub>-0.12</sub>	-0.10 <sup>+0.24</sup> <sub>-0.22</sub>

## REFERENCES

- Alton, P. D., Smith, R. J., & Lucey, J. R. 2017, *MNRAS*, 468, 1594, doi: [10.1093/mnras/stx464](https://doi.org/10.1093/mnras/stx464)
- . 2018, *MNRAS*, 478, 4464, doi: [10.1093/mnras/sty1242](https://doi.org/10.1093/mnras/sty1242)
- Amblard, A., Riguccini, L., Temi, P., et al. 2014, *ApJ*, 783, 135, doi: [10.1088/0004-637X/783/2/135](https://doi.org/10.1088/0004-637X/783/2/135)
- Annibali, F., Bressan, A., Rampazzo, R., Zeilinger, W. W., & Danese, L. 2007, *A&A*, 463, 455, doi: [10.1051/0004-6361:20054726](https://doi.org/10.1051/0004-6361:20054726)
- Baldwin, C., McDermid, R. M., Kuntschner, H., Maraston, C., & Conroy, C. 2018, *MNRAS*, 473, 4698, doi: [10.1093/mnras/stx2502](https://doi.org/10.1093/mnras/stx2502)
- Barbosa, C. E., Spiniello, C., Arnaboldi, M., et al. 2021a, *A&A*, 649, A93, doi: [10.1051/0004-6361/202039809](https://doi.org/10.1051/0004-6361/202039809)
- . 2021b, *A&A*, 645, L1, doi: [10.1051/0004-6361/202039810](https://doi.org/10.1051/0004-6361/202039810)
- Bertin, G., Bertola, F., Buson, L. M., et al. 1994, *A&A*, 292, 381
- Cappellari, M. 2012, pPXF: Penalized Pixel-Fitting stellar kinematics extraction. <http://ascl.net/1210.002>
- . 2017, *MNRAS*, 466, 798, doi: [10.1093/mnras/stw3020](https://doi.org/10.1093/mnras/stw3020)
- Cappellari, M., & Emsellem, E. 2004, *PASP*, 116, 138, doi: [10.1086/381875](https://doi.org/10.1086/381875)
- Cappellari, M., Verolme, E. K., van der Marel, R. P., et al. 2002, *ApJ*, 578, 787, doi: [10.1086/342653](https://doi.org/10.1086/342653)
- Cappellari, M., Bacon, R., Bureau, M., et al. 2006, *MNRAS*, 366, 1126, doi: [10.1111/j.1365-2966.2005.09981.x](https://doi.org/10.1111/j.1365-2966.2005.09981.x)
- Cappellari, M., McDermid, R. M., Alatalo, K., et al. 2012, *Nature*, 484, 485, doi: [10.1038/nature10972](https://doi.org/10.1038/nature10972)
- Carlsten, S. G., Hau, G. K. T., & Zenteno, A. 2017, *MNRAS*, 472, 2889, doi: [10.1093/mnras/stx2182](https://doi.org/10.1093/mnras/stx2182)
- Carter, D., Prieur, J. L., Wilkinson, A., Sparks, W. B., & Malin, D. F. 1988, *MNRAS*, 235, 813, doi: [10.1093/mnras/235.3.813](https://doi.org/10.1093/mnras/235.3.813)
- Cenarro, A. J., Gorgas, J., Vazdekis, A., Cardiel, N., & Peletier, R. F. 2003, *MNRAS*, 339, L12, doi: [10.1046/j.1365-8711.2003.06360.x](https://doi.org/10.1046/j.1365-8711.2003.06360.x)
- Chen, C.-W., Côté, P., West, A. A., Peng, E. W., & Ferrarese, L. 2010, *ApJS*, 191, 1, doi: [10.1088/0067-0049/191/1/1](https://doi.org/10.1088/0067-0049/191/1/1)
- Conroy, C. 2013, *ARA&A*, 51, 393, doi: [10.1146/annurev-astro-082812-141017](https://doi.org/10.1146/annurev-astro-082812-141017)
- Conroy, C., Graves, G. J., & van Dokkum, P. G. 2014, *ApJ*, 780, 33, doi: [10.1088/0004-637X/780/1/33](https://doi.org/10.1088/0004-637X/780/1/33)
- Conroy, C., & van Dokkum, P. G. 2012, *ApJ*, 760, 71, doi: [10.1088/0004-637X/760/1/71](https://doi.org/10.1088/0004-637X/760/1/71)
- Conroy, C., van Dokkum, P. G., & Villaume, A. 2017, *ApJ*, 837, 166, doi: [10.3847/1538-4357/aa6190](https://doi.org/10.3847/1538-4357/aa6190)
- Conroy, C., Villaume, A., van Dokkum, P. G., & Lind, K. 2018, *ApJ*, 854, 139, doi: [10.3847/1538-4357/aaab49](https://doi.org/10.3847/1538-4357/aaab49)
- Corwin, Harold G., J., Buta, R. J., & de Vaucouleurs, G. 1994, *AJ*, 108, 2128, doi: [10.1086/117225](https://doi.org/10.1086/117225)
- De Lucia, G., Springel, V., White, S. D. M., Croton, D., & Kauffmann, G. 2006, *MNRAS*, 366, 499, doi: [10.1111/j.1365-2966.2005.09879.x](https://doi.org/10.1111/j.1365-2966.2005.09879.x)
- Dejonghe, H., de Bruyne, V., Vauterin, P., & Zeilinger, W. W. 1996, *A&A*, 306, 363, <https://arxiv.org/abs/astro-ph/9509036>
- Dressler, A., Hare, T., Bigelow, B. C., & Osip, D. J. 2006, in *Society of Photo-Optical Instrumentation Engineers (SPIE) Conference Series*, Vol. 6269, Society of Photo-Optical Instrumentation Engineers (SPIE) Conference Series, ed. I. S. McLean & M. Iye, 62690F, doi: [10.1117/12.670573](https://doi.org/10.1117/12.670573)
- Drinkwater, M. J., Gregg, M. D., & Colless, M. 2001, *ApJL*, 548, L139, doi: [10.1086/319113](https://doi.org/10.1086/319113)
- Emsellem, E., Cappellari, M., Peletier, R. F., et al. 2004, *MNRAS*, 352, 721, doi: [10.1111/j.1365-2966.2004.07948.x](https://doi.org/10.1111/j.1365-2966.2004.07948.x)
- Feldmeier-Krause, A., Lonoce, I., & Freedman, W. L. 2020, *ApJ*, 902, 12, doi: [10.3847/1538-4357/abafb3](https://doi.org/10.3847/1538-4357/abafb3)
- Ferreras, I., Scott, N., La Barbera, F., et al. 2019, *MNRAS*, 489, 608, doi: [10.1093/mnras/stz2095](https://doi.org/10.1093/mnras/stz2095)
- Forbes, D. A., Reitzel, D. B., & Williger, G. M. 1995, *AJ*, 109, 1576, doi: [10.1086/117386](https://doi.org/10.1086/117386)
- Forbes, D. A., Sánchez-Blázquez, P., & Proctor, R. 2005, *MNRAS*, 361, L6, doi: [10.1111/j.1745-3933.2005.00052.x](https://doi.org/10.1111/j.1745-3933.2005.00052.x)
- Foreman-Mackey, D. 2016, *The Journal of Open Source Software*, 1, 24, doi: [10.21105/joss.00024](https://doi.org/10.21105/joss.00024)
- Foreman-Mackey, D., Hogg, D. W., Lang, D., & Goodman, J. 2013, *PASP*, 125, 306, doi: [10.1086/670067](https://doi.org/10.1086/670067)
- Franx, M., Illingworth, G., & Heckman, T. 1989, *ApJ*, 344, 613, doi: [10.1086/167830](https://doi.org/10.1086/167830)
- Franx, M., & Illingworth, G. D. 1988, *ApJL*, 327, L55, doi: [10.1086/185139](https://doi.org/10.1086/185139)
- González Delgado, R. M., Pérez, E., Cid Fernandes, R., et al. 2014, *A&A*, 562, A47, doi: [10.1051/0004-6361/201322011](https://doi.org/10.1051/0004-6361/201322011)
- Graves, G. J., & Faber, S. M. 2010, *ApJ*, 717, 803, doi: [10.1088/0004-637X/717/2/803](https://doi.org/10.1088/0004-637X/717/2/803)
- Graves, G. J., Faber, S. M., & Schiavon, R. P. 2009, *ApJ*, 698, 1590, doi: [10.1088/0004-637X/698/2/1590](https://doi.org/10.1088/0004-637X/698/2/1590)
- Graves, G. J., Faber, S. M., Schiavon, R. P., & Yan, R. 2007, *ApJ*, 671, 243, doi: [10.1086/522325](https://doi.org/10.1086/522325)
- Greene, J. E., Janish, R., Ma, C.-P., et al. 2015, *ApJ*, 807, 11, doi: [10.1088/0004-637X/807/1/11](https://doi.org/10.1088/0004-637X/807/1/11)
- Greene, J. E., Murphy, J. D., Graves, G. J., et al. 2013, *ApJ*, 776, 64, doi: [10.1088/0004-637X/776/2/64](https://doi.org/10.1088/0004-637X/776/2/64)

- Hagen, L. M. Z., Seibert, M., Hagen, A., et al. 2016, *ApJ*, 826, 210, doi: [10.3847/0004-637X/826/2/210](https://doi.org/10.3847/0004-637X/826/2/210)
- Ho, L. C., Li, Z.-Y., Barth, A. J., Seigar, M. S., & Peng, C. Y. 2011, *ApJS*, 197, 21, doi: [10.1088/0067-0049/197/2/21](https://doi.org/10.1088/0067-0049/197/2/21)
- Hunter, J. D. 2007, *Computing in Science and Engineering*, 9, 90, doi: [10.1109/MCSE.2007.55](https://doi.org/10.1109/MCSE.2007.55)
- Iodice, E., Sarzi, M., Bittner, A., et al. 2019, *A&A*, 627, A136, doi: [10.1051/0004-6361/201935721](https://doi.org/10.1051/0004-6361/201935721)
- Johansson, J., Thomas, D., & Maraston, C. 2012, *MNRAS*, 421, 1908, doi: [10.1111/j.1365-2966.2011.20316.x](https://doi.org/10.1111/j.1365-2966.2011.20316.x)
- Kausch, W., Noll, S., Smette, A., et al. 2015, *A&A*, 576, A78, doi: [10.1051/0004-6361/201423909](https://doi.org/10.1051/0004-6361/201423909)
- Koprolin, W., & Zeilinger, W. W. 2000, *A&AS*, 145, 71, doi: [10.1051/aas:2000232](https://doi.org/10.1051/aas:2000232)
- Kourkchi, E., & Tully, R. B. 2017, *ApJ*, 843, 16, doi: [10.3847/1538-4357/aa76db](https://doi.org/10.3847/1538-4357/aa76db)
- Krajnović, D., Ural, U., Kuntschner, H., et al. 2020, *A&A*, 635, A129, doi: [10.1051/0004-6361/201937040](https://doi.org/10.1051/0004-6361/201937040)
- Kroupa, P. 2001, *MNRAS*, 322, 231, doi: [10.1046/j.1365-8711.2001.04022.x](https://doi.org/10.1046/j.1365-8711.2001.04022.x)
- Kuntschner, H., Emsellem, E., Bacon, R., et al. 2010, *MNRAS*, 408, 97, doi: [10.1111/j.1365-2966.2010.17161.x](https://doi.org/10.1111/j.1365-2966.2010.17161.x)
- La Barbera, F., Ferreras, I., Vazdekis, A., et al. 2013, *MNRAS*, 433, 3017, doi: [10.1093/mnras/stt943](https://doi.org/10.1093/mnras/stt943)
- La Barbera, F., Vazdekis, A., Ferreras, I., et al. 2019, *MNRAS*, 489, 4090, doi: [10.1093/mnras/stz2192](https://doi.org/10.1093/mnras/stz2192)
- Lin, L., Cooper, M. C., Jian, H.-Y., et al. 2010, *ApJ*, 718, 1158, doi: [10.1088/0004-637X/718/2/1158](https://doi.org/10.1088/0004-637X/718/2/1158)
- Longhetti, M., Saracco, P., Severgnini, P., et al. 2005, *MNRAS*, 361, 897, doi: [10.1111/j.1365-2966.2005.09215.x](https://doi.org/10.1111/j.1365-2966.2005.09215.x)
- Lonoce, I., Feldmeier-Krause, A., & Freedman, W. L. 2021, arXiv e-prints, arXiv:2107.02335. <https://arxiv.org/abs/2107.02335>
- Machacek, M., Dosaj, A., Forman, W., et al. 2005, *ApJ*, 621, 663, doi: [10.1086/427548](https://doi.org/10.1086/427548)
- Maeder, A. 1992, *A&A*, 264, 105
- Maiolino, R., & Mannucci, F. 2019, *A&A Rv*, 27, 3, doi: [10.1007/s00159-018-0112-2](https://doi.org/10.1007/s00159-018-0112-2)
- Makarov, D., Prugniel, P., Terekhova, N., Courtois, H., & Vauglin, I. 2014, *A&A*, 570, A13, doi: [10.1051/0004-6361/201423496](https://doi.org/10.1051/0004-6361/201423496)
- Marigo, P. 2001, *A&A*, 370, 194, doi: [10.1051/0004-6361:20000247](https://doi.org/10.1051/0004-6361:20000247)
- Martín-Navarro, I., La Barbera, F., Vazdekis, A., Falcón-Barroso, J., & Ferreras, I. 2015a, *MNRAS*, 447, 1033, doi: [10.1093/mnras/stu2480](https://doi.org/10.1093/mnras/stu2480)
- Martín-Navarro, I., Vazdekis, A., Falcón-Barroso, J., et al. 2018, *MNRAS*, 475, 3700, doi: [10.1093/mnras/stx3346](https://doi.org/10.1093/mnras/stx3346)
- Martín-Navarro, I., Vazdekis, A., La Barbera, F., et al. 2015b, *ApJL*, 806, L31, doi: [10.1088/2041-8205/806/2/L31](https://doi.org/10.1088/2041-8205/806/2/L31)
- Martín-Navarro, I., Lyubenova, M., van de Ven, G., et al. 2019, *A&A*, 626, A124, doi: [10.1051/0004-6361/201935360](https://doi.org/10.1051/0004-6361/201935360)
- McDermid, R. M., Cappellari, M., Alatalo, K., et al. 2014, *ApJL*, 792, L37, doi: [10.1088/2041-8205/792/2/L37](https://doi.org/10.1088/2041-8205/792/2/L37)
- McDermid, R. M., Alatalo, K., Blitz, L., et al. 2015, *MNRAS*, 448, 3484, doi: [10.1093/mnras/stv105](https://doi.org/10.1093/mnras/stv105)
- McWilliam, A. 2016, *PASA*, 33, e040, doi: [10.1017/pasa.2016.32](https://doi.org/10.1017/pasa.2016.32)
- McWilliam, A., Matteucci, F., Ballero, S., et al. 2008, *AJ*, 136, 367, doi: [10.1088/0004-6256/136/1/367](https://doi.org/10.1088/0004-6256/136/1/367)
- Mehlert, D., Thomas, D., Saglia, R. P., Bender, R., & Wegner, G. 2003, *A&A*, 407, 423, doi: [10.1051/0004-6361:20030886](https://doi.org/10.1051/0004-6361:20030886)
- Meynet, G., & Maeder, A. 2002, *A&A*, 390, 561, doi: [10.1051/0004-6361:20020755](https://doi.org/10.1051/0004-6361:20020755)
- Naab, T., Johansson, P. H., & Ostriker, J. P. 2009, *ApJL*, 699, L178, doi: [10.1088/0004-637X/699/2/L178](https://doi.org/10.1088/0004-637X/699/2/L178)
- Oser, L., Ostriker, J. P., Naab, T., Johansson, P. H., & Burkert, A. 2010, *ApJ*, 725, 2312, doi: [10.1088/0004-637X/725/2/2312](https://doi.org/10.1088/0004-637X/725/2/2312)
- Osterbrock, D. E. 1989, *Astrophysics of gaseous nebulae and active galactic nuclei*
- Parikh, T., Thomas, D., Maraston, C., et al. 2018, *MNRAS*, 477, 3954, doi: [10.1093/mnras/sty785](https://doi.org/10.1093/mnras/sty785)
- . 2019, *MNRAS*, 483, 3420, doi: [10.1093/mnras/sty3339](https://doi.org/10.1093/mnras/sty3339)
- Portinari, L., Chiosi, C., & Bressan, A. 1998, *A&A*, 334, 505. <https://arxiv.org/abs/astro-ph/9711337>
- Prichard, L. J., Vaughan, S. P., & Davies, R. L. 2019, *MNRAS*, 488, 1679, doi: [10.1093/mnras/stz1191](https://doi.org/10.1093/mnras/stz1191)
- Raimann, D., Storch-Bergmann, T., Quintana, H., Hunstead, R., & Wisotzki, L. 2005, *MNRAS*, 364, 1239, doi: [10.1111/j.1365-2966.2005.09665.x](https://doi.org/10.1111/j.1365-2966.2005.09665.x)
- Rawle, T. D., Smith, R. J., Lucey, J. R., & Swinbank, A. M. 2008, *MNRAS*, 389, 1891, doi: [10.1111/j.1365-2966.2008.13720.x](https://doi.org/10.1111/j.1365-2966.2008.13720.x)
- Reynolds, C. S., Ward, M. J., Fabian, A. C., & Celotti, A. 1997, *MNRAS*, 291, 403, doi: [10.1093/mnras/291.3.403](https://doi.org/10.1093/mnras/291.3.403)
- Romano, D., Franchini, M., Grisoni, V., et al. 2020, *A&A*, 639, A37, doi: [10.1051/0004-6361/202037972](https://doi.org/10.1051/0004-6361/202037972)
- Rosa, D. A., Milone, A. C., Krabbe, A. C., & Rodrigues, I. 2018, *Ap&SS*, 363, 131, doi: [10.1007/s10509-018-3353-7](https://doi.org/10.1007/s10509-018-3353-7)
- Saglia, R. P., Bertin, G., Bertola, F., et al. 1993, *ApJ*, 403, 567, doi: [10.1086/172226](https://doi.org/10.1086/172226)
- Salpeter, E. E. 1955, *ApJ*, 121, 161, doi: [10.1086/145971](https://doi.org/10.1086/145971)

- Sánchez-Blázquez, P., Forbes, D. A., Strader, J., Brodie, J., & Proctor, R. 2007, *MNRAS*, 377, 759, doi: [10.1111/j.1365-2966.2007.11647.x](https://doi.org/10.1111/j.1365-2966.2007.11647.x)
- Sarzi, M., Spiniello, C., La Barbera, F., Krajnović, D., & van den Bosch, R. 2018, *MNRAS*, 478, 4084, doi: [10.1093/mnras/sty1092](https://doi.org/10.1093/mnras/sty1092)
- Schiavon, R. P. 2007, *ApJS*, 171, 146, doi: [10.1086/511753](https://doi.org/10.1086/511753)
- Schlafly, E. F., & Finkbeiner, D. P. 2011, *ApJ*, 737, 103, doi: [10.1088/0004-637X/737/2/103](https://doi.org/10.1088/0004-637X/737/2/103)
- Serra, P., & Oosterloo, T. A. 2010, *MNRAS*, 401, L29, doi: [10.1111/j.1745-3933.2009.00779.x](https://doi.org/10.1111/j.1745-3933.2009.00779.x)
- Serra, P., & Trager, S. C. 2007, *MNRAS*, 374, 769, doi: [10.1111/j.1365-2966.2006.11188.x](https://doi.org/10.1111/j.1365-2966.2006.11188.x)
- Smette, A., Sana, H., Noll, S., et al. 2015, *A&A*, 576, A77, doi: [10.1051/0004-6361/201423932](https://doi.org/10.1051/0004-6361/201423932)
- Smith, R. J. 2020, *ARA&A*, 58, 577, doi: [10.1146/annurev-astro-032620-020217](https://doi.org/10.1146/annurev-astro-032620-020217)
- Smith, R. J., Lucey, J. R., Hudson, M. J., & Bridges, T. J. 2009, *MNRAS*, 398, 119, doi: [10.1111/j.1365-2966.2009.15146.x](https://doi.org/10.1111/j.1365-2966.2009.15146.x)
- Spiniello, C., Barnabè, M., Koopmans, L. V. E., & Trager, S. C. 2015, *MNRAS*, 452, L21, doi: [10.1093/mnras/151/2/L21](https://doi.org/10.1093/mnras/151/2/L21)
- Spiniello, C., Trager, S., Koopmans, L. V. E., & Conroy, C. 2014, *MNRAS*, 438, 1483, doi: [10.1093/mnras/stt2282](https://doi.org/10.1093/mnras/stt2282)
- Spolaor, M., Proctor, R. N., Forbes, D. A., & Couch, W. J. 2009, *ApJL*, 691, L138, doi: [10.1088/0004-637X/691/2/L138](https://doi.org/10.1088/0004-637X/691/2/L138)
- Stoehr, F., Fraquelli, D., Kamp, I., et al. 2007, *Space Telescope European Coordinating Facility Newsletter*, 42, 4
- Thomas, D., Maraston, C., Bender, R., & Mendes de Oliveira, C. 2005, *ApJ*, 621, 673, doi: [10.1086/426932](https://doi.org/10.1086/426932)
- Thomas, D., Maraston, C., Schawinski, K., Sarzi, M., & Silk, J. 2010, *MNRAS*, 404, 1775, doi: [10.1111/j.1365-2966.2010.16427.x](https://doi.org/10.1111/j.1365-2966.2010.16427.x)
- Tody, D. 1986, in *Society of Photo-Optical Instrumentation Engineers (SPIE) Conference Series*, Vol. 627, *Instrumentation in astronomy VI*, ed. D. L. Crawford, 733, doi: [10.1117/12.968154](https://doi.org/10.1117/12.968154)
- Tody, D. 1993, in *Astronomical Society of the Pacific Conference Series*, Vol. 52, *Astronomical Data Analysis Software and Systems II*, ed. R. J. Hanisch, R. J. V. Brissenden, & J. Barnes, 173
- Trager, S. C., Faber, S. M., Worthey, G., & González, J. J. 2000a, *AJ*, 119, 1645, doi: [10.1086/301299](https://doi.org/10.1086/301299)
- . 2000b, *AJ*, 120, 165, doi: [10.1086/301442](https://doi.org/10.1086/301442)
- Treu, T., Auger, M. W., Koopmans, L. V. E., et al. 2010, *ApJ*, 709, 1195, doi: [10.1088/0004-637X/709/2/1195](https://doi.org/10.1088/0004-637X/709/2/1195)
- van der Walt, S., Colbert, S. C., & Varoquaux, G. 2011, *Computing in Science and Engineering*, 13, 22, doi: [10.1109/MCSE.2011.37](https://doi.org/10.1109/MCSE.2011.37)
- van Dokkum, P., Conroy, C., Villaume, A., Brodie, J., & Romanowsky, A. J. 2017, *ApJ*, 841, 68, doi: [10.3847/1538-4357/aa7135](https://doi.org/10.3847/1538-4357/aa7135)
- van Dokkum, P. G., Bloom, J., & Tewes, M. 2012, *L.A.Cosmic: Laplacian Cosmic Ray Identification*. <http://ascl.net/1207.005>
- van Dokkum, P. G., & Conroy, C. 2010, *Nature*, 468, 940, doi: [10.1038/nature09578](https://doi.org/10.1038/nature09578)
- Vaughan, S. P., Davies, R. L., Zieleniewski, S., & Houghton, R. C. W. 2018a, *MNRAS*, 475, 1073, doi: [10.1093/mnras/stx3199](https://doi.org/10.1093/mnras/stx3199)
- . 2018b, *MNRAS*, 479, 2443, doi: [10.1093/mnras/sty1434](https://doi.org/10.1093/mnras/sty1434)
- Wilkinson, D. M., Maraston, C., Thomas, D., et al. 2015, *MNRAS*, 449, 328, doi: [10.1093/mnras/stv301](https://doi.org/10.1093/mnras/stv301)
- Worthey, G., Tang, B., & Serven, J. 2014, *ApJ*, 783, 20, doi: [10.1088/0004-637X/783/1/20](https://doi.org/10.1088/0004-637X/783/1/20)
- Yan, Z., Jerabkova, T., & Kroupa, P. 2019, *A&A*, 632, A110, doi: [10.1051/0004-6361/201936636](https://doi.org/10.1051/0004-6361/201936636)
- Zhou, S., Mo, H. J., Li, C., et al. 2019, *MNRAS*, 485, 5256, doi: [10.1093/mnras/stz764](https://doi.org/10.1093/mnras/stz764)
- Zieleniewski, S., Houghton, R. C. W., Thatte, N., Davies, R. L., & Vaughan, S. P. 2017, *MNRAS*, 465, 192, doi: [10.1093/mnras/stw2712](https://doi.org/10.1093/mnras/stw2712)